Physik-Department

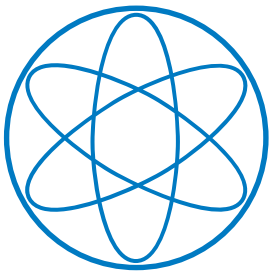

Segmented High Purity Germanium Detectors: Systematic Effects

Diplomarbeit von Annika Vauth

München, den 22. Oktober 2010

Max-Planck-Institut für Physik
(Werner-Heisenberg-Institut)

Technische Universität München

Abstract

Since the postulation and discovery of neutrinos, they have been the focus of numerous experiments. Neutrino oscillation experiments provided evidence for a finite neutrino mass. However, the absolute mass scale of the neutrinos is still unknown, as well as whether or not neutrinos are Majorana-particles , i.e. their own anti-particles.

These questions can be addressed by observation of neutrinoless double beta decay. The GERmanium Detector Array, GERDA, is designed to use germanium detectors to search for this decay in ^{76}Ge. If the decay is observed, the lifetime allows to draw conclusions on the effective Majorana mass of the neutrino. If it exists, it is a very rare process, thus the sensitivity of the experiment depends on background index. One way for background discrimination is the use of segmented detectors.

Systematic effects of 18-fold segmented high-purity n-type germanium detectors were studied:

The effects of a floating detector segment were investigated. A procedure to reconstruct the energy spectrum of the floating segment is presented. This shows that even if a contact is lost, nearly the full energy information can be extracted.

Data was taken to study the effect of a partial metallization of the segment contacts on the performance of an 18-fold segmented prototype detector. No effect on resolution was found within the experimental uncertainties.

Experimental and simulated data were compared to study the homogeneity of the active volume of another 18-fold segmented detector. The top and bottom layers were found to have smaller active volumes than the middle layer.

Zusammenfassung

Seit dem Postulat und dem experimentellen Nachweis von Neutrinos gab es zahlreiche Experimente, mit denen ihre Eigenschaften untersucht wurden. Die Beobachtung von Neutrino-Oszillationen weist auf die Existenz massiver Neutrinos hin und ermöglicht eine indirekte Messung der Massendifferenzen. Die Frage nach der absoluten Massenskala können sie jedoch nicht beantworten. Ebenfalls ungeklärt ist, ob Neutrinos Majorana-Teilchen, d.h. ihre eigenen Antiteilchen, sind.

Der neutrinolose Doppelbetazerfall, sofern er beobachtet wird, könnte diesen Fragen nachgehen. Im Zuge des GERDA-Experiments (GERmanium Detector Array) werden Germanium-Detektoren verwendet, um diesen Zerfall in ^{76}Ge zu suchen. Aus der Halbwertszeit des neutrinolosen Doppelbetazerfalls ließen sich Rückschlüsse auf die effektive Majorana-Masse des Neutrinos ziehen. Falls der Prozess stattfindet, so hat er eine sehr lange Halbwertszeit. Ein niedriger Untergrund-Index ist wichtig, um eine hohe experimentelle Sensitivität zu erreichen. Segmentierte Detektoren bieten eine Möglichkeit, zwischen Signal- und Untergrund-Ereignissen zu unterscheiden.

In dieser Arbeit werden Untersuchungen von systematischen Effekten von 18-fach segmentierten hochreinen n-Typ Germanium-Detektoren besprochen:

Die Auswirkungen eines unterbrochenen Segmentkontakts wurden analysiert. Eine Vorgehensweise zur Rekonstruktion der Energie-Information des betroffenen Segments wird vorgestellt. Es wurde gezeigt, dass nahezu alle Energie-Informationen extrahiert werden können.

Mit einem 18-fach segmentierten Prototyp-Detektor wurden Daten genommen, um die Auswirkungen einer teilweisen Metallisierung der Segment-Kontakte auf die Eigenschaften des Detektors zu prüfen. Ein solcher Effekt konnte innerhalb der Grenzen durch experimentelle Unsicherheiten nicht gefunden werden.

Experimentelle und simulierte Daten wurden verglichen, um die Homogenität des aktiven Volumens eines 18-fach segmentierten Detektors zu untersuchen. Ein geringeres aktives Volumen der äußeren Detektorschicht, gegenüber der mittleren Detektorschicht, wurde festgestellt.

Contents

1 Introduction

Neutrinos are an integral part of our universe. They are nearly as abundant as photons and can therefor have a large cosmological influence. However, their interaction with matter is so weak that studying their characteristics poses many experimental challenges, and fundamental questions regarding the properties of neutrinos are still unanswered.

Originally, neutrinos were assumed to be massless, but the observation of neutrino oscillations gave evidence for a finite neutrino mass. While mass differences can be deduced from these observations, the absolute mass scale of the neutrinos is still unknown.

Another essential question that is still open regards the nature of the neutrino. Whereas for all other fundamental particles a clear distinction between particles and anti-particles can be drawn, this is different for neutrinos. It is possible that neutrinos are Majorana-particles, i.e. their own anti-particles. This is the case for most theories explaining the matter-antimatter asymmetry in the universe.

The study of neutrinoless double beta decay can provide information about both the nature of the neutrino and the absolute mass scale of the neutrinos. The GERmanium Detector Array, GERDA, is an experiment designed to search for neutrinoless double beta decay in the germanium isotope ^{76}Ge. Germanium is particularly well suited material, since it is a semiconductor and can therefore not only serve as a source for the decay, but also as basis for detectors with very good energy resolution.

The sensitivity of neutrinoless double beta decay experiments is strongly dependent on the background level that can be achieved. GERDA is designed to reduce the background index by various techniques, such as reducing the amount of background producing material close to the detectors. For the second phase of GERDA, 18-fold segmented *High Purity Germanium (HPGe)* detectors were considered. By

using information of the segments, event topologies can be reconstructed. Thus certain types of background can be recognized.

The main goal of the work done for this thesis was to evaluate systematic effects of such 18-fold segmented high-purity germanium detectors. The structure of this thesis is as follows:

Chapter 2 gives a brief overview of the presently established picture of neutrino physics.

Chapter 3 discusses the physics of neutrinoless double beta decay as well as experimental considerations and techniques for its use in neutrino mass measurements.

Chapter 4 summarizes the design concept of GERDA and its background rejection techniques.

Chapter 5 introduces the operating principle of germanium detectors, as well as the detectors and detector test facilities used to take the data for this thesis.

Chapter 6 demonstrates the effects of a floating detector segment and presents an approach to reconstruct the corresponding energy spectrum.

Chapter 7 presents an investigation to address the question whether a partial metallization of the segment contacts has an effect on the performance of the detector.

Chapter 8 studies the homogeneity of the active volume of an 18-fold segmented prototype detector.

The results are summarized and an outlook to possible further studies is given in the last chapter.

2 Neutrino Physics

In the Standard Model of particle physics, neutrinos are assumed to be mass- and chargeless Dirac particles. New experimental evidence, especially the observation of neutrino oscillations, make a modification of the Standard model necessary to include massive neutrinos. The absolute mass scale of the neutrino still remains unknown, as oscillation experiments are only sensitive to the mass differences. The nature of the neutrinos is another open question: It is possible that neutrinos are their own anti-particles, so called *Majorana particles*, named after the Sicilian physicist Ettore Majorana.

This chapter gives a brief overview of the presently established picture of neutrino physics. For a more detailed discussion see for example [Alb04], [Giu07] or [Str10].

2.1 Neutrinos in the Standard Model

2.1.1 Fundamental Particles

The Standard Model of particle physics knows twelve fundamental fermions - six quarks and six leptons - as well as the force mediating gauge bosons, as illustrated in figure 2.1. The fermions are grouped into three families or flavors. Table 2.1 lists the twelve fermions and their respective electric charge. For each of these fermions, there is also an anti-particle with the same mass but opposite charge. Each electrically charged lepton is paired into a family with a chargeless neutrino. The *lepton number*, the number of leptons minus the number of anti-leptons, is conserved in the Standard Model [Pov94].

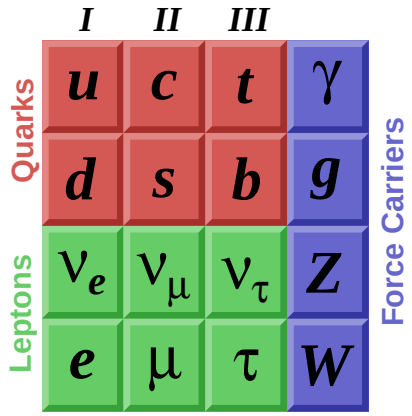

Figure 2.1: The Standard Model of particles physics, with fermions on the left and gauge bosons in the rightmost column.

Fermions	Flavor			Charge
Quarks	u	c	t	$+\frac{2}{3}$
	d	s	b	$-\frac{1}{3}$
Leptons	ν_e	ν_μ	ν_τ	0
	e^-	μ^-	τ^-	-1

Table 2.1: Fundamental fermions in the Standard Model and their respective electric charge.

2.1.2 Postulation of Neutrinos and Important Historical Experiments

The existence of neutrinos was first postulated by Wolfgang Pauli. He suggested that the energy conservation in β decay could be restored by including the emission of a light chargeless particle. With this hypothetic particle, β decay would be a three-body decay, which would explain the continuous energy spectrum [Pau85].

The β decay can be noted as

$$\beta\ -decay:\ n \rightarrow p + e^- + \overline{\nu_e}, \tag{2.1}$$

$$\beta\ +decay:\ p \rightarrow n + e^+ + \nu_e. \tag{2.2}$$

The first experimental proof for the existence of free neutrinos was based on the inverse β decay

$$p + \overline{\nu_e} \rightarrow n + e^+. \tag{2.3}$$

Frederick Reines and Clyde Cowan detected neutrinos created in a nuclear reactor. They could observe a pulse pair due to the annihilation of the positron, producing two photons, and the delayed capture of the neutron by the cadmium in the target material. This presented an identification of free neutrinos [Rei56], [Cow56].

Around the same time, the question whether the neutrinos accompanying the

$\beta -$ decay and the $\beta +$ decay were the same particle was also addressed experimentally for the first time. If ν and $\overline{\nu}$ were identical, the reaction

$$n + \overline{\nu_e} \rightarrow p + e^- \tag{2.4}$$

would be possible. Raymond Davis looked for this process in 1955 in an experiment based on a method suggested by Bruno Pontecorvo in 1946 [Bon05]: he tried to detect anti-neutrinos from the Savannah River reactor with the reaction

$$^{37}Cl + \overline{\nu_e} \rightarrow {}^{37}Ar + e^- \tag{2.5}$$

and reported a negative result [Dav55].

However, this result does not prove that ν and $\overline{\nu}$ are two intrinsically different particles. In 1956, Tsung Dao Lee and Chen Ning Yang postulated the violation of parity conservation in weak interactions [Lee56]. One year later Chien-Shiung Wu *et al.* verified this in an experiment measuring the angular distribution of the electrons coming from the beta decay polarized Co-60 atoms [Wu57].

Furthermore, in 1957 Maurice Goldhaber *et al.* performed an experiment to investigate the helicity of the neutrino. They found that the neutrinos emitted in the electron capture of ^{152}Eu all had a helicity of $\mathcal{H} = -1$, i.e. the projection of the spin is anti-parallel to the impulse of the neutrino (*left-handed neutrino*) [Gol58], while for anti-neutrinos $\mathcal{H} = +1$.

This means that the negative result of Davis' experiment does not necessarily mean ν and $\overline{\nu}$ are different particles, it is also possible that they only behave differently due to their different helicities.

Another groundbreaking experiment in neutrino physics was launched by Raymond Davis *et al.* in the Homestake gold mine in 1967 [Dav68]: in a tank containing 390,000 liters of liquid $CdCl_2$, he used the neutrino capture reaction

$$^{37}Cl + \nu_e \rightarrow {}^{37}Ar + e^- \tag{2.6}$$

not only to detect neutrinos from the sun, but also to measure the solar neutrino flux. The measured rate was three times smaller than the standard solar models predicted. This discrepancy was the origin of the so-called *solar neutrino problem* [Dav03]. In the following years, other experiments (SAGE [Abd99], GALLEX [Ham99], GNO [Alt05]) also observed the solar neutrino deficit.

2.2 Neutrino Oscillations

The discrepancy between the flux of electron neutrinos from the sun predicted by the solar standard model and the rate determined experimentally can be explained by *neutrino oscillations*, the conversion of neutrinos from one flavor into another after propagating a macroscopic distance.

This effect was first proposed by Bruno Pontecorvo who suggested that the electron neutrino might be a combination of different neutrino mass eigenstates, which could lead to flavor oscillations [Gri69]. Subsequently, Lincoln Wolfenstein [Wol78], Stanislav Mikheyev and Alexei Smirnov [Mik86] proposed a mechanism for resonant enhancement of neutrino oscillations in the sun, the MSW effect, that can account for the solar neutrino deficit observed by the experiments.

The solar neutrino experiments are not the only indication for neutrino oscillations. Another hint is the observation of muon flavor disappearance in the flux of atmospheric and reactor neutrinos [Jun01], [Egu03], which can also be explained by neutrino oscillations.
The theory of neutrino oscillations is briefly introduced in the following section.

2.2.1 Mechanism of Neutrino Oscillations

The neutrino flavor eigenstates $|\nu_a\rangle$ with $a = e, \mu, \tau$ and the mass eigenstates $|\nu_i\rangle$ with $i = 1, 2, 3$ are connected by a unitary mixing matrix

$$|\nu_a\rangle = \sum_i U_{ai} \cdot |\nu_i\rangle. \tag{2.7}$$

A neutrino created in certain flavor state $|\nu_a\rangle$ becomes a superposition of all flavors after travelling some time t. The probability to find the neutrino in a flavor state $|\nu_b\rangle$ after it travelled a distance $L \approx c \cdot t$ is given by

$$|\langle \nu_b | \nu_a(L) \rangle|^2. \tag{2.8}$$

The oscillations of solar ν_e and atmospheric ν_μ can be explained separately by considering mixing between two flavor states and two mass states [Kin07]

$$\begin{pmatrix} \nu_a \\ \nu_b \end{pmatrix} = \begin{pmatrix} \cos\theta & \sin\theta \\ -\sin\theta & \cos\theta \end{pmatrix} \begin{pmatrix} \nu_1 \\ \nu_2 \end{pmatrix}, \tag{2.9}$$

where θ is the mixing angle. For non-zero θ, the probability for the neutrino to change flavor is [Dor08]

$$\begin{aligned} P(\nu_\alpha \to \nu_\beta) &= \sin^2 2\theta \sin^2 \left(\Delta m^2_{12} \frac{L}{4E} \right) \\ &= \sin^2 2\theta \sin^2 \left(1.27 \Delta m^2_{12}[\mathrm{eV}^2] \frac{L\ [\mathrm{km}]}{E\ [\mathrm{GeV}]} \right) , \end{aligned} \tag{2.10}$$

where E is the average energy of the mass eigenstates and $\Delta m^2 = m_1^2 - m_2^2$. Obviously, neutrino oscillations can only take place if $\Delta m^2 \neq 0$, which means that at least one of the two involved neutrinos has to have a non-zero mass.

For most experiments this approximation will suffice. However, the complete picture is generated by three-flavor mixing.

For three neutrino flavors, ν_e, ν_μ and ν_τ, the unitary mixing matrix U becomes a 3×3 matrix:

$$\begin{pmatrix} \nu_e \\ \nu_\mu \\ \nu_\tau \end{pmatrix} = \begin{pmatrix} U_{e1} & U_{e2} & U_{e3} \\ U_{\mu 1} & U_{\mu 2} & U_{\mu 3} \\ U_{\nu 1} & U_{\nu 2} & U_{\nu 3} \end{pmatrix} \begin{pmatrix} \nu_1 \\ \nu_2 \\ \nu_3 \end{pmatrix} . \tag{2.11}$$

U is called the *Pontecorvo-Maki-Nakagava-Sakata (PMNS) matrix* and can be expressed in terms of three mixing angles and three phases:

$$U = \begin{pmatrix} 1 & 0 & 0 \\ 0 & c_{23} & s_{23} \\ 0 & -s_{23} & c_{23} \end{pmatrix} \begin{pmatrix} c_{13} & 0 & s_{13} e^{-i\delta} \\ 0 & 1 & 0 \\ -s_{13} e^{i\delta} & 0 & c_{13} \end{pmatrix} \begin{pmatrix} c_{12} & s_{12} & 0 \\ -s_{12} & c_{12} & 0 \\ 0 & 0 & 1 \end{pmatrix} \begin{pmatrix} e^{i\alpha_1/2} & 0 & 0 \\ 0 & e^{i\alpha_2/2} & 0 \\ 0 & 0 & 1 \end{pmatrix}, \tag{2.12}$$

where $s_{ij} = \sin\theta_{ij}$ and $c_{ij} = \cos\theta_{ij}$ represent the sines and cosines of the three mixing angles, and δ, α_1 and α_2 are CP-violating phases. The *Majorana phases* α_1 and α_2 are only present if the neutrinos are Majorana particles. The first matrix contains the parameters relevant for atmospheric neutrino oscillations, the second for reactor neutrino oscillations, and the third for solar neutrino oscillations [Dor08].

For three neutrino flavors, two independent square mass differences Δm^2_{12} and Δm^2_{23} can be defined. The results from current experimental data indicate that $\Delta m^2_{12} \approx 10^{-4} eV^2$ and $\Delta m^2_{23} \approx 10^{-3} eV^2$ [Dor08]. Since neutrino oscillations depend only on the square mass differences, they contain no information on the absolute value of the neutrino mass. While the sign of Δm_{21} is known from the MSW effect,

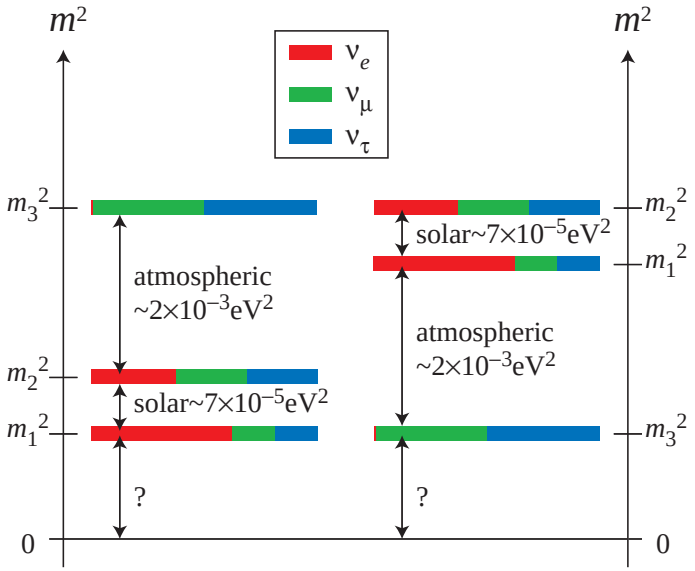

Figure 2.2: The two possible mass spectra for normal (left) and inverted (right) hierarchy. The color scheme of the mass eigenstate bands represent the probability of finding a certain flavor eigenstate ν_e, ν_μ and ν_τ in the respective mass eigenstate. Figure taken from [Kin07].

the sign of Δm_{23} is unknown. Therefore, two patterns are possible for the mass spectrum: the two states ν_1 and ν_2 are relatively closely spaced, while the third state ν_3 can either be heavier (*normal hierarchy*) or lighter (*inverted hierarchy*), as shown in figure 2.2.

2.3 Absolute Neutrino Mass Measurements

Since neutrino oscillation experiments are not sensitive to the absolute neutrino mass scale and to the two Majorana phases in the PMNS matrix, other experimental approaches are used to study some of those quantities:

- cosmological observations;
- β decay experiments;
- neutrinoless double beta decay ($0\nu\beta\beta$) experiments (which will be discussed in chapter 3).

Limits from Cosmology

Cosmological observations can be used to probe the sum of all neutrino mass eigenstates, $m_{\text{cosmo}} = m_1 + m_2 + m_3$, since all massive neutrinos contribute to the cosmological matter density Ω_m.
Neutrinos decoupled from the electromagnetic plasma at a temperature of a few MeV in the early universe, shortly before electron-positron annihilation. Their temperature is only ≈ 0.714 times the photon temperature [Han95]. This ratio links the total neutrino number density to the photon number density. The neutrino density, Ω_ν, is a parameter in the standard model of cosmology that is related to the sum of neutrino masses:

$$\Omega_\nu h^2 = \frac{m_{cosmo}}{93.5eV}, \tag{2.13}$$

where $h \approx 0.7$ is the Hubble parameter in units of (100km/s Mpc). The measured expansion rate of the universe and its observed age yield $\Omega_\nu h^2 \lesssim 0.4$, which gives a model-independent constraint of $m_{cosmo} \lesssim 40eV$ [Raf97].

Cosmic Microwave Background (CMB) data allows to further constraint the sum of neutrino masses to $m_{cosmo} < 2.6eV$ using the standard model of cosmology. Stronger limits on m_{cosmo} can be derived from combining Cosmic Microwave Background measurements with Large Scale Structure surveys and Lyman-alpha forest data. A present limit on the sum of neutrino masses from such a combined approach is $m_{cosmo} \lesssim 0.5eV$ at 99% confidence level [Str10].

Beta Decay

Another technique for direct neutrino mass measurements is to investigate the endpoint of the electron energy spectrum in β decay. The quantity that can be probed like this is

$$m^2_{\nu_e} = \sum_i |U^2_{ei}| m^2_i \tag{2.14}$$

Presently, the best sensitivity is obtained using tritium decay

$$^3H \rightarrow {}^3He + e^- + \bar{\nu_e} \;\; (Q = m_{^3H} - m_{^3He} = 18.6eV). \tag{2.15}$$

The maximum energy the electron can have is $Q - m_{\nu_e}$. In the energy region close to the endpoint, the shape of the beta spectrum is sensitive to the neutrino mass. Massive neutrinos reduce the number of decays in the endpoint region, with a functional dependence on $m^2_{\nu_e}$. By fitting the measured shape of the beta spectrum

to a calculated shape, limits on $m^2_{\nu_e}$ can be set.

Experiments from Mainz[Kra05] and Troitsk[Bel95] determined an upper limit on the neutrino mass of $m_{\nu_e} \leq 2.1eV$ (Troitsk) and $m_{\nu_e} \leq 2.3eV$(Mainz).

Currently the KATRIN experiment is under construction, aiming at an improvement of the sensitivity limit by an order of magnitude down to $m_{\nu_e} < 0.2eV$. KATRIN is expected to start data taking in 2012 [Ott10].

3 Neutrinoless Double Beta Decay

The only known experimental approach sensitive to the nature of the neutrino - Dirac or Majorana - are neutrinoless double beta decay experiments. They probe the effective Majorana neutrino mass

$$|m_{ee}| = |\sum_i U_{ei}^2 m_i|^2. \tag{3.1}$$

The physics of $0\nu\beta\beta$ as well as experimental considerations and techniques for its use in neutrino mass measurements are discussed in this chapter.

3.1 Signature

There are a few nuclei for which normal β decay is energetically forbidden, but double beta decay ($2\nu\beta\beta$), i.e. a transition between two nuclei with the same mass that changes the nuclear charge by two units, is possible:

$$2n \rightarrow 2p + 2e^- + 2\bar{\nu_e}. \tag{3.2}$$

The Feynman diagram for $2\nu\beta\beta$ is shown in figure 3.1(a).
The spectrum of the electrons' energy is continuous like the single beta decay spectrum. Double beta decay is a second order weak process and therefore the decaying isotopes have very long lifetimes of the order of $10^{[}19]$years - $10^{[}21]$ years. Still, it has been observed for several isotopes, for example ^{100}Mo, ^{82}Se, ^{48}K, ^{76}Ge and ^{136}Xe [Ste09].

If neutrinos are Majorana particles, another process is possible in addition to the neutrino-accompanied double beta decay: the neutrinoless double beta decay,

$$2n \rightarrow 2p + 2e^-. \tag{3.3}$$

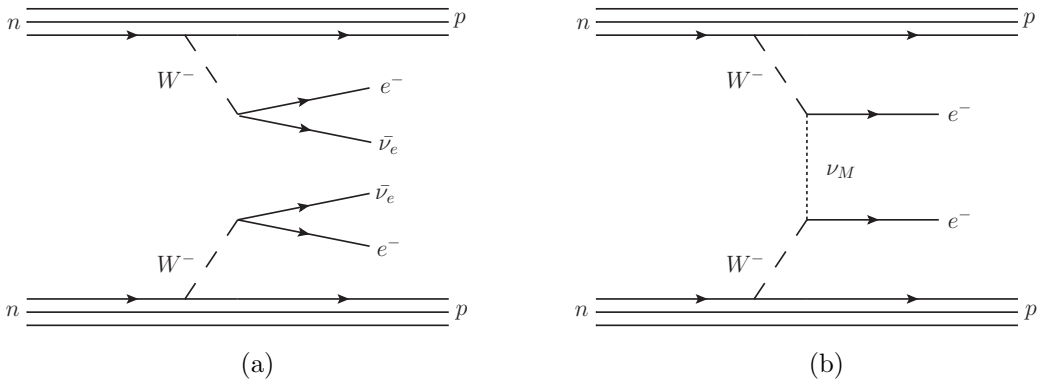

Figure 3.1: Feynman diagrams for (a) neutrino-accompanied and (b) neutrinoless double beta decay.

In this case a neutrino can be exchanged in the vertex. The Feynman diagram for this process is displayed in figure 3.1(b). The kinetic energies of the electrons add up to a mono-energetic line at the energy of the Q-value of the decay.

Figure 3.2 shows the kinetic energy spectrum of the electrons emitted in $2\nu\beta\beta$ and $0\nu\beta\beta$ decay.

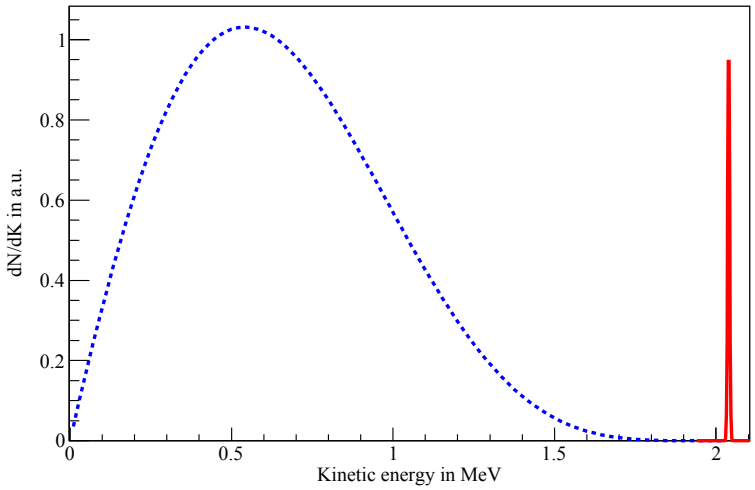

Figure 3.2: Illustration of the spectra of the sum K_e of the electrons' kinetic energies for the ^{76}Ge $2\nu\beta\beta$ decay (dotted blue curve) and $0\nu\beta\beta$ decay (red curve), not to scale. The spectra are convolved with an energy resolution of 0.3%.

$0\nu\beta\beta$ decay can only take place if neutrinos are Majorana particles. In addition, a chirality flip of the exchanged neutrino has to occur. This can be induced by a mass term. Therefore $0\nu\beta\beta$ decay can provide information on the absolute mass of the neutrinos. The decay rate is proportional to the square of the effective Majorana mass m_{ee} [Ste09]:

$$T_{1/2}{}^{-1} = \mathcal{G}^{0\nu} \cdot \left|\mathcal{M}^{0\nu}\right|^2 \cdot m_{ee}^2, \tag{3.4}$$

where $\mathcal{G}^{0\nu}$ is a known phase space factor and $\mathcal{M}^{0\nu}$ is the matrix element for the nuclear transition. This nuclear matrix element has to be calculated theoretically and varies by a factor of 2 - 3 in different calculations, which introduces theoretical uncertainties in the calculation of the effective Majorana mass [Ell02].

Neutrinoless double beta decay could also provide information on the mass hierarchy of neutrino mass eigenstates, since the electrons couple mostly to the first two mass states. If the mass of the lightest mass eigenstate is smaller than $\approx 10^{-2}eV$ and $|m_{ee}|$ can be measured with a sensitivity of 10 meV, information on the sign of Δm_{23}^2 can be deduced. Figure 3.3 shows the effective mass versus the minimum mass of the lightest mass eigenstate.

3.2 Challenges

In order to obtain a good sensitivity in the measurement of the effective Majorana mass, various requirements have to be met:

- Because of the low rate of $0\nu\beta\beta$ decay, a large number of source nuclei and a high detection efficiency are needed.

- A good energy resolution is needed, to obtain a good signal to background ration and also in order to be able to distinguish between the $0\nu\beta\beta$ signal and the tail of the $2\nu\beta\beta$ spectrum.

- A low background index in the region of interest is especially important, since the sensitivity is determined by the statistical precision of the background determination (the square root of the background level): if the number of signal events is smaller than the fluctuations in the background, no discovery can be made.
  Since the number of background counts increases linearly with measurement time, the sensitivity on the decay rate scales as the square root of time. From

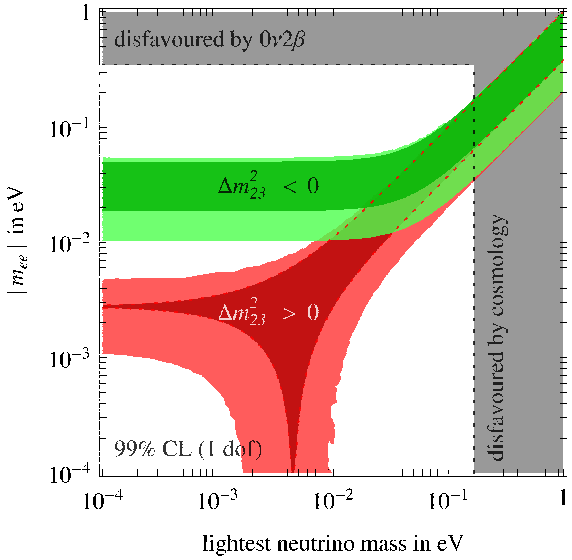

Figure 3.3: 99% CL expected ranges as function of the lightest neutrino mass for $|m_{ee}|$ probed by $0\nu2\beta$ (figure taken from [Str10]). $\Delta m^2_{23} > 0$ corresponds to normal hierarchy ($m_{\text{lightest}} = m_1$) and $\Delta m^2_{23} < 0$ corresponds to inverted hierarchy ($m_{\text{lightest}} = m_3$). The inner (outer) bands correspond to calculations without (with) 3σ-uncertainties on the oscillation parameters. The dark shaded regions show the ranges excluded by previous experiments and cosmological considerations.

equation 3.4 it can be seen that the sensitivity in m_{ee} goes with the square root of the decay rate, and therefore as the fourth root of the time.

3.3 Neutrinoless Double Beta Decay Experiments

There are a number of past, present and future $0\nu\beta\beta$ decay experiments, studying different isotopes based on different detection techniques. Some of them are presented in this section.

3.3.1 Tracking Calorimeters

NEMO3

The Neutrino Ettore Majorana Observatory 3 experiment, NEMO-3, is installed at the Laboratoire Souterrain de Modane and has been taking data since February 2003. It is based on the direct detection of the two decay electrons using a tracking device and a calorimeter. The source for the decay are foils enriched in different

double beta emitting isotopes (^{100}Mo, ^{82}Se, ^{48}Ca, ^{96}Zr, ^{116}Cd, ^{130}Te and ^{150}Nd), the total mass of enriched material is ≈ 9 kg. After analysis of the data corresponding to 3.75 years, no evidence for $0\nu\beta\beta$ decay was found in any of the samples. The best limits on $0\nu\beta\beta$ decay have been established with ^{100}Mo ($T_{1/2} > 1.1 \cdot 10^{24}$ years at 90% C.L.) and ^{82}Se ($T_{1/2} > 3.6 \cdot 10^{23}$ years at 90% C.L.) [Bar10]. NEMO-3 is intended to continue collecting data until 2011.

SuperNEMO

NEMO-3 will be followed by SuperNEMO, based on the same experimental techniques but operating on a larger scale: It is planned to use ≈100 kg of source material (20 modules, each containing 5 kg of isotope source), either ^{82}Se or ^{150}Nd. SuperNEMO aims at a sensitivity of 10^{26} years for the $0\nu\beta\beta$ half-life (down to $\sim$ 50 meV in the effective Majorana neutrino mass). The construction of the first module is expected to start in 2010 [Shi10].

3.3.2 Bolometers

Cuoricino and CUORE

Cuoricino uses cryogenic detectors to look for the $0\nu\beta\beta$ decay of ^{130}Te. An array of 62 TeO_2 bolometers with an active mass of 40.7 kg is operated at ≈ 10 mK at the Laboratori Nazionali del Gran Sasso (LNGS) in Assergi, Italy. Cuoricino started taking data in 2003. Until now, no evidence for $0\nu\beta\beta$-decay was observed and a limit of $T_{1/2} > 3.0 \cdot 10^{24}$ years at 90% C.L. has been set [Arn08].

Cuoricino will be followed by a larger scale experiment: the Cryogenic Underground Observatory for Rare Events, CUORE [Sis10], which will consist of 988 TeO_2 cryogenic detectors containing 200 kg of ^{130}Te . The experiment is presently being built in the Gran Sasso Underground Laboratory and is expected to start data taking in 2012.

3.3.3 Scintillation Calorimeters

EXO

The Enriched Xenon Observatory [Dol09], EXO, is an experiment designed for the search for $0\nu\beta\beta$ decay using the isotope ^{136}Xe. The first experimental phase, a detector using 200 kg of xenon enriched to 80% in ^{136}Xe in a low-background Time

Projection Chamber, is currently undergoing final commissioning. The experiment is located in an underground laboratory at the Waste Isolation Pilot Plant, a salt mine with an overburden of $\approx$ 1600 m water equivalent. Future plans envision the detection of the daughter ion ^{136}Ba correlated with the decay to eliminate all background from the $2\nu\beta\beta$ decay.

3.3.4 Semiconductor Detectors

COBRA

The COBRA experiment, situated at LNGS, uses a large amount of CdZnTe room temperature semiconductors. There are nine double beta emitters within the CdZnTe detector, five of which can decay via $2\nu\beta\beta$ decay, and four of them via either double electron capture, a combination of a positron emission with electron capture, or double positron emission. Limits on $0\nu\beta\beta$ decay for all seven isotopes were obtained (see [Blo07]). The first layer of 16 detectors was installed in summer 2006, with the full array of 64 detectors, corresponding to $\approx$ 0.42 kg of CdZnTe, starting data taking in autumn 2008. At present the experiment is revised to achieve a lower background level [Zub10].

IGEX

The International Germanium EXperiment, IGEX, was build for the search of $0\nu\beta\beta$ decay in ^{76}Ge employing HPGe detectors enriched to 86% in ^{76}Ge, with a total active mass of $\approx$ 5.3 kg. The experiment was located at the Canfranc underground laboratory under 2450 m water equivalent and took data from 1991 to 2000, from which a limit on the half-life of $T_{1/2} \leq 1.57 \cdot 10^{25}$ years was deduced [Aal02].

Heidelberg-Moscow

The Heidelberg-Moscow experiment used five germanium detectors with a total active volume of 10.96 kg, enriched to 86% – 88% in ^{76}Ge. The experiment ran from 1990 to 2003 at LNGS. Based on the data taken between 1990 and 2000, a limit on the $0\nu\beta\beta$ decay half-life of $T_{1/2} \leq 1.9 \cdot 10^{25}$ years was set [KK01a].

In a later publication, evidence for $0\nu\beta\beta$ decay was claimed by parts of the Heidelberg-Moscow collaboration [KK01b], reporting a half-life of $T_{1/2} = (0.8 - 18.3) \cdot 10^{25}$ years at 95% C.L. with a best value of $1.5 \cdot 10^{25}$years. The claim was re-

newed after re-analysis of the total data from 1990 to 2003 with $T_{1/2} = 2.23^{+0.44}_{-0.31} \cdot 10^{25}$ years [KK06].

This claim is controversial, mainly because the understanding of the background is still under debate [Str10], [Kir10]. New germanium $0\nu\beta\beta$ decay experiments with improved background suppression like MAJORANA [Aal05] and GERDA aim at verifying or rejecting the claim. The GERDA experiment is described in chapter 4.

4 The GERDA Experiment

The GERmanium Detector Array, GERDA [Abt04], is an experiment designed to search for $0\nu\beta\beta$ decay in ^{76}Ge. It is located in the underground laboratory Laboratori Nazionali del Gran Sasso (LNGS) in L'Aquila, Italy. The main goal of the experiment is to probe the $0\nu\beta\beta$ of ^{76}Ge with a sensitivity of $T_{1/2} > 2 \cdot 10^{26}$ years at 90 % confidence level, which corresponds to a range of <0.09 eV - 0.29 eV within $\approx$ 3 years [Sch05]. This will allow to test the claim for evidence for $0\nu\beta\beta$ decay made by parts of the Heidelberg-Moscow collaboration. If the claim is rejected, the low background index in the region of interest that GERDA aims for will make it possible to set an improved lower limit on the half-life of the $0\nu\beta\beta$ decay.

In this chapter, the design concept of GERDA and its background rejection techniques are briefly discussed. In the last section, the current status is described.

4.1 Concept of GERDA

GERDA is designed to be operated in two phases. In *Phase I*, the existing HPGe detectors enriched in ^{76}Ge from the Heidelberg-Moscow and IGEX experiments will be reused. Due to intrinsic ^{60}Co contamination of those detectors, the envisioned background level for this phase of GERDA is 10^{-2} events/(kg·keV·year).

In *Phase II* new HPGe detectors from enriched germanium, specially designed and produced for GERDA, will be deployed. One possible option for the Phase II detectors are segmented detectors. The aspired background level for Phase II is 10^{-3} events/(kg·keV·year).

As explained in section 3.2, a low background index in the energy range of interest is very important to be able to probe the $0\nu\beta\beta$ decay with a good sensitivity. The design of the GERDA experiment makes use of a number of techniques to reduce background. The combination of these techniques leads to the setup shown in figure 4.1.

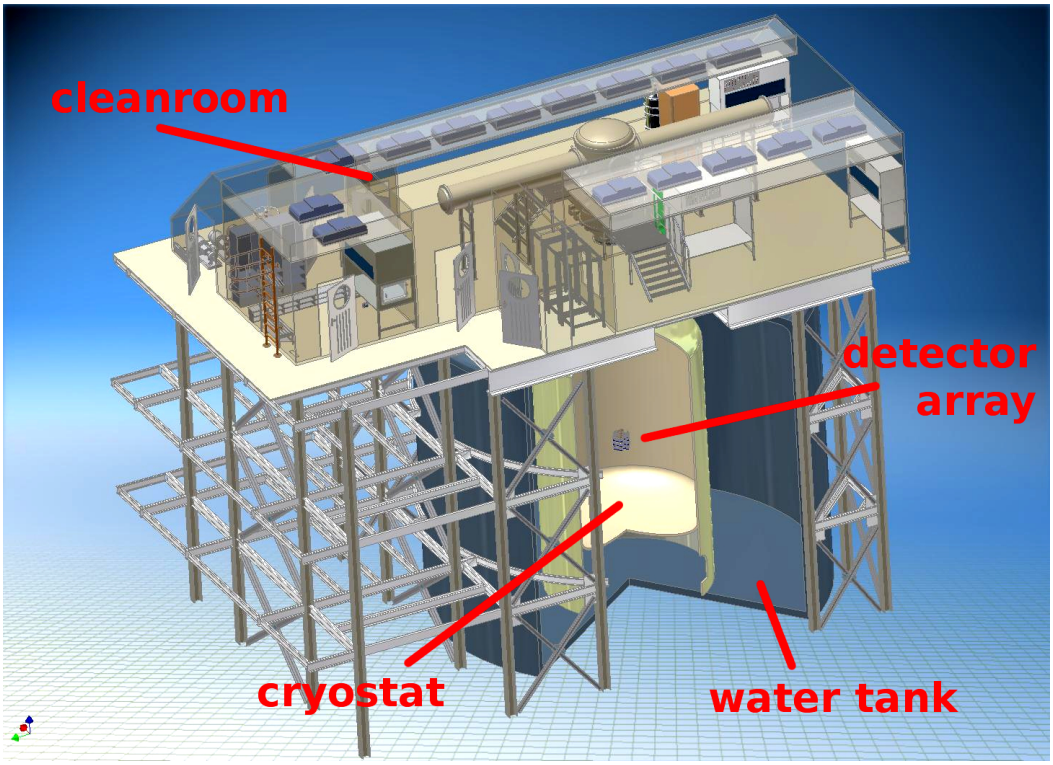

Figure 4.1: Setup of the GERDA experiment. An array of germanium detectors is submerged in liquid argon inside a cryostat, surrounded by a water tank. A lock system in the clean room on top of the structure provides access to the detectors.

Underground Location

GERDA is located at LNGS, under an average rock overburden of approximately 3400 m of water equivalent. This amount of rock blocks cosmic ray protons and neutrons completely, while the flow of cosmic ray muons is reduced by a factor of 10^6 compared to the surface [Arp92].

Cryostat

The germanium detectors for GERDA will be immersed directly in liquid argon inside a stainless steel cryostat with a copper lining on the inside. The cryostat has a diameter of 4.2 meter and holds 70 m^3 of liquid argon. The liquid argon serves two purposes: it cools the germanium detectors, and it acts as a shield against γ-rays, e.g. originating from the cryostat itself. Cryoliquids can be produced with very high purity. Nearly all massive background components are removed from the

direct vicinity of the detectors.

Water Tank and Muon Veto

The cryostat is surrounded by a stainless steel tank with a diameter of 10 m, filled with ultra-pure water. The water serves as a shield against γ-radiation from the outside and absorbs neutrons origination from the surrounding rock.

Furthermore, the water tank helps in reducing the muon underground further: the Čerenkov radiation induced by muons transversing the water tank is detected by photomultiplier tubes installed on the walls of the water tank. The walls of the water tank are lined with VM2000 wavelength shifting and reflecting foil to increase the detection efficiency. In addition to this, plastic scintillator plates are placed on top of the clean room to detect the muons entering the cryostat through its neck.

Cleanroom

When a HPGe detector is exposed to air, its surface can collect dust containing radioactive isotopes, in particular ^{238}U and ^{232}Th. If for example ^{210}Pb from the ^{238}U decay chain undergoes an α decay and only part of the energy is detected, because the remainder of the decay energy was deposited in the detector's dead layer, this may result in a signal close in energy to the Q-value of the ^{76}Ge $0\nu\beta\beta$ decay. Thus the preparation and insertion of the detectors has to be done in a dust free environment. To ensure this, a class 10,000 cleanroom has been built on top of the cryostat. The handling and mounting of the detectors will be performed in a glove-box or in class 100 flow-boxes inside the clean room (figure 4.2(a)). After assembling, the strings with the detectors can be lowered into the cryostat through a lock system.

Detector Array

The HPGe detectors used in the experiment are placed close together. This is important for improving the efficiency of identifying background events, in which particles scatter multiple times and deposit energy in more than one detector. The detectors will be chained together vertically into strings (see figure 4.2(b)). The detector strings are grouped together into an array in a way such that the horizontal distance between the detector centers is 9 cm.

Knowing the position of all the interactions of an event within the detector array helps to identify background events: The two electrons emitted in $0\nu\beta\beta$ decay will

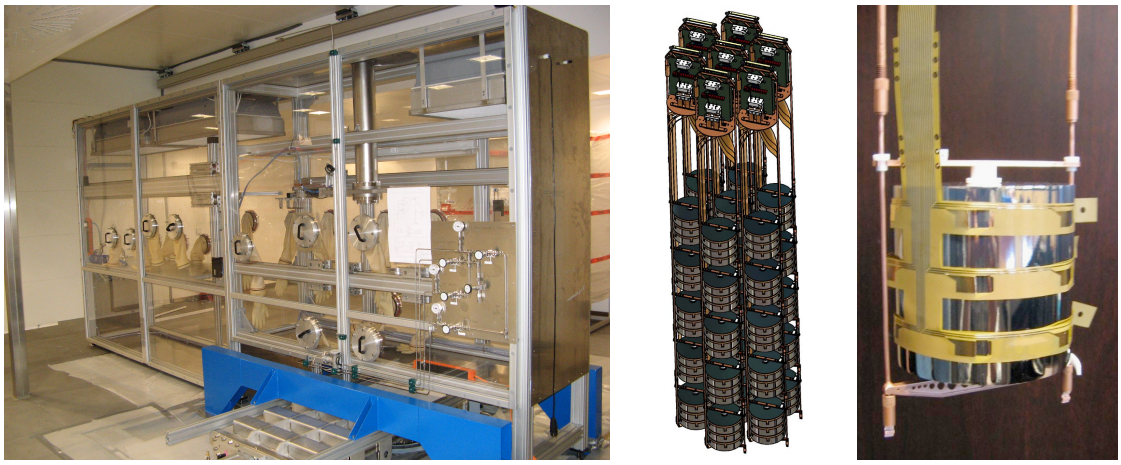

(a) (b) (c)

Figure 4.2: (a) Glove box inside the GERDA clean room, (b) drawing of a Phase II detector array with segmented detectors, (c) a prototype detector in its copper holder.

their deposit energy predominantly within 1 mm, while multiple Compton scattering is likely to deposit energy in more than one detector (Phase I) or in different volumes spatially separated by $\mathcal{O}(cm)$ inside a single detector (Phase II).

To reduce background radiation as much as possible, all components of the detector string have to be reduced to a minimum of mass and radio pure materials need to be used. All materials are screened and have to fulfill strict cleanliness requirements. Close to the detectors, mainly copper and Teflon are used, since those two materials can be produced with relatively high radio purity. Figure 4.2(c) shows a Phase II prototype detector and its holder, which consists of only 30 g copper and 7.5 g Teflon.

4.2 Status as of Summer 2010

By summer 2010, the GERDA experiment has reached the commissioning phase. The construction of the water tank, the cryostat and the clean room have been finished.

The cryostat was cooled down and filled with liquid argon in November and December 2009. The water tank's drainage system has been tested several times and

Figure 4.3: The first string deployed in GERDA during mounting in the glove box.

the tank has been filled. The commissioning lock arrived at LNGS in March 2010 and has been installed on the glove box in the clean room.

On June 2^{nd} 2010, the first string with 3 non-enriched germanium detectors has been deployed. It will be operated for a few month in order to measure the background of the full GERDA setup before the enriched Phase I detectors are deployed.

5 Particle Detection with High Purity Germanium Detectors

This chapter gives an introduction to the operating principle of germanium detectors. The interactions of ionizing particles with matter in the relevant energy region are discussed. Properties of HPGe detectors are briefly reviewed. The chapter closes with a short introduction of the detectors and detector test facilities used to take the data for this thesis.

5.1 Detection of Ionizing Particles

Particles and radiation can be detected via their interactions in matter. For high purity germanium detectors, the relevant interactions are those at energies of the order of keV up to several MeV.

5.1.1 Interactions of Electrons and Positrons in Matter

At energies up to several MeV, electrons and positrons passing through matter primarily lose energy through collisions (leading to ionization or excitation) and bremsstrahlung. The total energy loss of electrons and positrons is therefore composed of two parts:

$$\left(\frac{dE}{dx}\right)_{total} = \left(\frac{dE}{dx}\right)_{coll} + \left(\frac{dE}{dx}\right)_{brems}. \tag{5.1}$$

The collisional energy loss can be described as [Gru08]

$$-\frac{dE}{dx} \propto \frac{Z}{A\beta^2}\left[\ln\left(\gamma\frac{m_e c^2}{I} - \beta^2 - \delta\right)\right], \tag{5.2}$$

where m_e is the electron mass, c is the speed of light, Z and A are the atomic number and atomic weight of the absorbing material, β is the velocity of the interacting

particle in units of c, γ is its Lorentz factor, I and δ are absorber specific constants.

Bremsstrahlung in the electric field of the nucleus can play an important role in the energy loss of electrons and positrons, due to of their small mass. The energy loss due to bremsstrahlung can be written as [Gru08]

$$-\frac{dE}{dx} \propto \alpha E_e \frac{Z^2}{A} \ln\left(\frac{183}{Z^{1/3}}\right), \tag{5.3}$$

where α is the fine structure constant and E_e the energy of the electron or positron.

This contribution to the total energy loss is relatively small at energies of a few MeV or less, but increases rapidly with larger energies. The energy at which the bremsstrahlung contribution is equal to the collisional loss is called *critical energy*. The critical energy depends on the absorber material. For germanium, the critical energy is $E_{crit} = 18.16\ MeV$ for electrons and $E_{crit} = 17.58\ MeV$ for positrons [Ams08].

If the incident particle is a positron, it will annihilate with an electron of the absorber material after losing its kinetic energy and two 0.511 MeV photons are emitted in opposite directions [Kno00].

5.1.2 Interactions of Photons in Matter

The total probability for a photon interaction in matter per unit length, the *total absorption coefficient* μ, depends on E_γ and Z of the absorber material. It is composed of three contributions, photoelectric effect (σ_{photo}), Compton scattering ($\sigma_{Compton}$) and pair production (σ_{pair})[Leo92]:

$$\mu = \frac{N_A \rho}{A} \left(\sigma_{photo} + \sigma_{Compton} + \sigma_{pair}\right), \tag{5.4}$$

where ρ is the density of the absorber material and $N_A = 6.02 \cdot 10^{23}\text{mol}^{-1}$ is the Avogadro constant. The mass attenuation coefficient, which is equal to the absorption coefficient divided by the density, for germanium is shown in figure 5.1. In germanium, photons with energies below a few 100 keV interact mostly through the photoelectric effect, while for energies ranging from a few 100 keV to a few MeV Compton scattering is the dominating process. Above $\approx$ 10 MeV pair production becomes the dominant process.

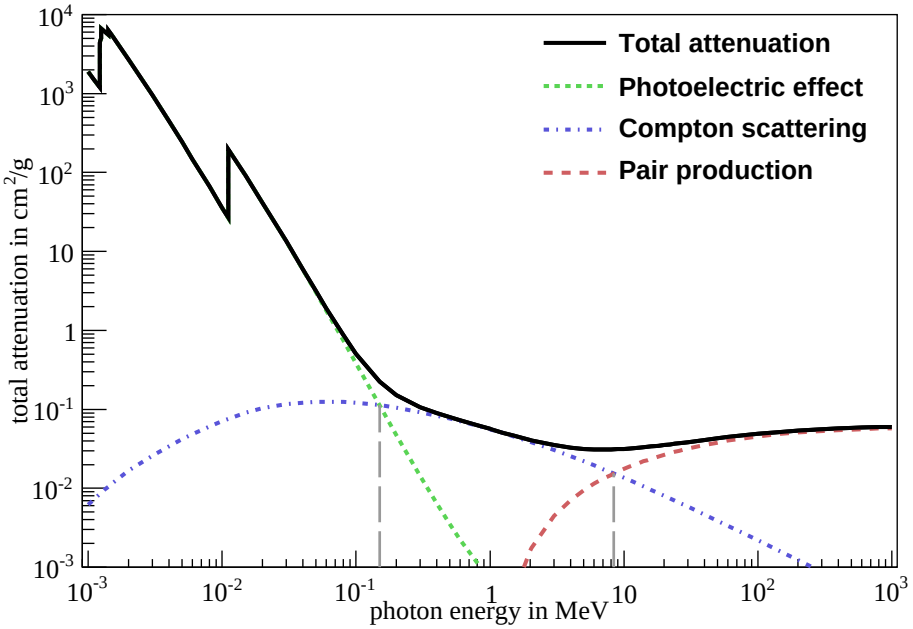

Figure 5.1: Mass attenuation coefficient for germanium [Ber]. The dashed line at 0.15 MeV (8.4 MeV) marks the energy where the cross-section of Compton scattering and photoelectric effect (pair production) are equal.

In the photoelectric effect, a photon is absorbed by an atomic electron which is then ejected from the atom. The energy of this electron is

$$E_e = E_\gamma - E_B, \tag{5.5}$$

where E_B is the binding energy of the electron. The cross section of the photoelectric effect decreases with increasing initial energy of the photon. Furthermore, it also depends on the atomic number Z of the absorber. At MeV energies, this dependence goes as Z to the 4th or 5th power [Leo92].

Compton scattering is the scattering of photons on free electrons or bound electrons whose binding energies are low with respect to the photon energy. The photon is deflected by an angle θ with respect to its incoming direction and transfers a portion of its energy to the electron. The energy of the scattered photon can be expressed as [Leo92]

$$E_{\gamma'} = \frac{E_\gamma}{1 + \frac{h\nu}{m_e c^2}(1 - cos\theta)}. \tag{5.6}$$

The energy transfer is maximal when $\theta = 180°$. If the incident photon leaves the detector with reduced energy, the event will contribute to the continuous background

of the energy spectrum.

Pair production can occur if the photon has an energy of at least 1.022 MeV (twice the electron mass): the photon is transformed into an electron-positron-pair in the electric field of a nucleus. The electron and the positron can be stopped in the absorber material. After the positron has lost its kinetic energy, it will annihilate to produce two photons, each with an energy of 511 keV.

5.1.3 Detector Efficiency

There are two types of efficiencies generally used to describe particle detector systems: the absolute efficiency and the intrinsic detection efficiency [Leo92].

The *absolute (or total) efficiency* is defined as the fraction of ionizing particles emitted by a source that are registered in the detector,

$$\varepsilon_{abs} = \frac{\text{particles registered}}{\text{particles emitted by source}} \ . \tag{5.7}$$

It is a function of the geometrical configuration of the experiment and the probability of an interaction in the detector.

The *intrinsic efficiency* is registered fraction of events out of those actually hitting the detector,

$$\varepsilon_{int} = \frac{\text{particles registered}}{\text{particles entering the detector}} \ . \tag{5.8}$$

It depends on the interaction cross-section of the radiation with the detector medium. Therefore, it depends on the type of the radiation, its energy and the properties of the detector material.

The fraction of radiation emitted by an external source that hits a certain point inside a detector is determined by two effects:

- The *inverse-square law*: The radiation is emitted radially from the source. It spreads out like the surface of a sphere ($4\pi r^2$), so the intensity of radiation passing through a certain area is inversely proportional to the squared distance to the source.

- *Attenuation*: While passing through the detector, particles can be removed from the beam through the interactions described above. The intensity of the

transmitted beam I is

$$I = I_0 e^{-\mu t} \tag{5.9}$$

where I_0 is the intensity before the absorber, μ the total attenuation coefficient, and t the thickness of absorber material that has to be passed [Kno00]. More attenuation takes place before the radiation reaches the detector volumes further away from the source. Since the attenuation coefficient depends on the energy, the effect is more pronounced for lower energies.

5.2 Working Principle of Semiconductor Detectors

The following section gives a brief overview over important characteristics of semiconductor detectors. For a more detailed discussion, see references [Kno00] and [Leo92].

One of the most important characteristics of a semiconductor, which distinguishes it from metals and insulators, is its narrow band gap. Materials are classified as semiconductors if their band gap is of the order of 1 eV.

The electronic properties of semiconductors are strongly affected by impurities: when impurities are introduced into a crystal, additional levels are created in the energy band structure. The electrically active impurities in a semiconductor are categorized as donors (e.g. materials from column V of the periodic table introduced in germanium or silicon crystal) or acceptors (atoms from column III). Donor impurities have energy states that lie in the band gap close to the conduction band (0.01 eV in germanium, 0.05 eV in silicon [Leo92]). Electrons in germanium crystals are easily thermally excited into the conduction band, resulting in a finite conductivity (n-type material). Similarly, acceptors have energy states close to the valence band (p-type) [Str95]. Intrinsically, any semiconductor material will have an excess of one type. By doping intrinsic semiconductor materials with acceptors (donors), p^+ (n^+) type materials can be obtained.

When forming a pn-junction, in its vicinity electrons from the n-type region will diffuse into the p-type region, and holes diffuse from the p-side to the n-side. This creates a *depletion region* in which almost no free charge carriers exist. By applying reverse bias (i.e. connecting the anode to the n-side and the cathode to the p-side), the width of the depletion region can be increased. Its thickness is a function of the applied bias voltage and the impurity concentration [Ebe08].

This depletion region forms the active volume for the detection of particles: When

ionizing radiation passes through the active region and electron-hole-pairs are created, the electrons and holes are swept out of the depletion region by the electric field. A charge that is proportional to the deposited energy can be detected at electrical contacts placed on either end of the junction [Leo92].

5.3 High Purity Germanium Detectors

The achievable net charge carrier density and the breakthrough voltage limit the size of the active volume that can be reached. To obtain a depletion width of several centimeters at a bias voltage on the order of a few kilovolts, a net impurity concentration of approximately 10^{10} atoms/cm^3 germanium is needed. Detectors that are made of such ultrapure germanium are called *High Purity Germanium (HPGe)* detectors.

5.3.1 Principles of High Purity Germanium Detectors

HPGe detectors can be made from an intrinsically p-type as well as from an intrinsically n-type crystal. The contacts are created by Lithium diffusion on one side (n^+ contact) and Boron implantation on the other side (p^+ contact). Common geometries for HPGe detectors are true coaxial and close-ended coaxial (see figure 5.2). The outer surface of the detector makes up one contact, the other electrode is fabricated on the surface of the inner bore-hole. The rectifying contact that forms the p-n-junction is typically placed on the outside. This has the benefits that a lower voltage is required to fully deplete the detector and that the electric field is larger on the outside, where most of the detection volume lies [Vet07]. To obtain a homogeneous electric filed, the surfaces of the detector are usually metallized.

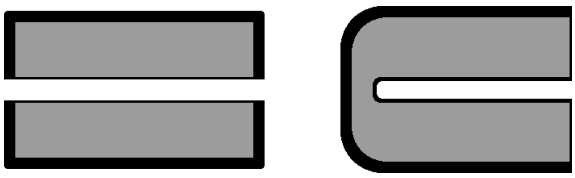

Figure 5.2: Coaxial detector geometries: true coaxial (left) and close-ended coaxial (right).

Operating temperature

At room temperature, germanium has a band gap of 0.7 eV. This means that electrons can easily be thermally excited from the valence band into the conduction band. Therefore, germanium detectors have to be operated at low temperatures, e.g. liquid nitrogen temperature (77 K), otherwise high leakage currents make the operation of the detector impossible [Leo92].

Energy resolution

An important property of a detector is its energy resolution, which describes the extent to which two close lying energies can be distinguished. Ideally, a monoenergetic beam of radiation would show up as a sharp line in the energy spectrum. In reality, a (usually Gaussian shaped) peak structure with finite width is observed. The full width at half maximum (FWHM) of the peak is a measure for the detector resolution.

The FWHM normally consists of contributions from statistical fluctuations, variations in the charge collection efficiency and the electronic noise. The FWHM can be described as [Kno00]

$$(\mathrm{FWHM})^2 = {W_D}^2 + {W_X}^2 + {W_E}^2, \tag{5.10}$$

where ${W_X}^2$ describes the statistical fluctuations, ${W_X}^2$ the charge collection inefficiency and ${W_E}^2$ the electronic noise.

The average energy required to produce an electron-hole pair in germanium is only $\varepsilon = 2.96eV$. This energy is larger than the band gap, because some energy is used to excite lattice vibrations instead of creating an electron-hole pair. The relatively small value of ε results in a reasonable number of charge carriers being created per keV, thus the statistical variations render it possible to achieve a better energy resolution with germanium than with most other semiconductors.

Since charge carrier creation and phonon excitation are not independent of each other, simple Poisson statistics cannot be used to calculate the variance in the number of created electron-hole-pairs. A correction factor, the *Fano factor*, has to be included. The Fano factor for germanium has been estimated to be $F \approx 0.1$. The contributions of the statistical fluctuations to the FWHM of a photo peak in

the energy spectrum can be described as [Ebe08]

$$W_D{}^2 = (2.35)^2 F\varepsilon E. \tag{5.11}$$

The second term, $W_X{}^2$, is due to the charge collection inefficiency. Charge carriers in semiconductors can be trapped by impurities that introduce energy levels near the middle of the band gap, e.g. gold, zinc or cadmium atoms. These traps can immobilize an electron or hole for a time that is long enough to prevent that the carrier drifts to the electrode and thus contributes to the measured pulse [Kno00]. The mean length a charge carrier can drift inside the semiconductor before trapping depends on the average drift velocity. Therefore, the amount of carrier loss due to trapping, and accordingly $W_X{}^2$, is influenced by both the volume of the detector and by the strength and shape of the electric field.

The third term, $W_E{}^2$, represents the way in which the electronic noise adds to the width of the photo peak in the energy spectrum. The most important contributions to the electronic noise are those hat occur at the beginning of the signal chain, because they will undergo the same amplifications as the signal. One type of noise that can contribute a substantial amount to $W_E{}^2$ are *microphonics*: mechanical vibrations transmitted to the preamplifier input, which can cause fluctuations in the capacitance and consequently in the output signal of the preamplifier. Other possible sources of noise are for example fluctuations in the leakage current of the detectors or thermal noise at the input stage of the preamplifiers, as well as electronic noise from the surroundings.

Segmented Detectors

Electrolithographic techniques for the segmentation of boron-implanted contacts have been developed to achieve position sensitivity in n-type germanium detectors [Gut90]. The segmentation allows to contact multiple areas on the surface of a detector and read them out separately.

5.3.2 Prototype Detectors

Segmented prototype HPGe detectors, the *Siegfried* detectors, were developed together with the manufacturer Canberra France[1]. The Siegfried detectors consist of n-type true coaxial cylindrical natural HPGe crystals. They are 18-fold segmented: 6-fold in the azimuthal angle, φ, and 3-fold in the height, z.

The specifications of the detectors used in the data taking for this thesis (Siegfried I and III) are summarized in table 5.1.

Parameter	*Siegfried* I	*Siegfried* III
Outer diameter (mm)	75.0	74.9
Inner diameter (mm)	10	10
Impurities (10^{10} cm^{-3})	0.70 - 1.35	0.61 - 1.35
Height (mm)	69.8	70.0
Operating voltage (V)	+3000	+4000
FWHM at 122 keV (keV)	0.99	1.10
FWHM at 1333 keV (keV)	1.99	2.25

Table 5.1: Detector specifications provided by Canberra-France.

For both detectors, the individual segments were contacted using Kapton printed circuit boards specifically developed for low-background purposes, like the one shown in figure 5.3(a).

Siegfried I was operated in a conventional vacuum teststand and has been characterized before [Abt07]. The segment numbering of the Siegfried I detector is shown in figure 5.3(b).

Siegfried III was operated immersed directly in liquid nitrogen. Contrary to Siegfried I, not all the segments of Siegfried III were fully metallized: for the segments in the top layer of the detector, the metallization was restricted to circular areas of roughly 10 mm diameter at the segment centers, where the contacts are placed. The purpose of this contact scheme was to examine the impact of such a partial metallization. This contact scheme was investigated as low background experiments such as GERDA might profit from a minimization of the amount of non-radiopure metal used. Figure 5.3(c) shows the segment numbering and metallization scheme of Siegfried III.

[1]CANBERRA France, chemin de la Roseraie 1, Parc des Tanneries, 67380 Lingolsheim

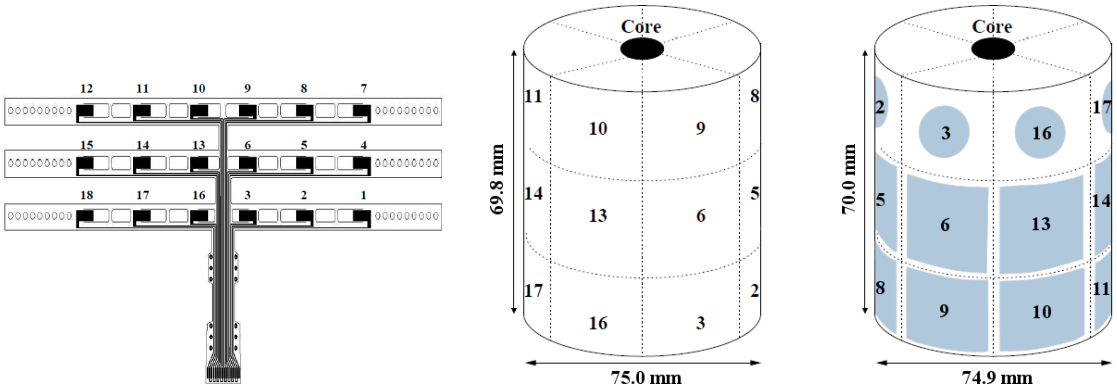

(a) (b) (c)

Figure 5.3: (a) Design of the Kapton cable used to read out the signals of the individual segments, (b) segmentation scheme of Siegfried I, (c) segmentation and metallization scheme of Siegfried III.

5.4 Detector Test Facilities

5.4.1 Cryostats and Front End

Different test facilities were used to examine the segmented prototype detectors in vacuum and immersed in liquid nitrogen.

Vacuum Cryostat

To examine the detectors in vacuum, a conventional vacuum test cryostat procured by Canberra-France was used. The detector is placed inside a two-walled aluminum vacuum can with a radius of 75 mm and a height of 116 mm on top of the dewar. The vacuum can is pumped down to 10^{-6} mbar before cool-down. A copper cooling finger is used as a thermal link between the detector and the cryogenic liquid. The temperature at the top of the cooling finger was monitored using a platinum resistance thermometer, a PT100. Between daily refilling cycles the temperature is stable around (-169 $\pm$ 3) °C.
A sketch of the setup can be seen in figure 5.4(a).

Charge sensitive preamplifiers of type PSC-823 procured by Canberra with a decay time of 50 μs and a nominal rise time of 20 ns were used to amplify the detector signals. The field effect transistor (FET) for the core signal that serves as the first amplification stage was placed inside the cryostat as close to the detector as feasible.

The FETs for the segment signals were incorporated into the preamplifier boards inside the copper ears on both sides of the vacuum can.

Gerdalinchen II

Gerdalinchen II (GII) is a special cryostat developed by the technical division of the Max-Planck-Institute for Physics to test the operation of segmented HPGe detectors immersed directly in cryogenic liquid under conditions resembling those in GERDA. GII consists of a two-walled cryogenic dewar inside a cylindrical aluminum tank. Up to three detectors can be mounted to a vertical stainless steel bar inside the dewar. A sketch of GII is shown in figure 5.4(b). Eight PT100 sensors are attached to different places inside the cryostat to monitor the level of the liquid nitrogen. The dewar is refilled every 24 to 48 hours.

The bias high voltage is applied via the AC coupled core contact. The HV filter and the coupling capacitance for the core are placed inside the dewar below the liquid level, roughly 20 cm from the core. The charge sensitive preamplifiers of type PSC-823 for core and segments are located inside copper preamplifier boxes at room temperature outside the dewar. One of these boxes is shown in figure 5.4(c). The signals from the 18 DC coupled segments are passed to the preamplifiers through the Kapton cable and approximately 50 cm of coaxial 50 Ohm SM50 habia cables, the distance from the core coupling capacitor to its preamplifier is roughly 60 cm. An 18-fold LEMO feed-through connects the single cables to the preamplifier box.

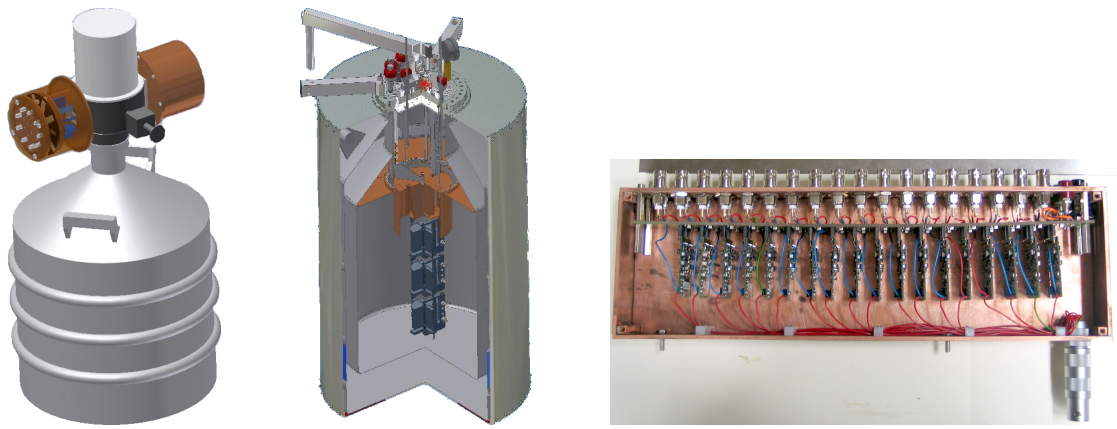

(a) (b) (c)

Figure 5.4: (a) Vacuum cryostat, (b) Gerdalinchen II, (c) preamplifier box.

The length of the cables results in the risk for extra noise due to pick-up of electronic noise, antenna effects and microphonics [Abt09].

A calibration source can be placed inside the dewar to perform scanning measurements: A tungsten collimator with a bore hole diameter of 2 mm and hole length of 25 mm is attached to a moveable holder. The collimator holder can be rotated around the detectors across a range of ≈80°in the azimuthal angle and moved over a range of 30 cm in the height. This range allows to cover the an entire row of segments (see figure 6.1(b)).

5.4.2 Data Acquisition

To digitize the preamplified signals, a Pixie-4 XIA system[2] was used, based on modules with four 14-bit ADCs each. The core signal was used to trigger the events. The energies of the signals were calculated using trapezoidal software filters. If the core energy was above a preset threshold, the energies for all channels were recorded. In addition to the energy and time information, it was also possible to record *pulse shapes*, i.e. the integrated charge at the preamplifiers over time. In pulse shape data, 300 samples of the amplitude of the integrated charge are recored with a sampling rate of 75 MHz, which corresponds to a bin width of 13.3 ns.

[2]XIA LLC, 31057 Genstar Rd., Hayward, CA 94544 USA

6 Reconstruction of the Energy Spectrum of a Floating Segment

During the installation of the Siegfried III detector, one of its top layer segments, segment 16, lost contact. The signals from this segment did not arrive at the preamplifier stage, as the transmission line was interrupted somewhere between the Kapton readout cable and the first preamplifier stage.

The effects caused by this and a method to reconstruct the energy information from the lost segment are discussed in this chapter.

6.1 Effects of a Floating Segment

If the signal line between the segment contact and the first preamplifier stage is interrupted, the charge carriers created inside the detector by incident radiation will still drift along the same trajectories as for a connected segment, until they reach the segment contact. The segment electrode and the transmission lines until the point of the interruption will charge up. Due to capacitive and inductive coupling either between individual detector segments, and also between individual transmission lines, mirror charges will be induced on neighboring electrodes. Unlike mirror charges induced by the drift of charge carriers in normally operating segments, the mirror charges caused by energy deposit in the floating segment will not disappear in the time window of the data acquisition, as the segment electrode can not be discharged. Instead, they will be mis-identified as energy deposit in the neighboring segments.

Since the couplings determine the amplitude of the mirror charges in the other segments, the amplitude ratios of the other segments will always be the same. In an ideal case, the sum of the signals in the other segments would be equal to the energy deposited in segment 16. In reality, some loss will occur due to charge dissipation. Therefore, the sum of the signals in the other segments is expected to be a constant

fraction less than one.

6.2 Experimental Setup

A 40 kBq ^{152}Eu source was located in the tungsten collimator inside the Gerdalinchen II teststand. In z-direction, the collimated source could be moved along the entire height of the detector: from z=170 mm, corresponding to the lower edge of segment 11, to z=240 mm, which corresponds to the top of segment 17. In φ, a range of $\approx$ 80°could be scanned, covering the segments 11, 14 and 17 completely. The collimator on its holder next to the detector is shown in figure 6.1(a). Figure 6.1(b) illustrates the definition of the z- and φ-coordinates and the surface area that could be scanned. The uncertainties in the source position are estimated to be $\pm$ 1 mm in z and $\pm$ 2° in φ.

6.2.1 Dataset

To demonstrate the possibility of energy reconstruction of events with energy deposit in segment 16, a dataset containing $\approx$ 4 million events was taken. The collimated ^{152}Eu source could not be rotated far enough to be positioned in front of the center of segment 16. Instead, it was chosen to aim it at the center of segment 14 (z=203

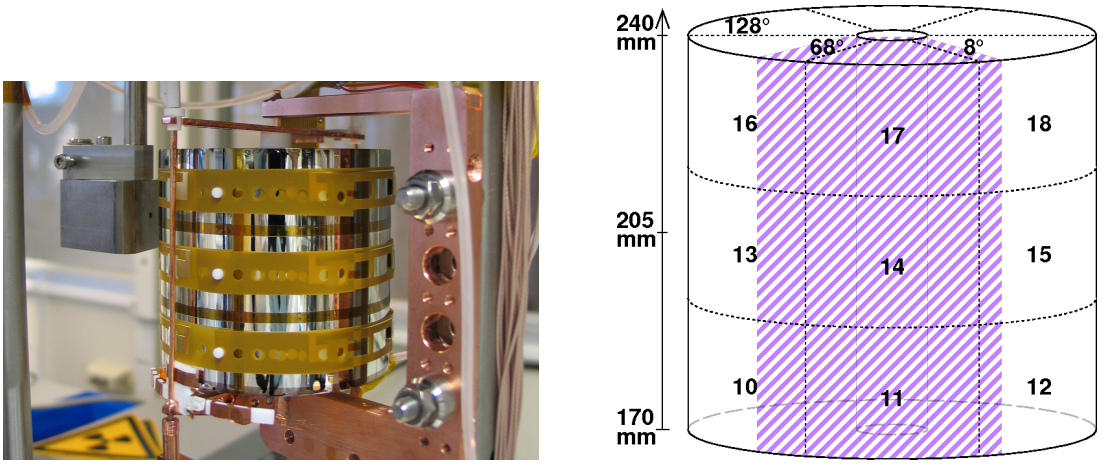

(a) (b)

Figure 6.1: Experimental Setup: (a) Siegfried III and the tungsten collimator, (b) definition of the detector coordinate system. The shaded area indicates the range that could be scanned.

mm, φ=38°), in the middle layer of the detector. For each event, energy and time information of the core and the 18 segments were recorded.

The energy resolutions of the core for this dataset as well as the peak-to-background ratios for different gamma energies are listed in table 6.1. Fitting the core resolution with equation 5.10 gives

$$\mathrm{FWHM} = \sqrt{\underbrace{(2.35)^2 \cdot 0.18 \cdot 2.96 \cdot (E_{core})}_{statistical\ variance} + \underbrace{2.0 \cdot (E_{core})^2}_{charge\ collection} + \underbrace{(4.1)^2}_{electronic\ noise}}\ keV. \quad (6.1)$$

Energy (keV)	FWHM_{core} (keV)	peak-to-background ratio
344.3	4.29 ± 0.17	0.2 ± 0.01
778.9	4.77 ± 0.05	0.9 ± 0.01
964.1	4.91 ± 0.03	2.2 ± 0.03
1112.1	5.13 ± 0.03	3.1 ± 0.05
1408.0	5.26 ± 0.02	40.3 ± 1.9

Table 6.1: Siegfried III core FWHM and peak-to-background ratios for different energies.

6.3 Observations

As expected, the pulses from energy deposits in segment 16 could be partly seen in energy spectra of the other segments, especially in the neighboring segments. In addition to the normal peaks in the energy spectrum corresponding to the ^{152}Eu decay, further peaks could be distinguished. That those peaks are due to an energy deposit in segment 16 could be confirmed by the investigation described below. They could be identified as ^{152}Eu lines shifted to lower energies by a factor R_{sci}, which had a different magnitude for the individual segments i, corresponding to the respective coupling.

Figure 6.2 shows an energy spectrum for segment 17, one of the direct neighbors of segment 16.

The energy deposited in segment 16 was always distributed over the other segments following the same pattern, as explained in 6.1. Figure 6.3 shows the segment energy plotted versus core energy for segment energies < 300 keV. This is the energy range in which the ^{152}Eu peaks induced in this segment by events with an energy

deposit in segment 16 were located. Most events are located in a band around a line with slope s=1. These are single segment events that occurred in the respective segment. In addition to this, another band appears that contains the signals induced by an energy deposit in segment 16. The slope of this second region is different for the individual segments, e.g. R_{sc-17} ≈0.18 for segment 17 (see figure 6.2 and table 6.2). It reflects the strength of the coupling between individual detector segments and between individual transmission lines, respectively. The events in this band correspond to be events with full energy deposit in segment 16.

In any event with energy deposit in segment 16, signals will be induced in all the other segments, according to the respective coupling. Events in which energy was deposited in segment 16 show up in another segments energy spectrum in one of four different ways:

I. single-segment events with energy deposit in segment 16 only;

II. events with partial energy deposit in segment 16 and no energy deposit in the corresponding, but additionally energy deposit in some other segment;

III. events with energy deposit in segment 16 and the corresponding segment:

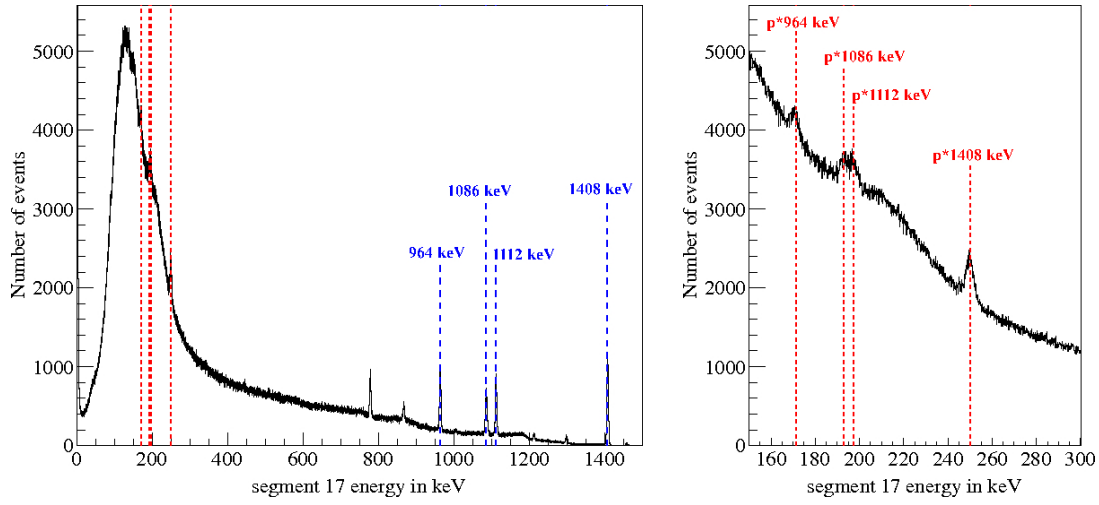

(a) (b)

Figure 6.2: Energy spectrum of segment 17. The dashed lines in (a) mark the positions of four lines in the ^{152}Eu spectrum, the dotted lines in (a) and (b) is a zoom into a low energy region, showing these lines shifted to lower energies by a factor of p≈0.18.

IV. events with energy deposit in segment 16, the corresponding segment and some other segment.

These cases are illustrated in figure 6.4 on the example of segment 17 for the 1408.0 keV ^{152}Eu line.

In events in which energy is deposited in segment 16, the core energy is reduced, e.g. the 1408.0 keV ^{152}Eu line gives rise to a peak at $\approx$ 1360 keV in the core energy spectrum if the full energy was deposited in segment 16. This can be explained by enhanced cross talk effects.

To confirm that these effects were caused by an interruption of the signal line from the detector to the preamplifier, data was taken in which another segment, segment 15, was disconnected at the input to the preamplifier stage. The effects caused by this were analogous to the effects observed due to the disconnection of segment 16. As an example, figure 6.5 shows the segment energy versus core energy histogram for segment 14 with second slope caused by disconnecting segment 15.

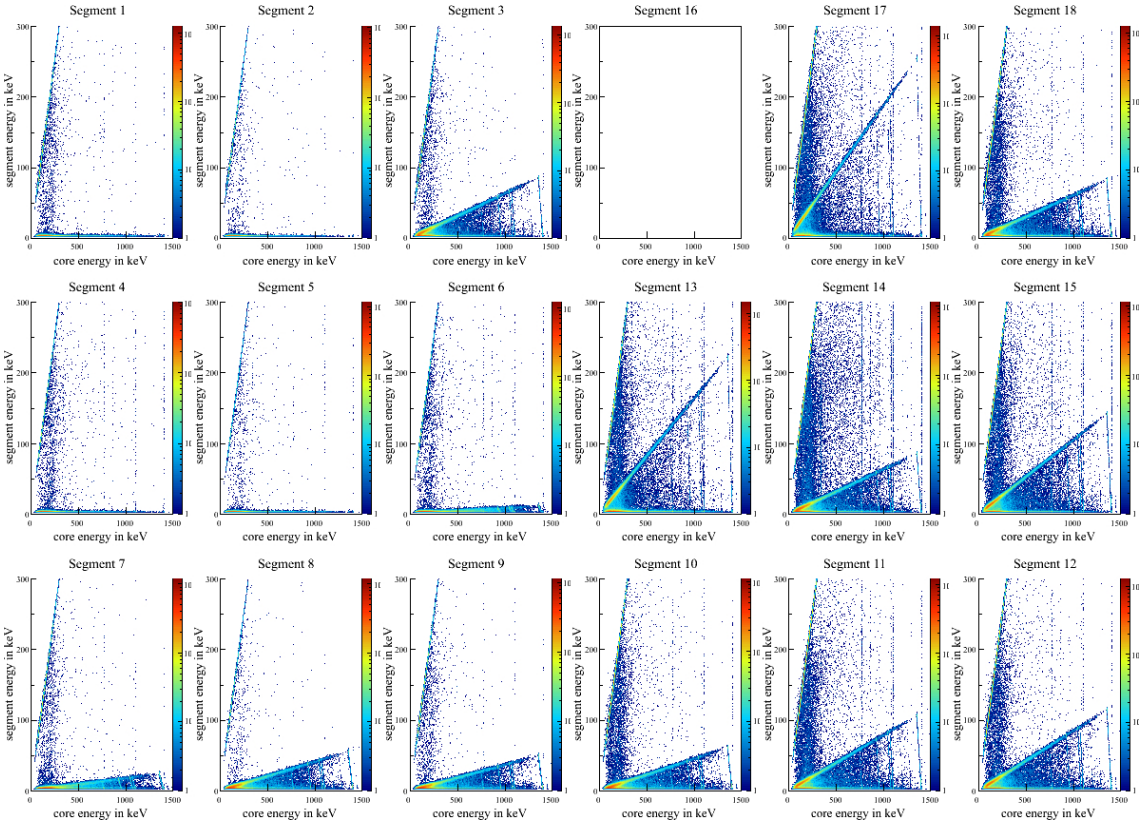

Figure 6.3: Segment energy versus core energy.

6.4 Energy Reconstruction Procedure

The pulse creation in the connected segments follows a well-defined rule. Therefore it should be possible to identify events in which segment 16 was involved, and to reconstruct the energy information of segment 16, as well as correct for the cross talk effects on the core and the segment energies.

6.4.1 Required Parameters

The first step was to quantify the coupling between segment 16 and the other segments. In order to do this, the distributions of segment energy over core energy were examined for the individual segments. These distributions show a continuous background as well as a peak around 1, which corresponds to single segment events with energy deposit in the respective segment. A second peak at lower energies corresponds to single segment events with energy deposit in segment 16. Events with this ratio R_{sci} between segment i energy and core energy lie in the bands mentioned in section 6.3. As an example, figure 6.6 shows the segment energy over core energy distribution for segment 17.

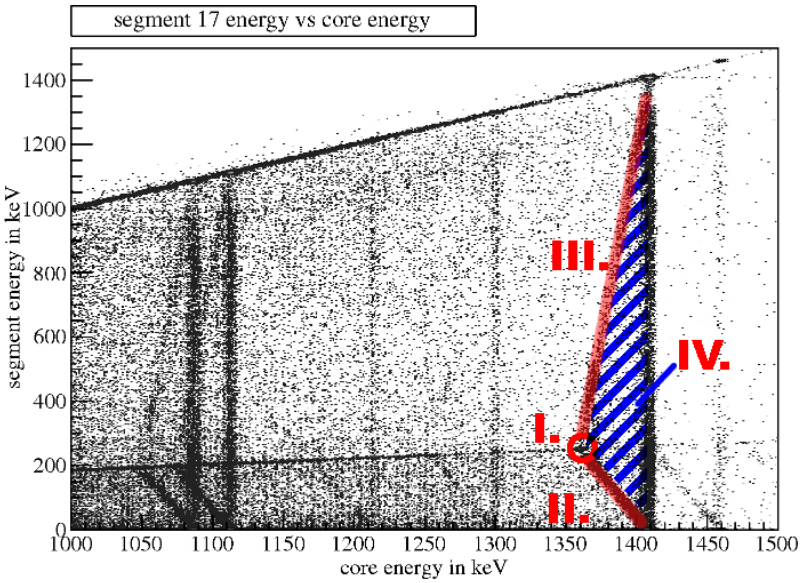

Figure 6.4: Segment energy of segment 17 versus core energy. 'I' marks single-segment events with energy deposit from the ^{152}Eu 1408.0 keV line in segment 16, 'II' are events with partial energy deposit in segment 16 and no energy deposit in segment 17, 'III' events with energy deposit in segment 16 and segment 17, and 'IV' are events with energy deposit in segment 16, the corresponding segment and some other segment.

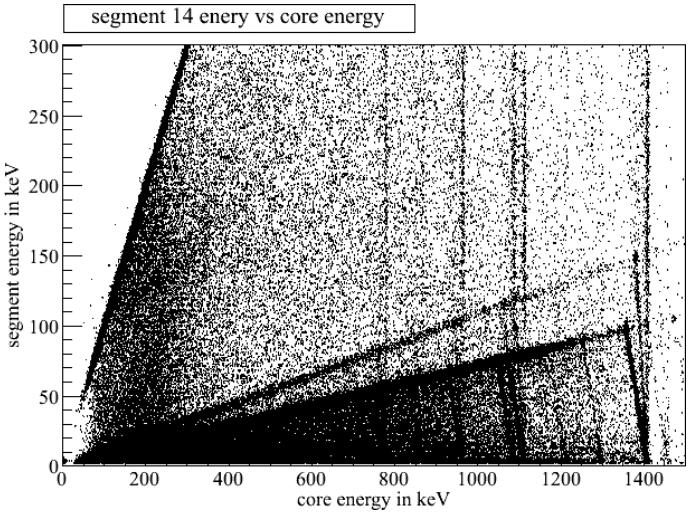

Figure 6.5: Segment 14 energy versus core energy. Segment 15 was disconnected at the input to the preamplifier stage. In addition to the slope caused by the loss of segment 16, a second line with a different slope can be seen.

To determine the position of these second peaks, they were fitted with a Gaussian plus a first order polynomial to describe the background. In some segments, the coupling was too small to be identified, since the induced pulse was too small to be distinguished from the noise peak at the lower edge of the segment over core energy-distribution, which was the case for all values of R_{sci} less than $\approx 1\%$.
The results for the ratios R_{sci} are listed in table 6.2. The sum over all segments is (93.9 $\pm$ 0.9) %. This means that roughly 6% of the charge dissipated during the pulse formation.

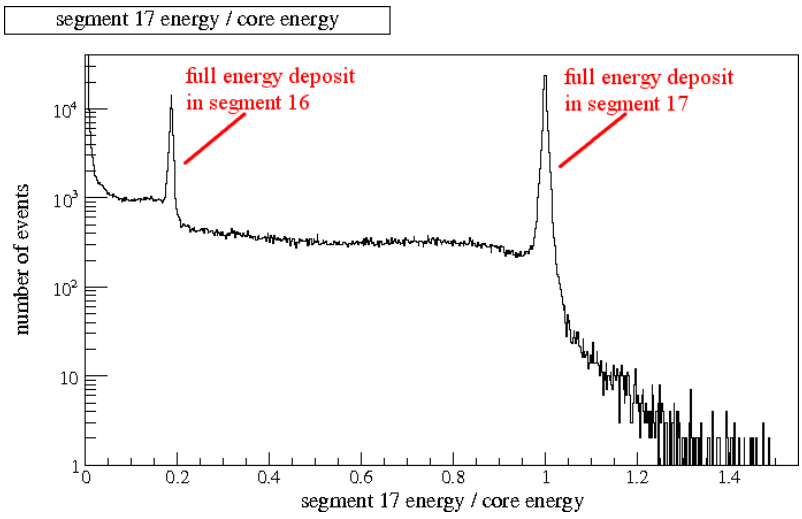

Figure 6.6: Segment 17 energy divided by core energy.

segment	energy fraction (%)
1	$\lesssim 1$
2	$\lesssim 1$
3	6.2 ± 0.3
4	$\lesssim 1$
5	$\lesssim 1$
6	$\lesssim 1$
7	1.7 ± 0.3
8	4.0 ± 0.2
9	3.6 ± 0.3

segment	energy fraction (%)
10	4.5 ± 0.2
11	7.8 ± 0.3
12	8.4 ± 0.3
13	16.3 ± 0.3
14	6.2 ± 0.3
15	10.4 ± 0.3
16	-
17	18.7 ± 0.3
18	6.0 ± 0.3

Table 6.2: Ratio R_{sci} of segment to core energy for events with full energy deposit in segment 16.

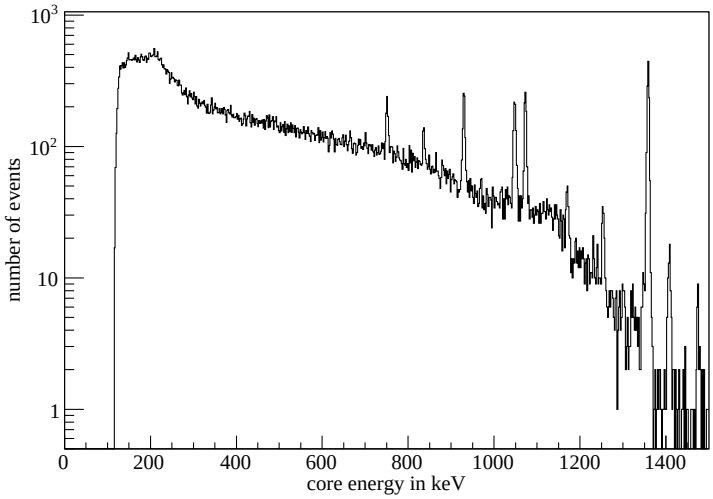

Figure 6.7: Core energy spectrum used to find the core pulse height for single segment events in segment 16.

In addition to these factors, the cross talk shift of the core energy for events with energy deposit in segment 16 has to be taken into account as well. This shift was studied by determining the position of the peaks in a core energy spectrum composed of single segment events in segment 16. These events were selected by requiring that the segment over core energy ratio of both the two segments with the largest fraction of transferred segment 16 energy (i.e. segments 13 and 17) were within 3σ of the values given in table 6.2. The resulting core energy spectrum for those events can be seen in figure 6.7. The peaks in the core energy spectrum were

fitted with a Gaussian plus first order polynomial and compared to the energies of the ^{152}Eu decay. The results are listed in table 6.3. The pulse height of single segment events in segment 16 in the core was found to be $s_{core} = (96.5 \pm 0.2)\%$ of the pulse height that would be seen in the connected segments, independent of the energy.

^{152}Eu line (keV)	Shifted peak (keV)	FWHM (keV)	ratio $s_{core}(\%)$
778.9	751.0 ± 0.2	4.5 ± 0.4	96.4 ± 0.2
964.1	929.8 ± 0.1	4.9 ± 0.3	96.4 ± 0.2
1085.9	1048.0 ± 0.2	6.3 ± 0.5	96.5 ± 0.3
1112.1	1072.9 ± 0.1	4.9 ± 0.2	96.5 ± 0.2
1408.0	1358.7 ± 0.1	4.9 ± 0.2	96.5 ± 0.1

Table 6.3: ^{152}Eu lines and corresponding shifted peaks in the core energy spectrum for single segment events in segment 16.

6.4.2 Energy Reconstruction

For the reconstruction of the energy information from segment 16, the four segments with the largest fraction of transferred energy, designated as $\mathcal{S} = \{$ segments 12, 13, 15, 17 $\}$, were used. The number of four segments was chosen because it was judged to be sufficient to reliably identify events with energy deposit in segment 16, without complicating the algorithm too much.

Only events in which all four segments had an energy larger than 10 keV were taken into consideration as events with possible energy deposit in segment 16. Below 10 keV, the energy seen in those segments could be caused by electronic noise. This requirement leads to an energy threshold for the reconstructed energy spectrum depending on the smallest value of R_{sci} for the segments $\in \mathcal{S}$, that is $E[seg_{16}] > \frac{10keV}{R_{sc-12}} \approx 120\,keV$.

Event Types

For the purpose of identifying events with energy deposit in segment 16, all events were classified as one of five event types:

Type A events: Single segment hit in segment 16;

Type B events: Partial energy deposit in segment 16, no energy deposit in any of the segments $\in \mathcal{S}$;

Type C events: Partial energy deposit in segment 16, and partial energy deposit in one of the segments $\in \mathcal{S}$;

Type D events: No energy deposit in segment 16, i.e. no corrections necessary;

Type E events: All other events, for example events with energy deposit in segment 16 and two segments out of $\mathcal{S}$.

Type A

For type A events, the ratio between core and segment energy should correspond to the ratio given in table 6.2 within 2σ for all segments $\in \mathcal{S}$:

$$|Energy[seg_i] - Energy[core] \cdot R_{sci}| \leq \Delta R_{sci} \cdot s_{core} Energy[seg_i], \tag{6.2}$$

where seg_i are the segments $\in \mathcal{S}$, R_{sci} is the segment-to-core energy ratio for the respective segment given in table 6.2, ΔR_{sci} two times the standard deviation of the fitted peak in the corresponding segment energy over core energy distribution, given in percent, and s_{core} is the shift in core energy determined in section 6.4.1.
If this condition is met for each of the four segments, the event is assumed to be an event with full energy deposit in segment 16. The energy of segment 16 is then

$$Energy[seg_{16}] = \frac{Energy[core]}{s_{core}}. \tag{6.3}$$

Type B

For type B events, the energy should be less than for type A events in all four segments, thus:

$$Energy[seg_i] < Energy[core] \cdot R_{sci} + \Delta R_{sci} \cdot s_{core} Energy[seg_i]. \tag{6.4}$$

The energies of segment 16 calculated from the energies of each segment $\in \mathcal{S}$ should all agree within the uncertainty ΔR_{sci} . The energy deposit in segment 16 is then calculated as the weighted average over the results from the four segments, including

the correction for the core shift:

$$Energy[seg_{16}] = \sum_{seg_i \in \mathcal{S}} \frac{1}{w_i} \cdot \frac{Energy[seg_i]}{R_{sci} \cdot s_{core}}, \tag{6.5}$$

where $w_i = R_{sci} / \sum_{seg_i \in \mathcal{S}} R_{sci}$ are the weighting factors for the individual segments.

Type C

If the energy deposit in three out of the four segments $\in \mathcal{S}$ (a, b, c) satisfies equation 6.4 and the energy deposit in the fourth segment (d) was larger, it can be identified as an event with energy deposit in the corresponding segment and in segment 16. This was assumed to be the case if the energies of segment 16 calculated separately from the energies of the other three segments agreed within the uncertainty ΔR_{sci}. In this case, the event was accepted as an event involving segment 16. The reconstructed energy of segment 16 can be calculated from the measured energies in the core and the segment (d) with the partial energy deposit as

$$Energy[seg_{16}] = \frac{Energy[core] - Energy[seg_d]}{(1 - R_{sci}) + (1 - 1/s_{core})}. \tag{6.6}$$

Correction of the Other Segments

If an event was accepted as an event of one of the types discussed above, the calculated energy for segment 16 was used to correct the energies of core and all the other detector segments.
Since the core energy was decreased if some of the energy deposit took part in segment 16, the corrected core energy was calculated as

$$Energy[core]_{corrected} = Energy[core]_{measured} + Energy[seg_{16}] \cdot (1/s_{core} - 1)\,. \tag{6.7}$$

The corrected segment energies for the connected detector segments were calculated by subtracting the signal induced in them due to energy deposit in segment 16 from the measured segment energy,

$$Energy[seg_i]_{corr} = Energy[seg]_{meas} - Energy[seg_{16}] \cdot (1 - 1/s_{core})\, R_{sci} \cdot s_{core}. \tag{6.8}$$

Restrictions

The conditions used by the algorithm only allow for reconstruction of a part of the events in which energy was deposited in segment 16.

As mentioned above, the requirement that the four segments $\in \mathcal{S}$ should have an energy of at least 10 keV means that any events in which $Energy[seg_{16}] \lesssim 120keV$ could not be reconstructed.

Additionally, events with energy deposit in segment 16 and in two or more out of the four segments $\mathcal{S}$ (type E) were not reconstructed.

6.4.3 Application to Data

The energy reconstruction procedure was applied to the dataset described in 6.2.1. It resulted in an identification of 4.02% of the events in the dataset as events of type A, B and C. Of these, (1.04 ± 0.12)% were of type A, (1.59 ± 0.16)% were of type B and (1.39 ± 0.15)% were of type C.

The ^{152}Eu lines could be resolved in the reconstructed energy spectrum of segment 16. The resolution is FWHM = 4.12 ± 0.15 keV at 1408.0 keV, which is of the same order as the energy resolution of the other segments. The reconstructed energy spectrum of segment 16 can be seen in figure 6.8.

Figure 6.9 shows the core energy spectrum before and after the correction for the energy deposit in segment 16. It is evident that the artificial structures induced by hits in segment 16, which are present in the uncorrected spectrum, are significantly reduced. The resolution that was FWHM = 5.26 ± 0.02 keV at 1408.0 keV before the correction is reduced to FWHM = 5.21 ± 0.02 keV.

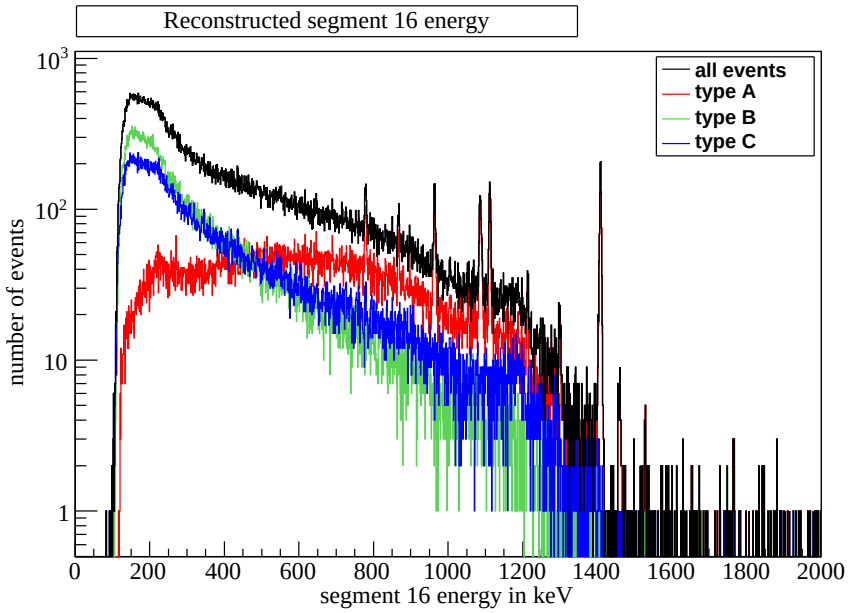

Figure 6.8: Reconstructed energy spectrum of segment 16, for type A, B, C and all events.

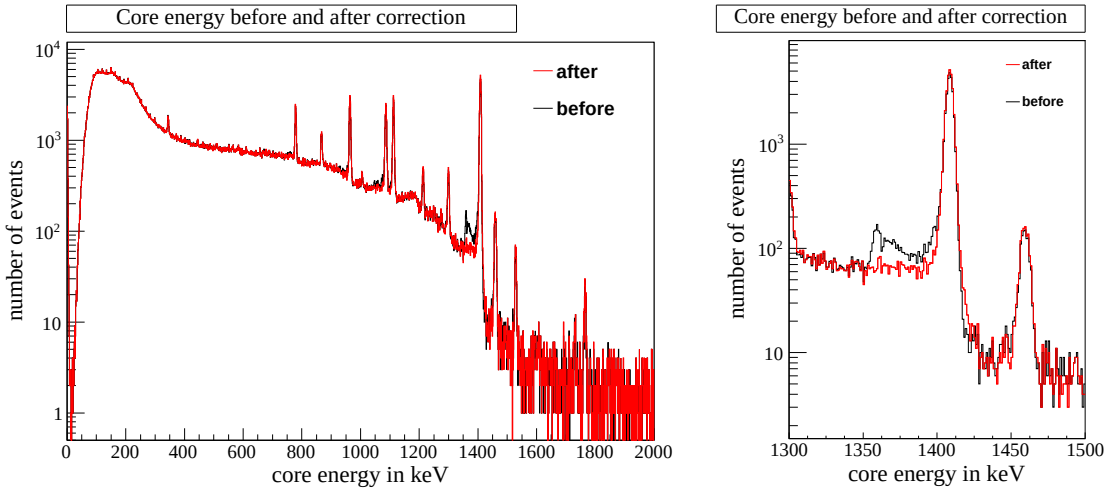

(a) (b)

Figure 6.9: Core energy spectrum before and after the correction for energy deposit in segment 16. In (b) it can be seen how the peak around 1360 keV caused by the shift to lower core energies for events with energy deposit in segment 16 is reduced by the energy correction procedure.

6.5 Comparison with Simulated Data

To investigate the efficiency of the energy reconstruction procedure, the results described in section 6.4.3 were compared to a simulated dataset. This was done for

two reasons:

1. to see how high the probability was for an event to be falsely selected as a segment 16 event;

2. to compare the number of segment 16 events found in the data with the fraction of actual segment 16 events and the number of type A, B, C, D and E events predicted by the simulation.

This gives a limit on the efficiency of the method.

6.5.1 Simulation

The Siegfried III detector and the Gerdalinchen II teststand were simulated in MaGe, a Geant4 [Ago03] framework developed by the Majorana and GERDA collaborations [Cha08].

Figure 6.10 shows the simulated setup. A collimated ^{152}Eu source was aimed at the center of segment 14 (z=203 mm, φ=38°) and its decay was simulated. The simulated dataset contains $\approx$ 5 million events.

The detector resolution as seen in the experimental setup was taken into account. Equation 6.1 was used to obtain the energy resolution which was then used to "smear" the simulation. To do this, the energy of each event in the simulated spectra was multiplied with a random point from within a Gaussian whose standard deviation corresponds to the 1σ resolution at this energy, ,

$$E_{smeared} = E_{dep} + rn \cdot \sigma(E), \tag{6.9}$$

where rn is a random number from a standard Gaussian and $\sigma(E)$ the value calculated from equation 6.1.

The same reconstruction procedure as for the experimental dataset was applied to the simulated events.

6.5.2 Comparison of Measured and Simulated Data

Out of these, only one event was found to meet the requirements for a segment 16 event, i.e. the number of false positives was $\approx 2 \cdot 10^{-5}$ %.

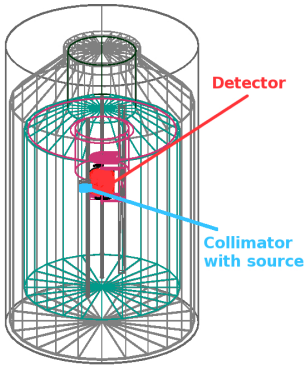

Figure 6.10: Schematic drawing of Siegfried III inside Gerdalinchen II.

The number of events per segment, normalized to the total number of entries, were determined for the experimental data before and after energy reconstruction, and for the simulation. The energy range from 300 keV - 1500 keV was taken into account.

Figure 6.11 shows the normalized fraction of events per segment for the corrected and the uncorrected data and for the simulation. The agreement between the results for the data and the simulation for most segments is good. Slight deviations are visible especially in the segments 13, 14 and 15 that were closest to the source, could be due to the uncertainty on the source position in the data mentioned in section 6.2. The deviations are of the order of 10%.

The fraction of events for the individual event types in the corrected data and the simulation are listed in table 6.4. As explained in section 6.4.2, type E events can not be reconstructed with the presented algorithm. Comparison of the fraction of events in the corrected data and the simulation show that the energy reconstruction algorithm finds $\approx 85\%$ of the type A, B and C events with energy deposit in segment 16.

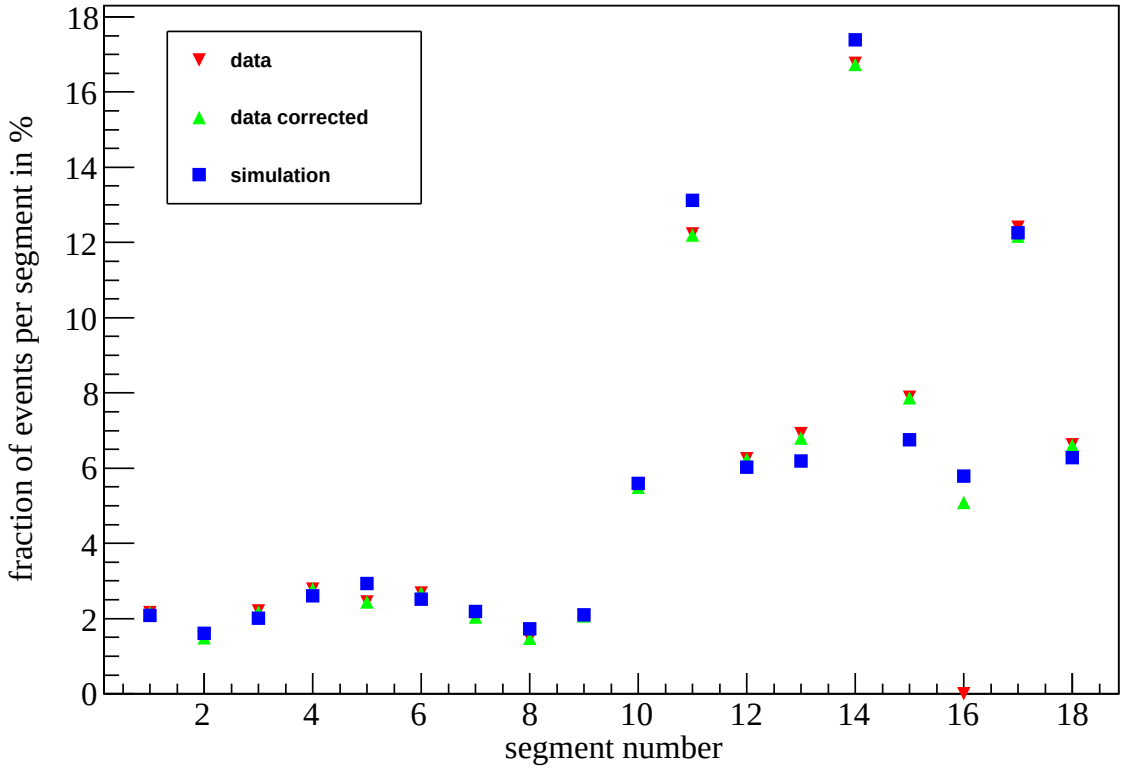

Figure 6.11: Normalized fraction of events per segment for the corrected and the uncorrected data and for the simulation. Statistical uncertainties are included but too small to be visible.

type of event	reconstructed events (%)	simulated events (%)
A	3.1	3.5
B	1.4	1.5
C	1.8	2.3
D	93.7	90.9
E	-	1.8

Table 6.4: Normalized fraction of events per segment for the corrected data and for the simulation for the different event types. Events inside the range 300 keV to 1500 keV were considered.

6.6 Results

The discussion in the section above shows that if one segment of the detector is disconnected between detector and preamplifier stage, its energy information can be recovered.

The reconstruction procedure described performs well in finding events in which energy was deposited in the disconnected segment, while the number of false positives selected by the criteria described above is negligible.

The energy resolution in the reconstructed energy spectrum is comparable to the normal resolution of other segments, it can thus provide valuable information in a long-term experiment where one of the segments might lose contact during operation, making an immediate repair unnecessary.

In the future, the algorithm could be expanded to use more than four segments in the event identification. An analysis of the type E events could be implemented in the reconstruction method to increase the identification rate of events affected by hits in segment 16.

7 Siegfried III Energy Resolution

Since the GERDA experiment requires an extremely low background level, the amount of radioactively impure material has to be limited as much as possible, especially close to the detectors. One way to reduce the amount of material close to the detector would be a partial instead of a full metallization of the segment contacts.

This chapter describes an investigation to address the question whether such a partial metallization has a significant effect on the performance of the detector. A special prototype detector was scanned to see if a partial metallization has a measurable effect on the energy resolution. Different fitting methods are applied to the data to investigate the systematics of the fit procedure used to determine the resolution.

7.1 Experimental Setup

As mentioned in section 5.3.2, the prototype detector Siegfried III was produced with a mixed metallization scheme: the segments in the top layer of the detector (segments 1, 2, 3, 16, 17 and 18) are only metallized in the segment centers, while the outer surfaces of the segments in the middle and bottom layer are fully metallized. Since the partial metallization can change the shape of the electric field, it could be expected to have an effect on the charge collection inefficiency term in equation 5.10 for the resolution.

To address the question whether there is an effect of the missing metallization on the energy resolution, data was taken with Siegfried III inside the liquid nitrogen teststand Gerdalinchen II (see 5.4.1). A 40 kBq ^{152}Eu source was placed into the tungsten collimator inside the teststand, in the experimental setup described in the previous chapter (see section 6.2).

7.2 Datasets

The entire length of the detector was scanned in 4 mm steps in z, with the source aimed at the center of the segments 11, 14, 17, respectively, in φ. The data taking took place during several weeks, from 14.01.2010 to 23.03.2010. The data samples for the different z-positions contain approximately $4 \cdot 10^6$ events each. For each event, energy and time information of the core and the 18 segments were recorded.

The step size of 4 mm in z-direction was chosen based on the spot size of the collimated beam. From purely geometrical calculations, the spot size of the collimator can be found to be ≈ 3.5 mm. The actual spot size can be found by examining the count rate distribution of the measurements:

The count rate was calculated from the measuring time and the number of events under the 344.3 keV end 1408.0 keV peaks respectively. Assuming no charge trapping occurs at the segment boundaries, the shape of the count rate distribution can be described by the convolution of a box function representing the borders of the segments, and a Gaussian to account for the spot size of the beam.

Figure 7.1 shows the count rate distributions of the 344.3 keV and 1408.0 keV lines for the segments 11, 14 and 17 as a function of the height z for all events in

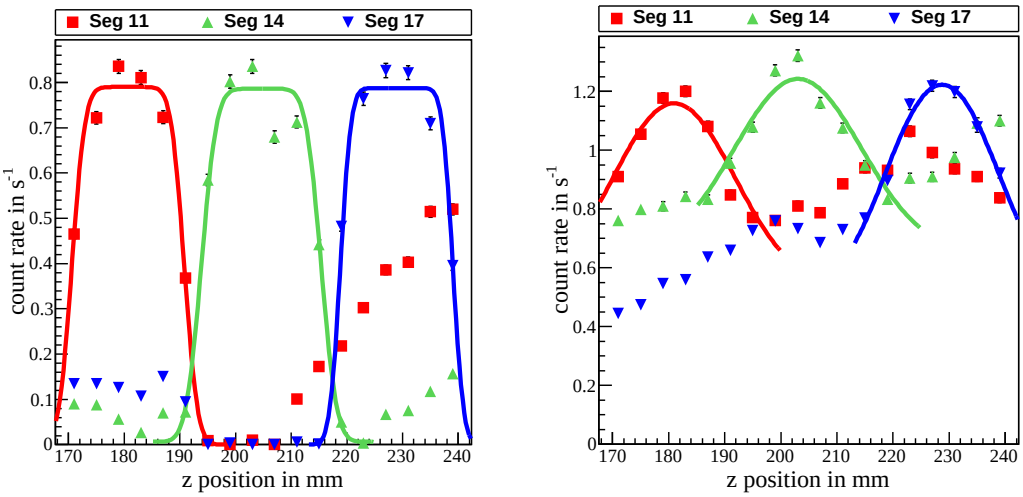

Figure 7.1: Count rate in the segments 11, 14 and 17 as a function of the source position in z-direction, for (a) the 344.3 keV and (b) the 1408.0 keV ^{152}Eu lines. The fit with a step function folded with a Gaussian for the individual segments is also shown.

the datasets, without applying any cuts. Also visible in figure 7.1(a) is the increase of the count rate in segment 11 when the source is moved towards the top of the detector, even though segment 11 is located in the bottom layer of the detector. This effect is caused by the geometry of the source holder. Since there is no tungsten underneath the source, there is a small angle through which photons can escape downwards. If the source is positioned near the top of the detector, the downwards directed photons can deposit energy in the bottom layer. Therefore, the count rate distributions for the segments were only fitted within a range covering the physical height of the segment plus 10 mm. A similar pattern can be seen in the count rate of segment 14.

The box function convoluted with a Gaussian was fitted to the data, with the height of the box, the z-position of the lower segment boundaries and the width of the Gaussian as free parameters. The results are displayed in figure 7.1, the widths of the Gaussian functions determined by the fit are given in table 7.1. For the 344.3 keV ^{152}Eu line, the size of the beam spot is close to the one calculated purely from the collimator geometry, while for the 1408.0 keV line the source is significantly less collimated.

Segment	FWHM at 344.3 keV [mm]	FWHM at 1408.0 keV [mm]
11	4.4 ± 0.2	13.5 ± 0.6
14	5.1 ± 0.1	13.9 ± 0.6
17	3.8 ± 0.2	13.9 ± 0.6

Table 7.1: Fitted width of the Gaussian describing the collimator spot size at 344.3 and 1408.0 keV for the segments 11, 14, and 17.

7.2.1 Event Selection

From the datasets described above, events with energy deposit in only one segment (*single segment events*) were selected. The condition for a single segment event is that the energy deposit in all segments except one is less than 20 keV. A 20 keV threshold was chosen to reject signals due to low-amplitude noise, however it will also lead to a less strict background rejection than a lower threshold would.

During data taking, segment 16 had no contact, as discussed in chapter 6. As a consequence, an event in which the energy deposit in all segments except one is less than 20 keV is not necessarily a single segment event. It might also be an event in which a fraction of the energy was deposited in segment 16. Therefore,

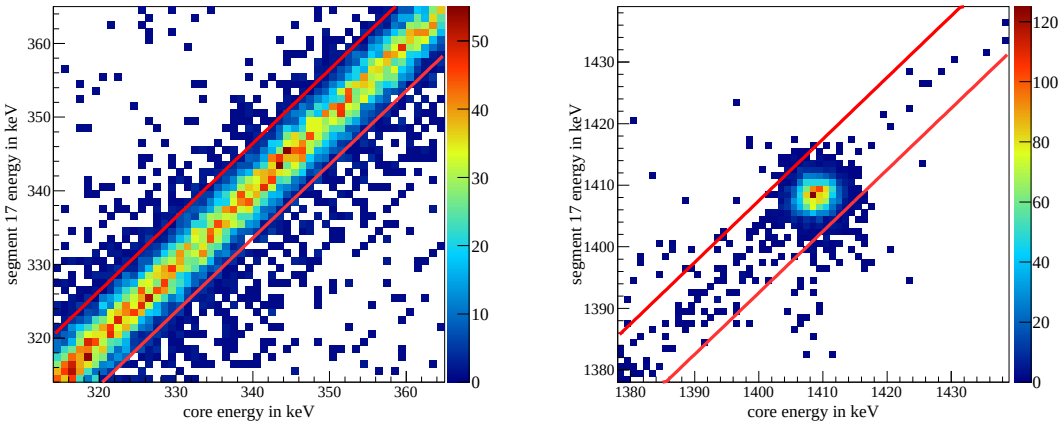

(a) (b)

Figure 7.2: Event selection: All single segment events in segment 17 are shown for the dataset with z=203 mm, (a) around 344.3 keV and (b) around 1408.0 keV. The two red lines mark the $\pm 3\sigma_{core}$ range.

an additional cut had to be introduced in the event selection procedure: For each dataset, the core resolution as a function of energy was fitted as described in section 6.2.1. Only events in which the segment energy was within 3σ of the core energy were selected. The range this corresponds to is illustrated in figure 7.2.

7.3 Analysis

The 121.8 keV line of ^{152}Eu had a peak to background ratio much smaller than one. Therefore, two other ^{152}Eu lines with better signal to background ratios were studied instead, the 344.3 keV line with a peak-to-background ratio $\frac{peak}{BG} \approx 1$, and the 1408.0 keV line with $\frac{peak}{BG} \geq 40$. As an example for the shape of the energy spectra, figure 7.3 shows the core energy spectrum for the single segment events selected from the dataset taken at z=203 mm.

For each single segment dataset, the core resolution and the resolution of the segment closest to the source, the *segment of interest*, were determined. Table 7.2 shows the z-positions at which data was taken, the respective segments of interest and the peak to background ratios at 344.3 keV and 1408.0 keV.

Different fit windows and functions were used and compared to study the systematics of the fitting procedure.

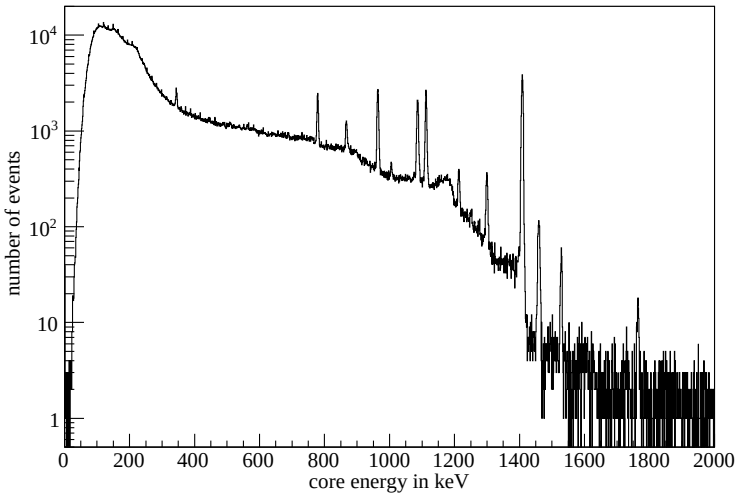

Figure 7.3: Core energy spectrum for the selected events from the dataset taken at z=203 mm.

segment	z in mm	$\left(\frac{peak}{BG}\right)_{core,344}$	$\left(\frac{peak}{BG}\right)_{core,1408}$	$\left(\frac{peak}{BG}\right)_{seg,344}$	$\left(\frac{peak}{BG}\right)_{seg,1408}$
11	171	0.13 ± 0.01	81.36 ± 5.39	0.58 ± 0.02	53.30 ± 6.66
	175	0.19 ± 0.01	66.20 ± 3.90	0.90 ± 0.02	68.13 ± 9.05
	179	0.20 ± 0.01	61.23 ± 3.42	1.04 ± 0.03	58.42 ± 6.90
	183	0.19 ± 0.01	60.14 ± 3.31	1.04 ± 0.03	82.28 ± 11.43
	187	0.19 ± 0.01	48.71 ± 2.44	0.93 ± 0.03	54.29 ± 6.46
	191	0.11 ± 0.01	58.33 ± 3.21	0.52 ± 0.02	57.42 ± 7.97
14	195	0.14 ± 0.01	59.42 ± 3.25	0.91 ± 0.03	47.39 ± 5.31
	199	0.17 ± 0.02	60.54 ± 3.31	1.26 ± 0.04	66.46 ± 8.13
	203	0.18 ± 0.01	40.30 ± 1.82	1.23 ± 0.03	65.79 ± 7.87
	207	0.18 ± 0.02	76.94 ± 4.72	1.33 ± 0.04	55.35 ± 6.30
	211	0.17 ± 0.01	64.47 ± 3.48	1.09 ± 0.03	67.04 ± 8.31
	215	0.13 ± 0.01	63.27 ± 3.39	0.81 ± 0.03	59.74 ± 7.48
17	219	0.17 ± 0.01	60.96 ± 3.18	0.56 ± 0.02	44.55 ± 4.97
	223	0.24 ± 0.01	71.95 ± 4.17	1.00 ± 0.03	69.58 ± 9.28
	227	0.26 ± 0.01	78.53 ± 4.75	0.99 ± 0.03	60.48 ± 7.34
	231	0.25 ± 0.01	69.41 ± 3.93	1.00 ± 0.03	63.87 ± 8.03
	235	0.28 ± 0.02	77.51 ± 4.65	0.86 ± 0.02	62.11 ± 8.11
	239	0.22 ± 0.01	75.18 ± 4.52	0.50 ± 0.02	60.50 ± 8.41

Table 7.2: Segment of interest, corresponding z-positions and peak-to-background ratios for 344.3 keV and 1408.0 keV in the core and segment energy spectra.

7.3.1 Comparison of Fitting Methods

A common procedure for fitting the peaks of a gamma spectrum is to use a Gaussian on top of a first order polynomial. This technique was compared with similar approaches trying to improve the background model, to study the systematics in determining the energy resolution of the datasets. To compare the goodness of fit, the reduced chi-squared statistics, i.e. the chi-squared divided by the number of degrees of freedom, were calculated:

$$\chi^2_{\text{red}} = \frac{\chi^2}{\text{NDF}} = \frac{1}{\text{NDF}} \sum_{i=1}^{n} \frac{(O_i - E_i)^2}{E_i}, \tag{7.1}$$

where n is the number of histogram bins being fitted, O_i is the observed frequency (number of counts) in bin i, E_i is the frequency in bin i expected based on the integral of fitted function over the bin width, and NDF the number of degrees of freedom (i.e. the number of histogram bins being fitted, reduced by the number of parameters of the fit function) [Bra03]. Since the fits were performed with different NDFs, the areas in the tails of the probability distributions given by the χ^2 and NDF values, the so-called *p-values* $p(\chi^2/_{\text{NDF}})$, were used to compare the goodness of fit.

Gaussian Plus First Order Polynomial Background

As a first step, the datasets were fitted with a Gaussian plus a first order polynomial

$$\underbrace{p_0 + p_1 x}_{\substack{first\ order \\ polynomial}} + \underbrace{a \cdot \exp\left(-\frac{(x-\mu)^2}{2\sigma^2}\right)}_{gaussian\ function}, \tag{7.2}$$

where the free parameters were the y-intercept and the slope of the first order polynomial, p_0 and p_1, the constant a, the center of the gauss peak μ and the standard deviation σ, which is related to the full width at half maximum (FWHM) through the relation

$$\text{FWHM} = 2\sqrt{2\ln 2} \cdot \sigma \approx 2.35 \cdot \sigma. \tag{7.3}$$

The best fit of the free parameters varies with the energy range which was fitted and thus with the fraction of background that was included in the fit range. Therefore, to ensure that the area of the fitted Gaussian was approximately the same for all datasets, the fitting was done in two steps: First, equation 7.2 was fitted to the

data within a fixed fit window of ± 15 keV, centered around 344.3 keV and 1408.0 keV respectively. The results from the first fit were then used to set a new range of width $\pm n \cdot \sigma$ around the center of the peak, where n was varied, and fit the spectrum again. An example for such a fit can be seen in figure 7.6(a).

The $p(\chi^2/_{\mathrm{NDF}})$ values were calculated and compared for different n. The average FWHM and $p(\chi^2/_{\mathrm{NDF}})$ for core and segment are listed in table 7.3 and 7.4, the single values from all fits are listed in tables A.1-A.6. Figure 7.4 shows the FWHM result for the fit within a fit range of $5 \cdot \sigma$.

The charge collection inefficiency contributes to the energy resolution. If an effect due to reduced charge collection efficiency near the segment boundaries is present, it should have an impact on the shape of the peak. In this case, $p(\chi^2/_{\mathrm{NDF}})$ for the fits to the segment energy spectra 344.3 keV ^{152}Eu line is expected to be smaller for data points where the source was positioned near the segment borders than for source positions near the segment center. The fits to the 1408.0 keV ^{152}Eu line should not

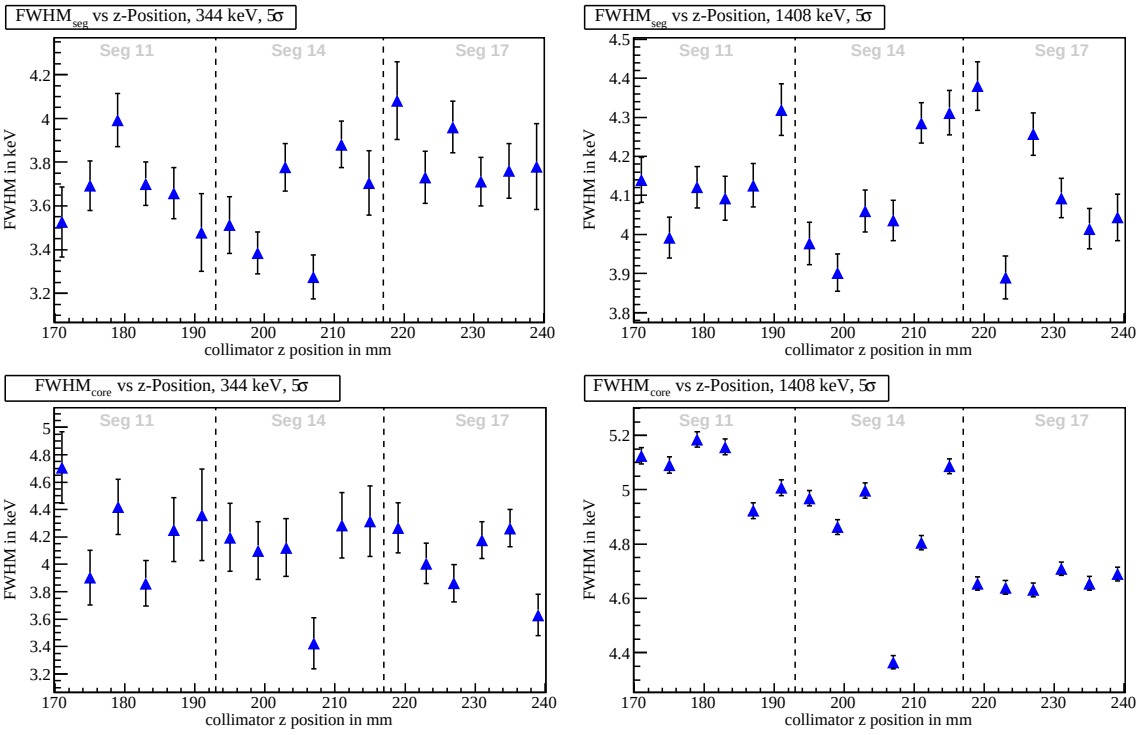

Figure 7.4: Resulting segment (top) and core (bottom) FWHM at 344.3 keV (left) and 1408.0 keV(right). The values are those from the fit with Gaussian with first order polynomial background within a fit range of $5 \cdot \sigma$, with statistical errors. Please note the different ranges of the y-axes.

show this behavior to the same extent, since this energy beam was less collimated and effects of the segment boundary would be washed out. For the segment energy spectra, a more pronounced effect than for the core is expected due to the weighting field in the affected volume.

This behavior is not fully confirmed by the data. While the $p(\chi^2/_{\mathrm{NDF}})$-values for the fully metallized segment agree with that expection for the segment fits, the same can not be said for the partially metallized segment. Further analysis of this effect

energy (keV)	$n \cdot \sigma$	FWHM_{core}	FWHM_{11}	FWHM_{14}	FWHM_{17}
344.3	3.5	4.10 ±0.35	3.65 ±0.14	3.59 ±0.25	3.85 ±0.09
	4.0	4.13 ±0.31	3.65 ±0.16	3.61 ±0.22	3.83 ±0.12
	4.5	4.14 ±0.30	3.68 ±0.14	3.58 ±0.21	3.83 ±0.15
	5.0	4.12 ±0.29	3.68 ±0.16	3.59 ±0.22	3.84 ±0.14
	6.0	4.13 ±0.32	3.70 ±0.13	3.59 ±0.21	3.84 ±0.14
	7.0	4.15 ±0.34	3.71 ±0.12	3.60 ±0.21	3.86 ±0.14
1408.0	3.5	4.88 ±0.23	4.11 ±0.07	4.06 ±0.15	4.09 ±0.14
	4.0	4.87 ±0.22	4.11 ±0.10	4.07 ±0.16	4.10 ±0.15
	4.5	4.87 ±0.22	4.12 ±0.10	4.09 ±0.15	4.10 ±0.16
	5.0	4.86 ±0.22	4.13 ±0.10	4.10 ±0.15	4.11 ±0.16
	6.0	4.86 ±0.22	4.14 ±0.09	4.11 ±0.15	4.12 ±0.16
	7.0	4.87 ±0.22	4.14 ±0.09	4.11 ±0.15	4.13 ±0.17

Table 7.3: Average FWHM for core and segments of interest, fitted using a Gaussian plus first order polynomial background.

energy (keV)	$n \cdot \sigma$	$p(\chi^2/_{\mathrm{NDF}})_{core}$	$p(\chi^2/_{\mathrm{NDF}})_{11}$	$p(\chi^2/_{\mathrm{NDF}})_{14}$	$p(\chi^2/_{\mathrm{NDF}})_{17}$
344.3	3.5	0.95 *pm* 0.06	0.79 ± 0.29	0.81 ± 0.25	0.58 ± 0.35
	4.0	0.94 *pm* 0.07	0.83 ± 0.18	0.78 ± 0.29	0.57 ± 0.36
	4.5	0.93 *pm* 0.09	0.83 ± 0.15	0.79 ± 0.26	0.57 ± 0.35
	5.0	0.92 *pm* 0.11	0.84 ± 0.14	0.78 ± 0.25	0.59 ± 0.33
	6.0	0.92 *pm* 0.12	0.86 ± 0.13	0.77 ± 0.29	0.65 ± 0.32
	7.0	0.94 *pm* 0.13	0.87 ± 0.14	0.76 ± 0.26	0.74 ± 0.31
1408.0	3.5	0.97 *pm* 0.05	0.82 ± 0.11	0.54 ± 0.32	0.82 ± 0.23
	4.0	0.97 *pm* 0.06	0.82 ± 0.16	0.52 ± 0.31	0.79 ± 0.23
	4.5	0.99 *pm* 0.03	0.86 ± 0.16	0.59 ± 0.34	0.73 ± 0.29
	5.0	0.99 *pm* 0.02	0.85 ± 0.21	0.55 ± 0.34	0.77 ± 0.21
	6.0	1.00 *pm* 0.01	0.82 ± 0.26	0.70 ± 0.30	0.76 ± 0.23
	7.0	1.00 *pm* 0.00	0.78 ± 0.27	0.65 ± 0.30	0.84 ± 0.17

Table 7.4: Average $p(\chi^2/_{\mathrm{NDF}})$ for the fit with a Gaussian plus first order polynomial, with statistical errors.

are beyond the scope of this thesis. As an example for the $p(\chi^2/_{\mathrm{NDF}})$-distribution over z, figure 7.5 shows $p(\chi^2/_{\mathrm{NDF}})_{segment}$ and $p(\chi^2/_{\mathrm{NDF}})_{core}$ for the fit with Gaussian with first order polynomial background within a fit range of $5 \cdot \sigma$.

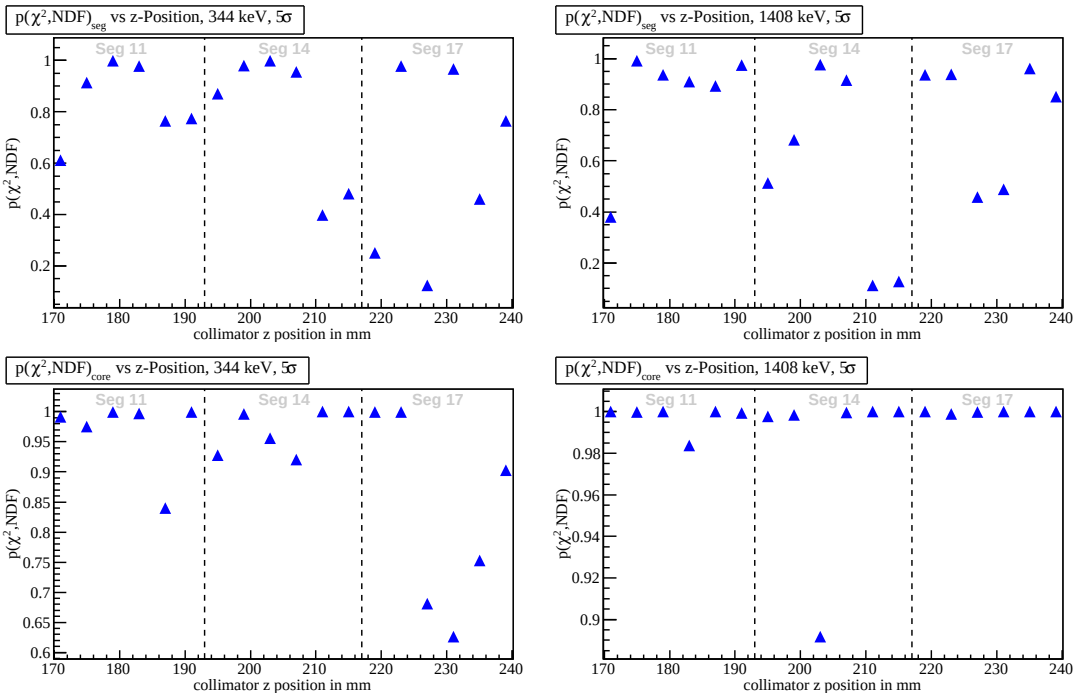

Figure 7.5: $p(\chi^2/_{\mathrm{NDF}})_{segment}$ (top) and $p(\chi^2/_{\mathrm{NDF}})_{core}$ (bottom) from the fit with Gaussian with first order polynomial background within a fit range of $5 \cdot \sigma$, for 344.3 keV (left) and 1408.0 keV(right). Please note the different ranges of the y-axes.

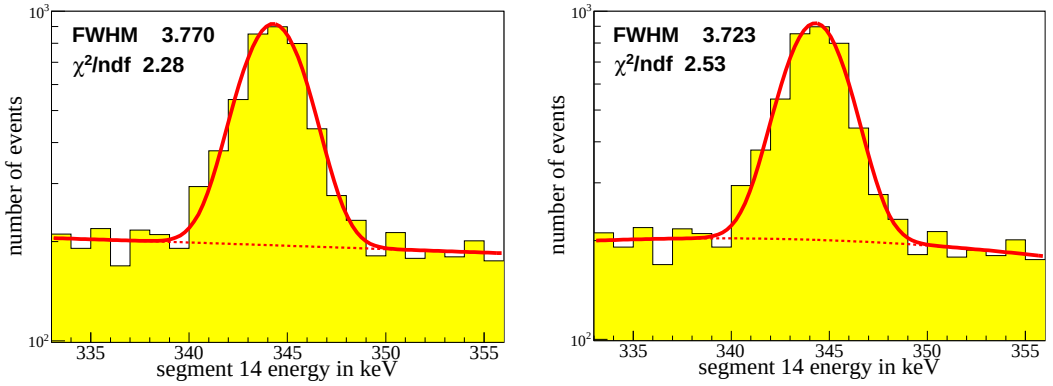

(a) (b)

Figure 7.6: Gaussian with (a) first order polynomial and (b) cubic background, fitted to the energy of segment 14 around the 344.3 keV ^{152}Eu line (z=203 mm). The thick line is the total fit function, the dotted line indicates the fitted background.

Gaussian Plus Cubic Background

An increase in the number of parameters can give an improvement in the description of the background. However, the question remains whether this improvement is large enough to justify the accompanying loss in degrees of freedom. To study this, the datasets were also fitted with a gauss-function plus a cubic background

$$p_0 + p_1 x + p_2 x^2 + p_3 x^3 + \; a \cdot \exp\left(-\frac{(x-\mu)^2}{2\sigma^2}\right), \tag{7.4}$$

with p_0, p_1, p_2, p_3, a, μ and σ as free parameters.

As for the first order polynomial background, the first step was to fit the data within a fit window of ± 15 keV, centered around 344.3 keV and 1408.0 keV respectively. Subsequently a second fit with equation 7.4 was performed inside a new fit range of width $\pm n \cdot \sigma$ around the center of the peaks. An example for such a fit can be seen in figure 7.6(b). The average FWHM and $p(\chi^2/_{\mathrm{NDF}})$ for core and segment are listed in table 7.5 and 7.6, the single values from all fits are listed in tables A.7-A.12. Figure 7.7 shows the result for the fit within a fit range of $5 \cdot \sigma$.

No significant improvement in the description of the data was found that would justify the introduction of two extra parameters for the background. Therefore, only methods for fitting with Gaussian plus first order polynomial background were investigated further.

energy (keV)	$n \cdot \sigma$	FWHM_{core}	FWHM_{11}	FWHM_{14}	FWHM_{17}
344.3	3.5	4.26 ± 0.78	3.74 ± 0.15	3.52 ± 0.35	3.82 ± 0.09
	4.0	4.13 ± 0.44	3.68 ± 0.19	3.55 ± 0.28	3.91 ± 0.14
	4.5	4.08 ± 0.39	3.60 ± 0.12	3.64 ± 0.30	3.88 ± 0.16
	5.0	4.17 ± 0.40	3.63 ± 0.17	3.56 ± 0.25	3.88 ± 0.13
	6.0	4.11 ± 0.32	3.64 ± 0.20	3.59 ± 0.24	3.81 ± 0.13
	7.0	4.10 ± 0.30	3.66 ± 0.16	3.58 ± 0.20	3.79 ± 0.14
1408.0	3.5	4.88 ± 0.23	4.11 ± 0.07	4.06 ± 0.15	4.09 ± 0.14
	4.0	4.87 ± 0.22	4.11 ± 0.10	4.07 ± 0.16	4.10 ± 0.15
	4.5	4.87 ± 0.22	4.09 ± 0.05	4.09 ± 0.15	4.10 ± 0.16
	5.0	4.86 ± 0.22	4.13 ± 0.10	4.10 ± 0.15	4.11 ± 0.16
	6.0	4.86 ± 0.22	4.13 ± 0.10	4.11 ± 0.15	4.11 ± 0.14
	7.0	4.87 ± 0.23	4.14 ± 0.09	4.11 ± 0.15	4.13 ± 0.17

Table 7.5: Average FWHM for core and segments of interest, fitted using a Gaussian plus cubic background.

energy (keV)	$n \cdot \sigma$	$p(\chi^2/_{\mathrm{NDF}})_{core}$	$p(\chi^2/_{\mathrm{NDF}})_{11}$	$p(\chi^2/_{\mathrm{NDF}})_{14}$	$p(\chi^2/_{\mathrm{NDF}})_{17}$
344.3	3.5	0.98 *pm* 0.02	0.86 ± 0.23	0.87 ± 0.19	0.71 ± 0.29
	4.0	0.96 *pm* 0.05	0.88 ± 0.14	0.86 ± 0.19	0.67 ± 0.30
	4.5	0.95 *pm* 0.08	0.88 ± 0.10	0.78 ± 0.30	0.66 ± 0.28
	5.0	0.94 *pm* 0.10	0.89 ± 0.13	0.83 ± 0.22	0.67 ± 0.27
	6.0	0.94 *pm* 0.09	0.88 ± 0.08	0.80 ± 0.26	0.70 ± 0.30
	7.0	0.93 *pm* 0.12	0.87 ± 0.12	0.81 ± 0.23	0.77 ± 0.30
1408.0	3.5	0.99 *pm* 0.03	0.91 ± 0.06	0.67 ± 0.31	0.89 ± 0.16
	4.0	0.99 *pm* 0.04	0.90 ± 0.11	0.65 ± 0.28	0.87 ± 0.16
	4.5	1.00 *pm* 0.01	0.84 ± 0.19	0.69 ± 0.31	0.81 ± 0.24
	5.0	1.00 *pm* 0.01	0.90 ± 0.16	0.65 ± 0.32	0.85 ± 0.16
	6.0	1.00 *pm* 0.01	0.84 ± 0.22	0.77 ± 0.29	0.82 ± 0.17
	7.0	1.00 *pm* 0.01	0.83 ± 0.24	0.73 ± 0.30	0.89 ± 0.13

Table 7.6: Average $p(\chi^2/_{\mathrm{NDF}})$ for the fit with a Gaussian plus cubic background.

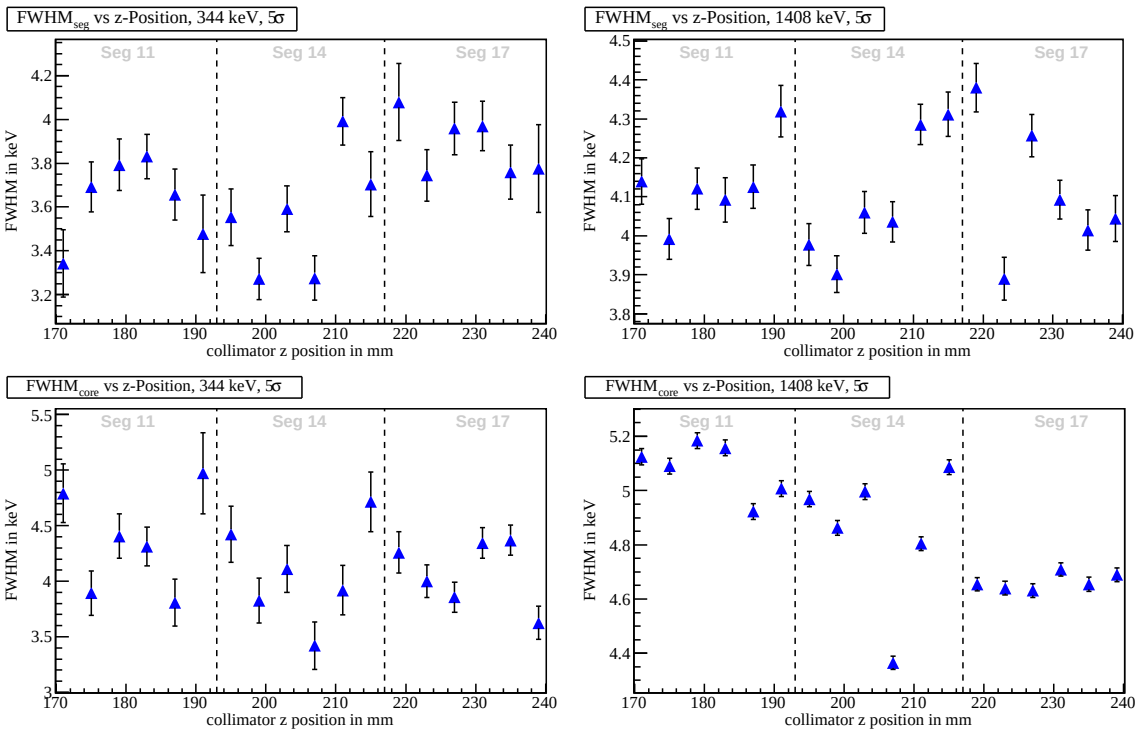

Figure 7.7: Resulting segment (top) and core (bottom) FWHM from the fit with Gaussian with cubic background within a fit range of $5 \cdot \sigma$, with statistical errors. Please note the different ranges of the y-axes.

One-Sided Gaussian

The background contributions on either sides of the peak can differ. To study the influence of the background on the result, two sets of gauss-function plus a straight line were fitted separately to the left-hand side and the right-hand side of the peak.

First the data were fitted with a Gaussian plus first order polynomial within a fit window of ± 15 keV, centered around 344.3 keV and 1408.0 keV respectively. The results from this fit were used to chose a new fit range of width $\pm n \cdot \sigma$ around the center of the peaks. Two one-sided Gaussians plus first order polynomials (see equation 7.2) were fitted to the data within this range, with p_0, p_1, a, μ and σ as free parameters: one from the lower edge of the fit window to the mean value from the first fit, the other from the mean to the right edge of the window. An example for such a fit can be seen in figure 7.8. Figure 7.9 shows the result for the fit within a fit range of $5 \cdot \sigma$, the average FWHM and $p(\chi^2/_{\mathrm{NDF}})$ for core and segment are listed in table 7.8 and 7.9.

For segments with a high charge collection inefficiency, larger deviations from Gaussian shape could be expected on the low energy side. If the partial metallization increases the charge collection inefficiency significantly, $p(\chi^2/_{\mathrm{NDF}})$ for the left-sided fit is expected to be smaller than for the right-sided fit. Table 7.7 lists the percent-

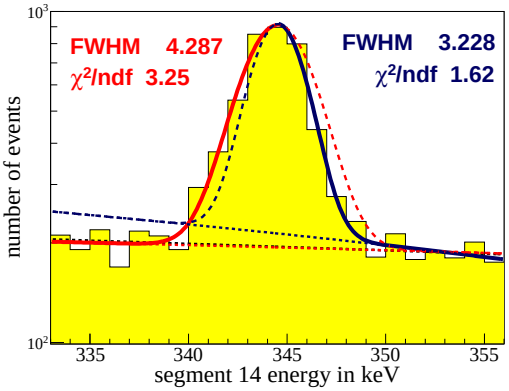

Figure 7.8: Two one-sided Gaussians plus first order polynomials fitted to the energy of segment 14 around the 344.3 keV ^{152}Eu line (dataset taken at z=203 mm). The thick lines are the fits to the left and right side of the peak inside, the dashed lines their continuation outside the fit window. The dotted lines indicate the respective backgrounds.

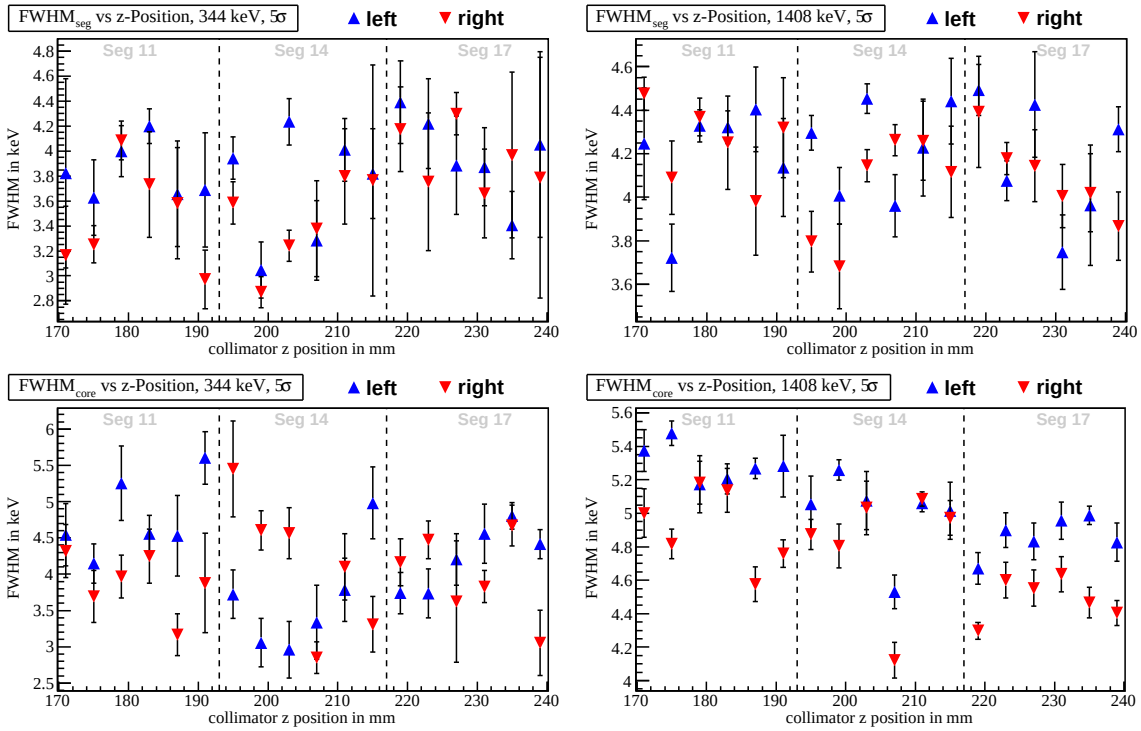

Figure 7.9: Resulting segment (top) and core (bottom) FWHM from the fit with two one-sided Gaussians with first order polynomial backgrounds within a fit range of $5 \cdot \sigma$, with statistical errors. Please note the different ranges of the y-axes.

age of the data points fitted with one-sided Gaussians for which $p(\chi^2/\mathrm{NDF})_{left}$ is larger than $p(\chi^2/\mathrm{NDF})_{right}$. The percentage of fitted data points with $p(\chi^2/\mathrm{NDF})_{left} > p(\chi^2/\mathrm{NDF})_{right}$ for the 1408.0 keV peak in the core energy spectrum is noticeably lower than for the segments or for the 344.3 keV line. The reason for this is not clear. No effect of the partial metallization can be found within the statistical uncertainties.

Energy in keV	CL_{core}	CL_{seg11}	CL_{seg14}	CL_{seg17}
344.3	30.6 ± 5.3	36.1 ± 10.0	41.7 ± 10.8	61.1 ± 13.0
1408.0	13.2 ± 3.5	58.3 ± 12.7	50.0 ± 11.8	50.0 ± 11.8

Table 7.7: Percentage of fitted data points CL_i for which $p(\chi^2/\mathrm{NDF})_{left} > p(\chi^2/\mathrm{NDF})_{right}$, for core and segments 11, 14 and 17.

To study the influence of the background on the outcome of the fit, the fitted FWHM for the left- and right-hand side of the peaks were compared. Within the statistical uncertainties, no difference between the partially metallized segment 17

and the other segments can be found.

Figure 7.10 shows the distribution of the deviations between right-sided and left-sided fit for the core and the segment fits.

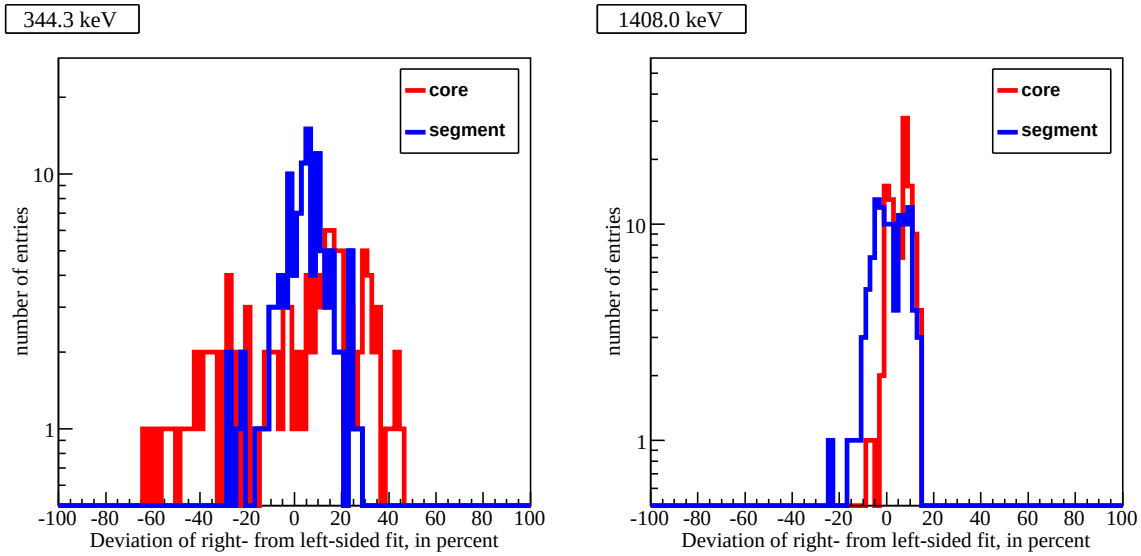

Figure 7.10: Deviations of the right-sided from the left-sided fit, for core and segments.

energy (keV)	$n \cdot \sigma$	FWHM$_{core,L}$	FWHM$_{core,R}$	FWHM$_{11,L}$	FWHM$_{11,R}$
344.3	3.5	3.99 ± 0.70	3.85 ± 0.62	3.69 ± 0.44	3.47 ± 0.26
	4.0	3.99 ± 0.64	3.88 ± 0.61	3.71 ± 0.35	3.53 ± 0.41
	4.5	4.07 ± 0.63	3.96 ± 0.71	3.77 ± 0.28	3.52 ± 0.41
	5.0	4.22 ± 0.71	4.00 ± 0.64	3.83 ± 0.21	3.47 ± 0.38
	6.0	4.23 ± 0.55	3.96 ± 0.68	3.82 ± 0.27	3.48 ± 0.47
	7.0	4.27 ± 0.49	3.92 ± 0.61	3.83 ± 0.27	3.43 ± 0.43
1408.0	3.5	4.99 ± 0.30	4.75 ± 0.28	4.14 ± 0.20	4.23 ± 0.26
	4.0	5.01 ± 0.25	4.74 ± 0.29	4.15 ± 0.24	4.25 ± 0.15
	4.5	5.03 ± 0.20	4.73 ± 0.28	4.18 ± 0.24	4.24 ± 0.17
	5.0	5.05 ± 0.24	4.74 ± 0.30	4.19 ± 0.23	4.25 ± 0.17
	6.0	5.06 ± 0.23	4.72 ± 0.26	4.25 ± 0.19	4.24 ± 0.18
	7.0	5.07 ± 0.23	4.70 ± 0.25	4.27 ± 0.12	4.24 ± 0.16
energy (keV)	$n \cdot \sigma$	FWHM$_{14,L}$	FWHM$_{14,R}$	FWHM$_{17,L}$	FWHM$_{17,R}$
344.3	3.5	3.69 ± 0.34	3.40 ± 0.35	4.12 ± 0.36	4.09 ± 0.15
	4.0	3.73 ± 0.46	3.50 ± 0.35	3.98 ± 0.30	4.11 ± 0.06
	4.5	3.75 ± 0.45	3.44 ± 0.36	4.01 ± 0.32	4.06 ± 0.15
	5.0	3.72 ± 0.42	3.44 ± 0.32	3.97 ± 0.31	3.94 ± 0.23
	6.0	3.69 ± 0.38	3.49 ± 0.36	3.93 ± 0.29	4.02 ± 0.24
	7.0	3.72 ± 0.38	3.37 ± 0.26	3.90 ± 0.33	4.02 ± 0.26
1408.0	3.5	4.17 ± 0.21	3.86 ± 0.23	4.00 ± 0.31	4.14 ± 0.21
	4.0	4.16 ± 0.22	4.00 ± 0.26	4.17 ± 0.24	4.10 ± 0.16
	4.5	4.20 ± 0.22	4.03 ± 0.21	4.17 ± 0.25	4.12 ± 0.15
	5.0	4.23 ± 0.19	4.04 ± 0.22	4.17 ± 0.26	4.10 ± 0.16
	6.0	4.23 ± 0.18	4.06 ± 0.23	4.19 ± 0.28	4.12 ± 0.23
	7.0	4.24 ± 0.19	4.08 ± 0.25	4.23 ± 0.28	4.14 ± 0.22

Table 7.8: Average FWHM for core and segments of interest, fitted with one-sided Gaussians plus first order polynomial background to the left (L) and right (R) half of the fit window.

energy (keV)	$n \cdot \sigma$	$p(\chi^2/\mathrm{NDF})_{core,L}$	$p(\chi^2/\mathrm{NDF})_{core,R}$	$p(\chi^2/\mathrm{NDF})_{11,L}$	$p(\chi^2/\mathrm{NDF})_{11,R}$
344.3	3.5	0.84 ± 0.23	0.82 ± 0.26	0.87 ± 0.23	0.83 ± 0.16
	4.0	0.81 ± 0.24	0.82 ± 0.25	0.87 ± 0.20	0.83 ± 0.17
	4.5	0.79 ± 0.27	0.81 ± 0.26	0.89 ± 0.14	0.81 ± 0.20
	5.0	0.80 ± 0.29	0.80 ± 0.27	0.86 ± 0.14	0.82 ± 0.21
	6.0	0.87 ± 0.15	0.81 ± 0.24	0.76 ± 0.25	0.78 ± 0.31
	7.0	0.87 ± 0.17	0.86 ± 0.21	0.79 ± 0.16	0.75 ± 0.33
1408.0	3.5	0.56 ± 0.38	0.92 ± 0.12	0.91 ± 0.05	0.78 ± 0.11
	4.0	0.56 ± 0.36	0.87 ± 0.17	0.86 ± 0.04	0.71 ± 0.23
	4.5	0.51 ± 0.38	0.86 ± 0.19	0.83 ± 0.04	0.68 ± 0.30
	5.0	0.53 ± 0.36	0.84 ± 0.21	0.81 ± 0.03	0.62 ± 0.32
	6.0	0.56 ± 0.34	0.82 ± 0.23	0.78 ± 0.12	0.57 ± 0.31
	7.0	0.55 ± 0.33	0.79 ± 0.25	0.78 ± 0.18	0.52 ± 0.31

energy (keV)	$n \cdot \sigma$	$p(\chi^2/\mathrm{NDF})_{14,L}$	$p(\chi^2/\mathrm{NDF})_{14,R}$	$p(\chi^2/\mathrm{NDF})_{17,L}$	$p(\chi^2/\mathrm{NDF})_{17,R}$
344.3	3.5	0.78 ± 0.29	0.82 ± 0.29	0.75 ± 0.26	0.58 ± 0.20
	4.0	0.81 ± 0.20	0.80 ± 0.29	0.72 ± 0.32	0.48 ± 0.19
	4.5	0.75 ± 0.25	0.78 ± 0.32	0.72 ± 0.30	0.38 ± 0.24
	5.0	0.77 ± 0.24	0.73 ± 0.34	0.75 ± 0.26	0.51 ± 0.24
	6.0	0.71 ± 0.31	0.76 ± 0.27	0.64 ± 0.34	0.63 ± 0.21
	7.0	0.72 ± 0.27	0.72 ± 0.30	0.64 ± 0.33	0.74 ± 0.23
1408.0	3.5	0.67 ± 0.21	0.67 ± 0.31	0.69 ± 0.21	0.68 ± 0.28
	4.0	0.59 ± 0.25	0.63 ± 0.31	0.78 ± 0.17	0.68 ± 0.33
	4.5	0.48 ± 0.24	0.58 ± 0.32	0.71 ± 0.20	0.62 ± 0.32
	5.0	0.48 ± 0.30	0.56 ± 0.31	0.72 ± 0.15	0.57 ± 0.32
	6.0	0.41 ± 0.32	0.54 ± 0.31	0.71 ± 0.12	0.52 ± 0.34
	7.0	0.51 ± 0.24	0.47 ± 0.31	0.78 ± 0.16	0.51 ± 0.35

Table 7.9: Average $p(\chi^2/\mathrm{NDF})$ for the fit with one-sided Gaussians plus first order polynomial background to the left (L) and right (R) half of the fit window.

Gaussian Plus First Order Polynomial, Fitted in Two Steps

The final approach that was tested was to fit Gaussian and first order polynomial background separately. After a preliminary fit, a background region of width $n_{BG} \cdot \sigma$ and a peak region inside this of width $n_{peak} \cdot \sigma$ were chosen. A first order polynomial was fitted to the data inside the background region, not taking into account the data points that are part of the peak region. Then a Gaussian plus first order polynomial was fitted to the peak region, where the background parameters were set to the values determined by the background fit. They were allowed to vary within the range given by the one sigma errors from the background fit.

This procedure was carried out for different combinations of n_{BG} and n_{peak}. The $p(\chi^2/_{\mathrm{NDF}})$ values for the different combinations were compared. The average FWHM and $p(\chi^2/_{\mathrm{NDF}})$ for core and segment are listed in table A.13 and A.14. Figure 7.11 shows the average $p(\chi^2/_{\mathrm{NDF}})$ versus the different choices for n_{BG} and n_{peak}. The

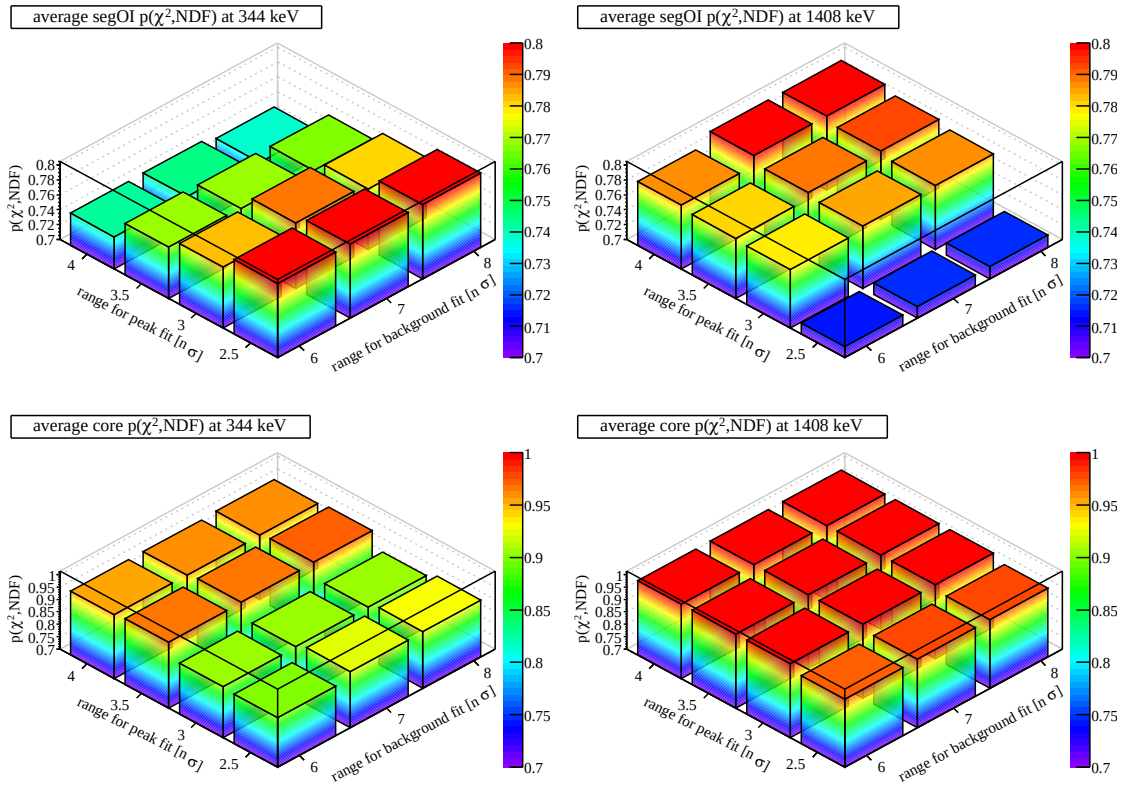

Figure 7.11: Average $p(\chi^2/_{\mathrm{NDF}})$ for core and segment of interest for different combinations of background fit window $n_{BG} \cdot \sigma$ and peak fit window $n_{peak} \cdot \sigma$. Please note the different ranges of the y-axes.

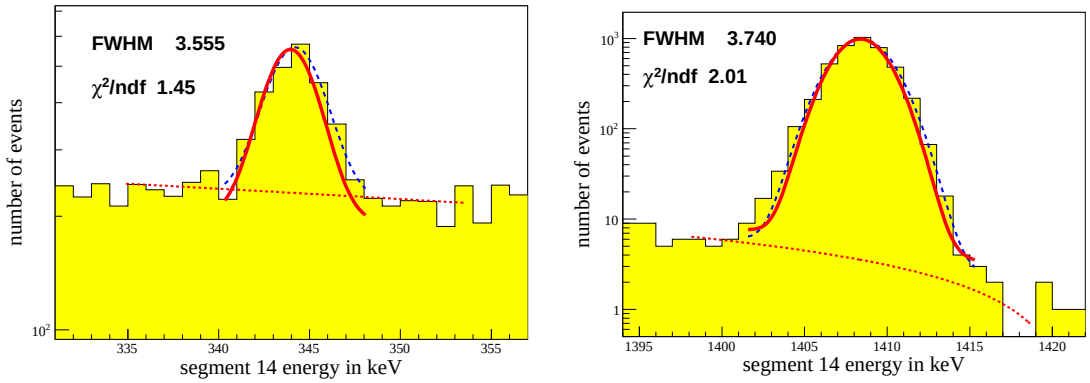

(a) (b)

Figure 7.12: Example for the fit with first order polynomial and Gaussian in separate steps, fitted to the segment energy of segment 14 (dataset taken at z=203 mm). The fit window parameters displayed are $n_{BG} = 6$ in combination with (a) $n_{peak} = 2.5$ for 344.3 keV and (b) $n_{peak} = 4.0$ for 1408.0 keV. The thick line is the total fitted function, the dotted line indicates the fitted background, the dashed line is the initial fit that was used to set the windows.

statistical variations ware significantly less than the observed dependency. For the 344.3 keV line, a smaller n_{peak} seems better suited to describe the segment data, while for the 1408.0 keV line a larger n_{peak} in general yielded the lower $p(\chi^2/_{\mathrm{NDF}})$ values. This is attributed to the fact that the peak-to-background ratio for the 1408.0 keV line is larger than for the 344.3 keV line (see table 7.2).

For any given n_{peak}, a widening of the fit window for the background fit (larger n_{BG}) does not improve the fit.

Figure 7.12 shows the segment energy fit at z=203 mm for both energies, figure 7.13 shows the results of the fit, with $n_{BG} = 6$ and $n_{peak} = 2.5$ for 344.3 keV and $n_{peak} = 4.0$ for 1408.0 keV.

7.3.2 Uncertainties

Systematic Errors from the fitting procedure

The absolute value of the FWHM for core and segment changed depending on which of the fit methods described in the previous section was used. For a given fit method, the outcome of the fit depends on the energy range in which the data is fitted.

The results from the different fits were compared to estimate the systematic uncer-

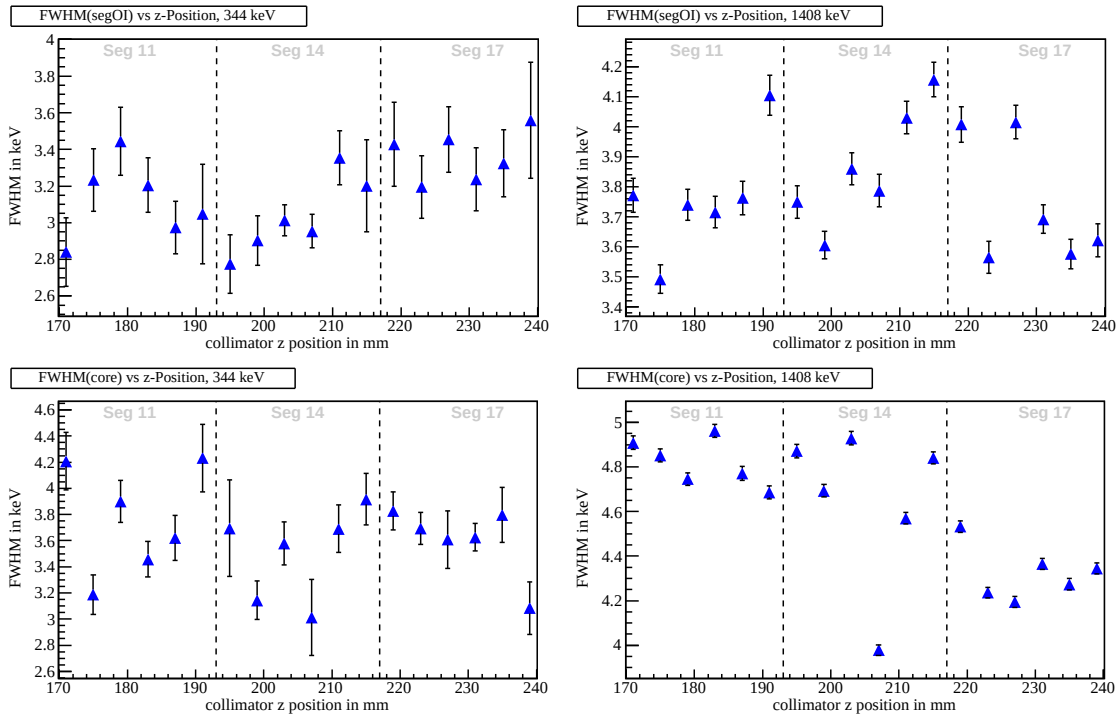

Figure 7.13: Resulting segment (top) and core (bottom) FWHM from the Gaussian plus first order polynomial background fit in two steps for $n_{BG} = 6$ and $n_{peak,344} = 2.5$, $n_{peak,1408} = 4.0$, with statistical errors. Please note the different ranges of the y-axes.

tainty due to the fitting procedure. Figure 7.14 shows the procentual deviations of the fit results between the fit with a Gaussian plus first order polynomial background with a 5σ fit window and the other fit methods.

For the fits to the 344.3 keV ^{152}Eu line, the deviations are within $\pm 5.8\%$ for 90% of the datasets.

The peak-to-background ratio for the 1408.0 keV ^{152}Eu line was considerably larger than for the 344.3 keV line (see table 7.2). Therefore, the influence on the background on the fit result was reduced. The deviations between the results from the different fit procedures are within $\pm 1.2\%$ for 90% of the datasets.

As it is a priori not known which background model is correct and thus which fit procedure best describes the reality, these values are taken as systematic uncertainties.

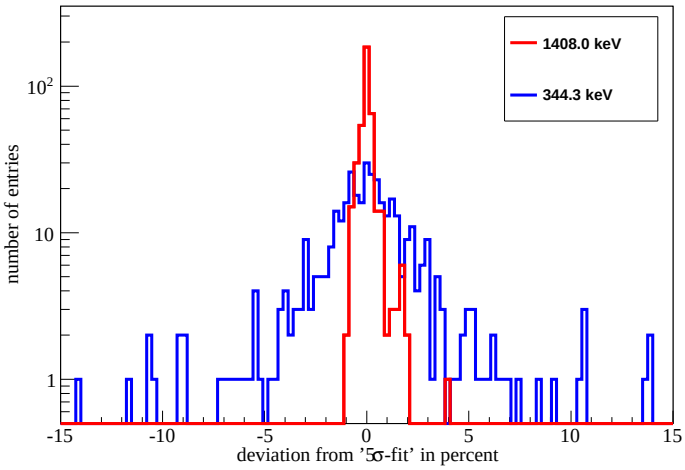

Figure 7.14: Procentual deviations of the fit results between the fit with Gaussian plot first order polynomial background with a 5σ fit window and the other fit methods.

Variations in the Electronic Noise

The datasets were taken over a time span of several weeks. Therefore, variations in the electronic noise can be expected.

Some experimental conditions such as room temperature, humidity or electronics activity in the neighboring laboratories could vary, which might affect the resolution, especially the electronic noise: The detector and the first stages of the preamplifiers are connected with long, unshielded cables, as described in 5.4.1. Gerdalinchen II is not a perfect Faraday cage. Thus the cables inside can easily pick up disturbances from the surroundings, creating electronic noise.

Additionally, refilling the cryostat with liquid nitrogen leads to an increased noise level due to microphonics. Therefore, the measurements for this analysis were only started after a waiting period of at least 15 hours after the last refill. Figure 7.15 shows the resolution of core and segment of interest in dependence of the waiting time after refilling the cryostat and indicated the date at which the respective datasets were taken. It can be seen that the dataset (z = 207 mm, on the 23.03.2010) in which the core resolution was noticeable smaller than for the datasets at neighboring z-positions, especially at 1408.0 keV, was taken after a much longer waiting time, which might explain the better resolution.

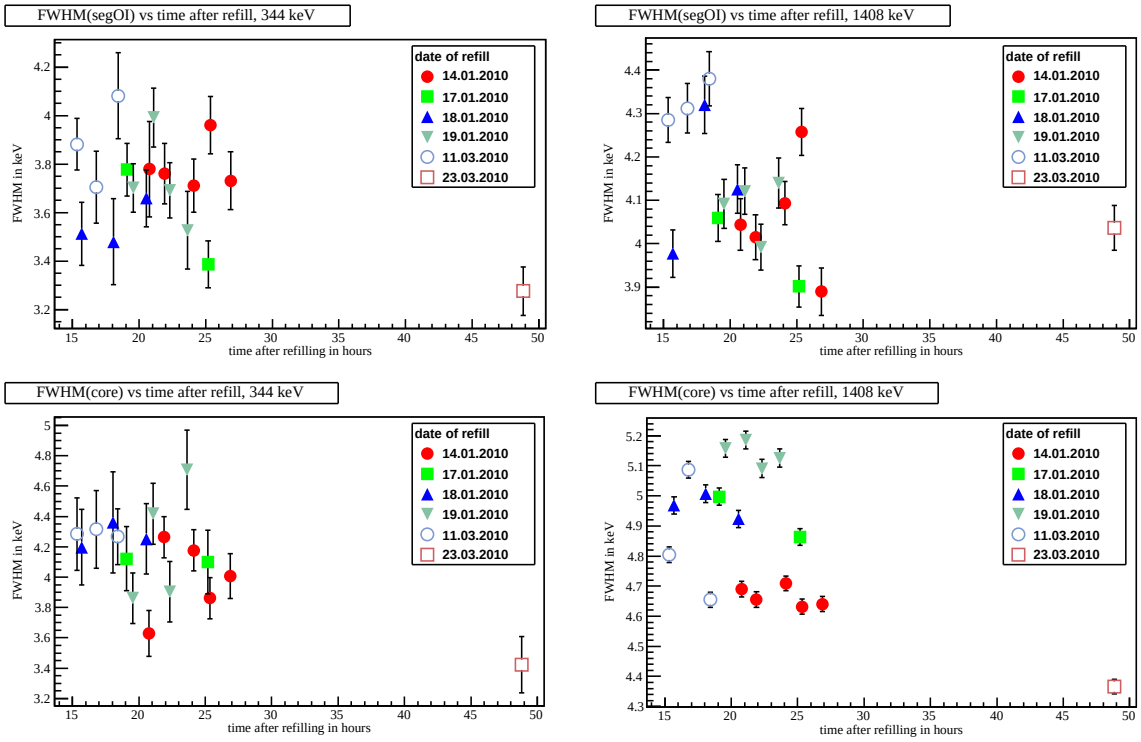

Figure 7.15: FWHM in dependence of waiting time after refilling the cryostat. The FWHM values are those determined using the fit with Gaussians plus first order polynomial background within a fit range of $5 \cdot \sigma$, with statistical errors.

7.4 Results

Out of the fit methods described above, the lowest average $p(\chi^2/_{\mathrm{NDF}})$ for the fit of all data points was the fit procedures with Gaussian plus first order polynomial background fitted over a 5σ fit window. Figure 7.17 shows the results from this fit, with statistical and systematic uncertainties. The average values of the FWHM for the z-position ranges corresponding to the individual segments are also shown.

Figure 7.16 shows the deviation of the individual FWHM values from the corresponding averages. For the fits to the 344.3 keV ^{152}Eu line, 90% of the fitted points are located within ± 11.2% around the mean value, and within ± 6.4% for the 1408.0 keV line.

These variations can be attributed to the experimental conditions, such as electronic noise due to the long cables between the detector and the first stage of the preamplifiers, and to the uncertainties due to the fit procedure. If there is an effect of the partial metallization of the segment contacts on the resolution, it can not

be deduced from the data taken under the described experimental conditions. This leads to the conclusion that if such an effect exists, it is below $\mathcal{O}(10\%)$.

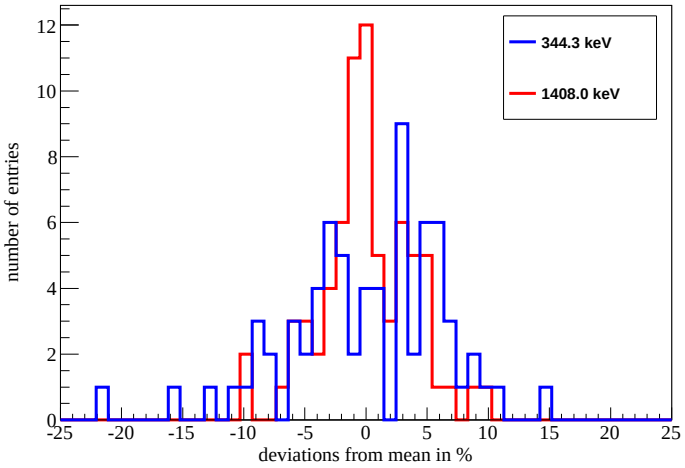

Figure 7.16: Procentual deviations of the fit results from the FWHM value averaged over the individual segments, for 344.3 keV and 1408.0 keV.

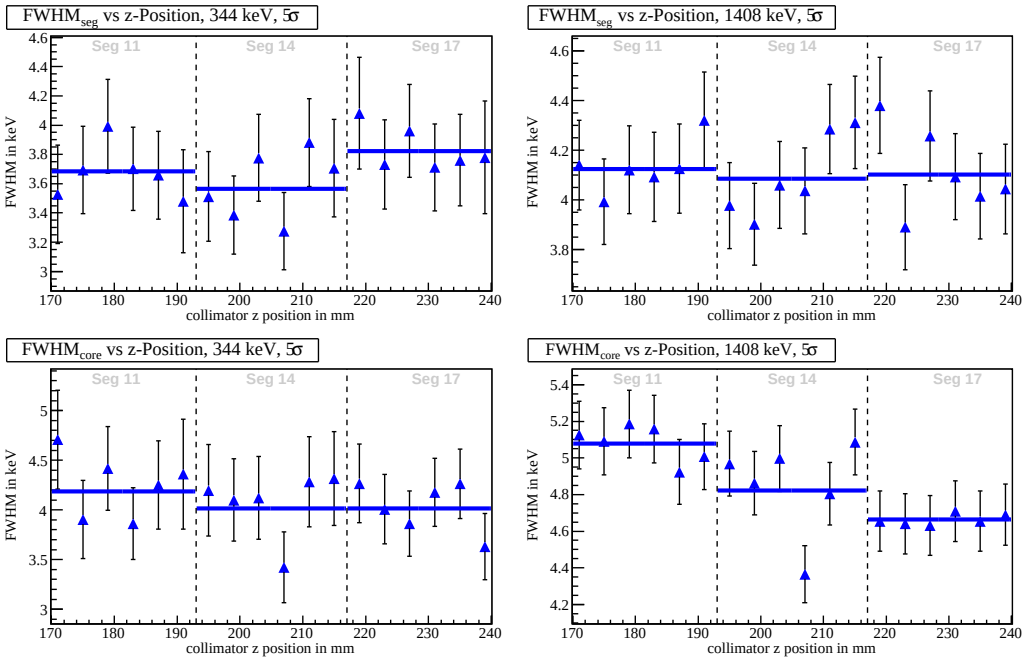

Figure 7.17: Resulting segment (top) and core (bottom) FWHM for the fit with Gaussian plus first order polynomial background within a fit range of $5 \cdot \sigma$. The systematic errors due to the fitting procedure are included in this plot. The lines indicate the average of the FWHM over the z-position ranges corresponding to the scanned segments. Please note the different ranges of the y-axes.

8 Homogeneity of the Detector Efficiency

The active volume of the detectors is one of the parameters that have to be taken into account in the determination of the half-life of neutrinoless double beta decay from measured events. An extensive knowledge of the detector properties is desirable, therefore the distribution of the active volume over the detector is interesting, especially since the passivation layers on top and bottom may cause surface effects.

In this chapter, the homogeneity of the active volume of the 18-fold segmented HPGe detector Siegfried I (described in section 5.3.2) is studied.

8.1 Ways of Determining the Active Volume

In the GERDA Experiment, the neutrino-accompanied decay of ^{76}Ge offers a good way of determining the active volume, since the events from this decay will be homogeneously distributed throughout the detector.

However, this only works in the low-background environment of the final experiment. For studying the active volume of the prototype detectors in a normal lab environment, a different method has to be applied. A common approach is the comparison of measured data with simulations. A difficulty that arises in the cause of this approach is that uncertainties in the simulation of the detector and its properties, especially its geometry, can lead to significant systematic effects in the simulation. An 18-fold segmented detector offers a way to eliminate some of those systematic effects: With such a detector it is possible to examine the top, middle and bottom layers individually, which permits the calculation of double ratios (DR) between the number of events in outer layer and central layer, from experiment and simulation respectively. By taking theses double ratios, geometrical effects in the simulation are reduced, since the analysis compares the ratios between detector layers in the

simulation with detector layers in the experiment, instead of comparing simulation and experiment directly. Since systematic offsets of the simulation occur for both middle and outer layers, they can cancel each other out.

$$DR = \frac{Outer\ Layer_{experiment}}{Middle\ Layer_{experiment}} : \frac{Outer\ Layer_{simulation}}{Middle\ Layer_{simulation}} \tag{8.1}$$

8.2 Experimental Setup

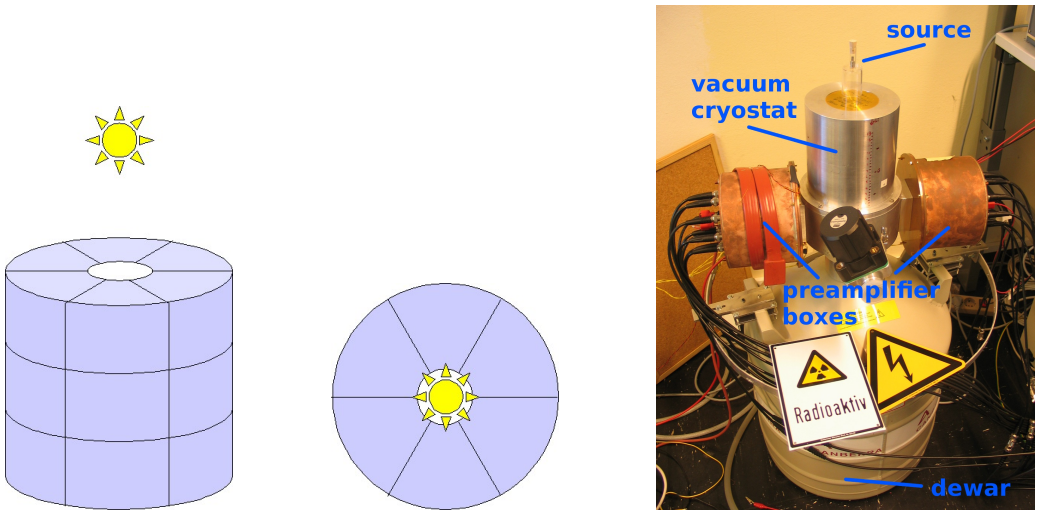

(a) (b) (c)

Figure 8.1: Experimental Setup: Schematic drawing (not to scale) a) from the side and b) from the top. c) Photo of the teststand with radioactive source on top.

Data was taken using the Siegfried I detector inside a vacuum teststand (see 5.4.1). Measurements were taken with three different calibration sources: a 100 kBq ^{228}Th source, a 50 kBq ^{152}Eu source and a 60 kBq ^{60}Co source, which were placed 10 cm above the center of the detector cryostat in consecutive measurements. For each event the energy and time information of the core and segment electrodes were recorded with the data acquisition described (DAQ) in section 5.4.2.

The fact that the sources were located above the detector means that more interactions will take place in the top (segments 1-3, 16-18) than in the middle (segments 4-6, 13-15) layer, and more in the middle than in the bottom layer (segments 7-12). This is due to the principles described in section 5.1.3.

8.3 Dataset

The datasets used for this analysis were taken for the characterization of the first 18-fold segmented n-type HPGe detector [Abt07]. For each of the three sources mentioned above, $\approx$ 5 million events was recorded. The characteristics of these datasets are described below.

8.3.1 Resolution

As described in section 5.3.1, the full width at half maximum of a peak in an energy spectrum can be described as composed of contributions from the statistical e-h-pair variance (Fano term), the charge collection inefficiency and electronic noise.

The detector resolutions determined from the data for the different gamma energies are listed in table 8.1. Fitting with equation 5.10 (see figure 8.2) gives

$$\mathrm{FWHM} = \sqrt{\underbrace{(2.35)^2 \cdot 0.098 \cdot 2.96 \cdot (E_{core})}_{statistical\ variance} + \underbrace{1.52 \cdot (E_{core})^2}_{charge\ collection} + \underbrace{(1.32)^2}_{electronic\ noise}}\ keV. \quad (8.2)$$

The electronic noise contribution to the resolution is significantly smaller than for the measurements in the GII teststand (see equation 6.1. This could be expected due to the differences between the two teststands described in section 5.4.1.

Source	Energy (keV)	FWHM_{core}
^{228}Th	510.8	1.820 ± 0.007
	583.2	1.798 ± 0.003
	860.6	2.067 ± 0.011
	1592.5	3.311 ± 0.051
	2614.5	4.079 ± 0.010
^{152}Eu	121.8	1.398 ± 0.002
	344.3	1.563 ± 0.002
	778.9	1.967 ± 0.006
	964.1	2.154 ± 0.006
	1112.1	2.323 ± 0.008
	1408.0	2.628 ± 0.007
^{60}Co	1173.2	2.378 ± 0.003
	1332.5	2.561 ± 0.003

Table 8.1: Siegfried I core FWHM for different energies.

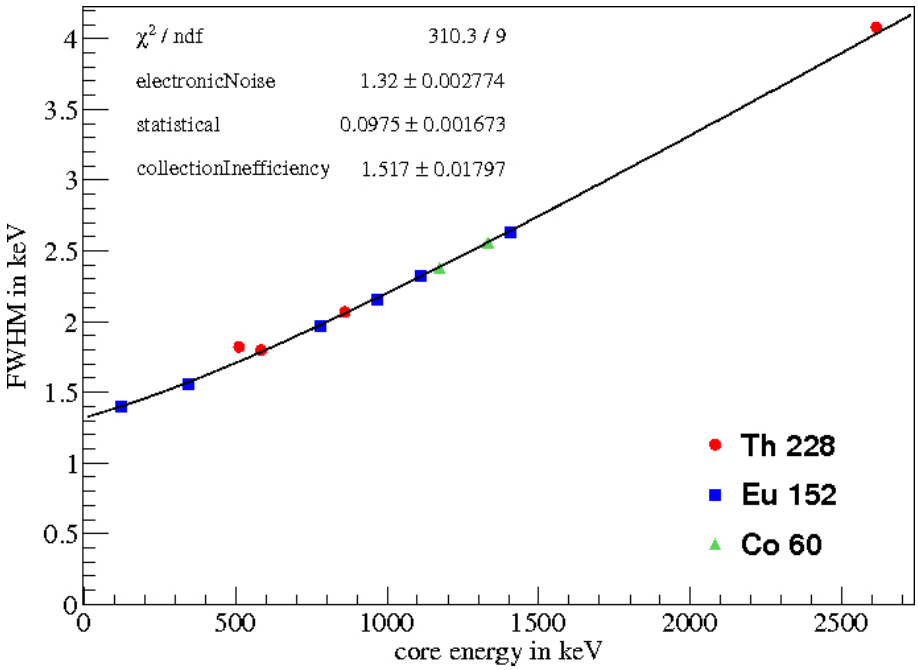

Figure 8.2: Siegfried I core FWHM over energy with fit function.

8.3.2 Crosstalk

For one detector hemisphere (segments 1-9), cross-talk between the amplified core signal and the unamplified segment signal lines was observed in this setup. This was due to the placement of the core FET close to the detector itself. The crosstalk-ratios for segments 1-9 have been calculated in [Abt07] and are listed in table 8.2.

Segment	1	2	3	4	5	6	7	8	9
κ_{seg}	0.128	0.014	0.009	0.033	0.014	0.037	0.014	0.037	0.385

Table 8.2: Crosstalk coefficients κ_{seg} of segments 1-9.

The crosstalk ratios were taken into account in the energy calibration of the recorded data: In first order, the true energy deposit in a segment, $E_{seg,true}$ can be calculated as

$$E_{seg,true} = E_{seg,meas} - \kappa_{seg} E_{core}, \tag{8.3}$$

where $E_{seg,meas}$ and E_{core} are the measured values for the segment and core respectively. This calculation neglects second order effects, which were found to be quite small and do not need to be corrected for this application [Abt07].

8.3.3 Selection of Events

From the data recorded with the described setup, single segment events, i.e. events with energy deposit in only one segment were chosen and all segments of a layer grouped together. The requirement for a single segment was that the energy deposit in all segments except one was less than 20 keV, and that the energy of the corresponding segment was within 2 σ of the core energy. A 20 keV threshold was chosen to reject signals due to low-amplitude noise, however it will also lead to a less strict background rejection than a lower threshold would.

The single segment spectra were fitted with a gauss-function plus a first order polynomial (for photon peak plus background) around the following peaks:

- 510.8 keV, 583.2 keV, 860.6 keV and 2614.5 keV for the ^{228}Th data,
- 344.3 keV, 778.9 keV, 964.1 keV, 1085.9 keV, 1112.1 keV and 1408.0 keV for the ^{152}Eu data,
- 1173.2 keV and 1332.5 keV for the ^{60}Co data.

The systematic uncertainties due to the fitting procedure were estimated to be $\lesssim$5%, based on the discussion in section 7.3.2. This assumption over-estimates the uncertainties due to fitting for the higher energy peaks, which will lead to a higher uncertainty on the values given for the double ratios.

The number of events used to form the double ratios is the number of events inside the Gaussian, within $\pm 2\sigma$ around the center of the peak.

The single ratios between the resulting number of entries for top or bottom layer relative to the middle layer show the expected behavior due to the angular coverage and the energy dependence of the mean free path of a photon (figure 8.4): The top layer is closest to the source, which leads to a top-middle ratio larger than 1; the bottom layer is furthest away, thus the bottom-middle ratio is less than 1. Since the attenuation is smaller for photons with higher energies, the ratios decrease with higher energies. The errors bars in figure 8.4 are statistical uncertainties propagated to the ratios.

8.4 Simulation

The detector and its teststand were simulated in MaGe. The decay chains of ^{228}Th, ^{152}Eu, and ^{60}Co were simulated. The simulated datasets contain $\approx$ 2.5 million events

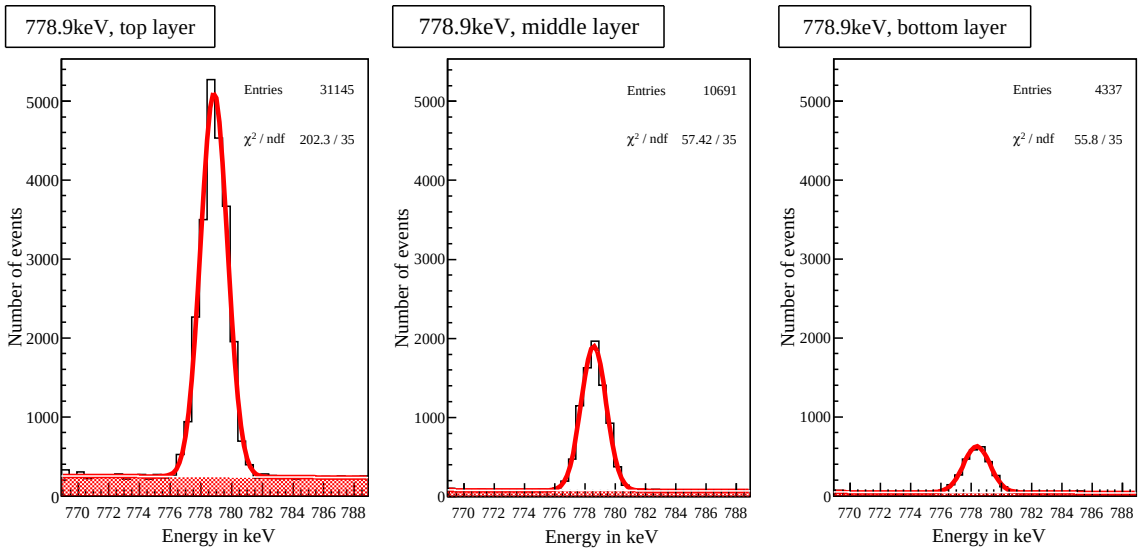

Figure 8.3: Example: fit for the 778.9 keV Eu-line.

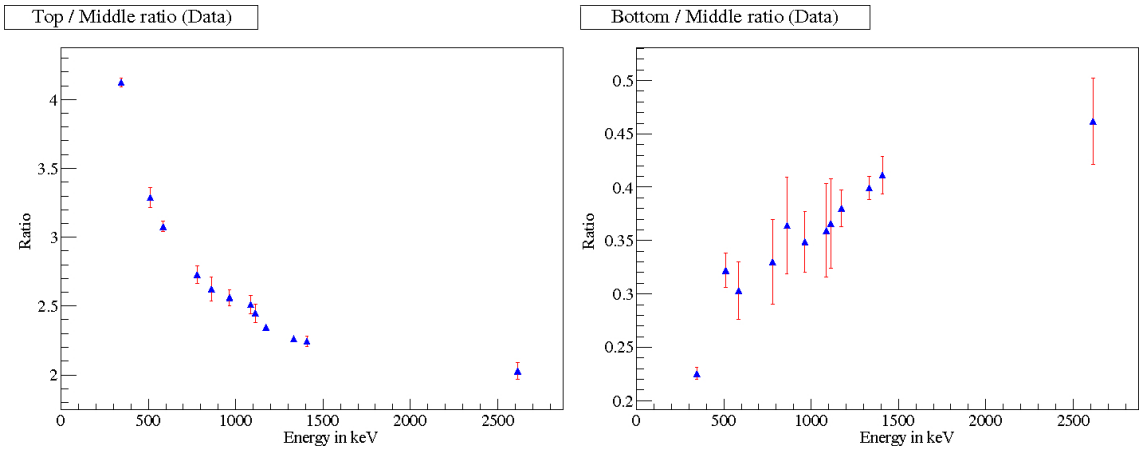

Figure 8.4: Single ratios of top/bottom layer to middle layer for the experiment data.

for ^{152}Eu and ^{60}Co and $\approx$ 5 million events for ^{228}Th.

To have a good comparability between experiment and simulation, the detector resolution as seen in the experimental setup was taken into account:
The equation for the resolution obtained in 8.3.1 was used to "smear" the simulation by taking the simulated events and multiplying the deposited energy with a random point from within a Gaussian with a standard deviation that corresponds to the resolution at this energy,

$$E_{smeared} = E_{dep} + rn \cdot \sigma(E), \tag{8.4}$$

where rn is a random number from a standard Gaussian and $\sigma(E)$ the value calculated from equation 8.2.

Afterwards, the simulated data were treated in the same way as the measured data, as described in section 8.3.3.

There are some differences between the experimental data and the simulation.

On the one hand, in the simulated events the energy was assigned to a segment if the energy was deposited at a position in this segment. The drift of the charge carriers was not taken into account. If the induced charge carriers are close to the segment boundaries, their drift trajectories can bend such that some of them are registered in the neighboring segment. This would increase the fraction of single segment events inside the considered segment in the simulation compared to the data.

On the other hand, instead of taking every produced electron-hole-pair into account, hits are clustered together in the simulation. The charge cloud created inside the detector by an energy deposit might therefore be smaller than in the experiment for boundary events. This can lead to a reduced number of single segment events in the simulation compared to the data.

These two differences can cause the single-segment-cut to have a different effect in data and simulation. However, this is a systematic effect that is in first order assumed to be canceled out by using the double ratios.

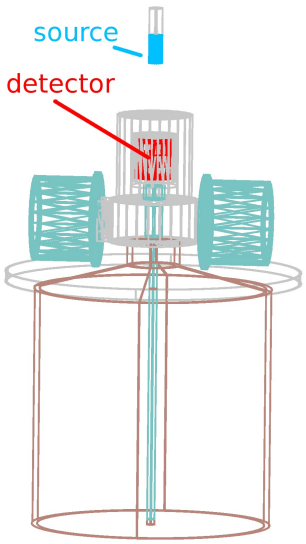

Figure 8.5: Schematic drawing of Siegfried I and its cryostat with source on top.

8.5 Error Analysis

8.5.1 Statistical Errors

Radioactive decays of the sources are randomly distributed in time following a Poisson distribution. The standard deviation for the number of counts within a time window is just the square root of the expected number of events, $\sqrt{\lambda}$ [Bar89].

8.5.2 Systematic Errors due to Geometry

Monte Carlo simulations were employed to get an estimate of the systematic errors due to geometrical factors in the measurement:
While the dimensions of the detector and the teststand are well known, the exact placement of the source could be established with less accuracy. To check how much of an effect the uncertainty in the position of the source has on the result, simulations with otherwise unchanged specifications were done with varied source positions:

- with the source 9.5 cm above the detector cryostat,
- with the source 10.5 cm above the detector cryostat,
- with the source 0.5 cm away from the center of the detector cryostat.

The top-middle and bottom-middle ratios of the simulated datasets with varied source position were compared with the simulated dataset in which the source was positioned 10 cm above the center of the detector cryostat. The maximum deviation between varied position-data and center-position data was employed as an estimate for the systematic error due to geometric uncertainties. The variations are of percent order and are listed in table 8.3.

E (keV)	344	511	583	779	861	964	1086	1112	1173	1333	1408	2615
Δ_{TM} (%)	0.5	2.5	1.1	2.4	2.4	2.2	2.0	2.8	0.7	0.7	0.5	2.8
Δ_{BM} (%)	0.2	0.8	2.2	3.2	3.0	2.0	3.3	3.2	1.4	0.7	0.9	2.0

Table 8.3: Systematic uncertainties due to geometry on top-middle ratio and bottom-middle ratio for different energies, given in percent.

8.5.3 DAQ Effects

In the DAQ version used to take the dataset described above, a bug with the coincidence window setting existed. This coincidence window is the time window within

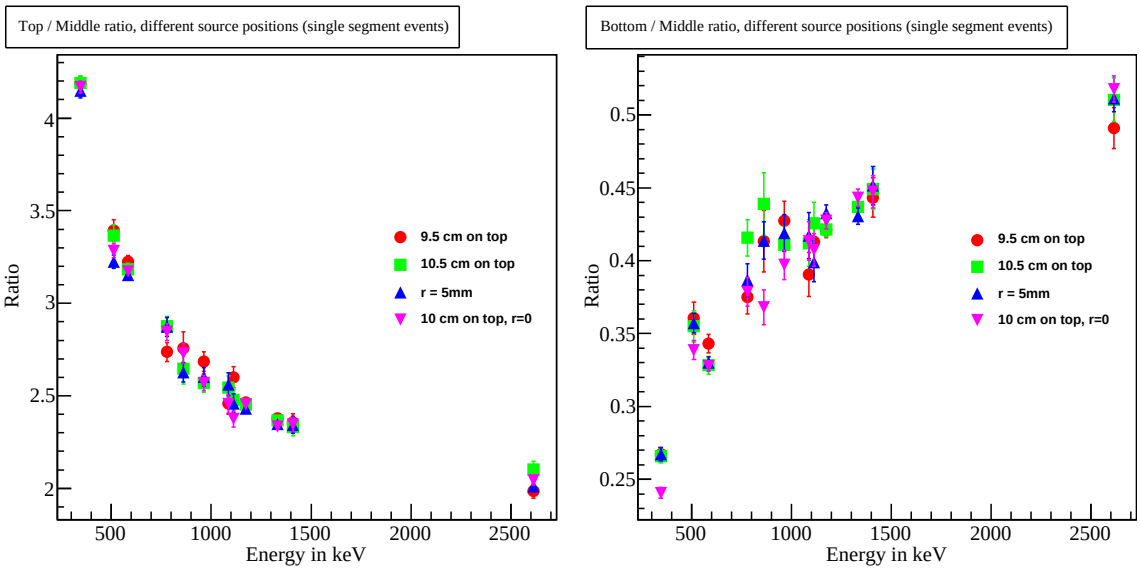

Figure 8.6: Top-middle and bottom-middle ratio calculated from simulations with varied source positions.

which the energies of the non-triggered channels, i.e. the segment channels, are taken into account. If a segment pulse arrives outside the coincidence window, the channel energy is set to zero. For some events the segment signal arrived late, thus the DAQ was unable to determine the event energy correctly.

From looking at another dataset recorded with the same DAQ version, but with the pulseshapes stored in addition to time and energy, it became apparent that this caused a small fraction of individual segment signals not to be recorded. This could cause an artificial increase of single segment events.

While this problem was fixed in later versions of the data acquisition system, it was still present during the data taking for this analysis. The distribution of these "problem events" was studied to determine if this effect occurred uniformly across all segments. An uneven distribution of such events could systematically bias the result, which depends on the number of events recorded in each segment.

There were two types of manifestations of the effect that could potentially alter the number of events-distribution derived from the data:

Type 1: One or several segments in which only the decreasing tail of a pulse was recorded. The energy is set to be zero by the DAQ.

Type 2: One or several segments in which a normal pulseshape was recorded and the energy is set to zero by the DAQ.

In both cases, the core energy is not equal to the sum of all segment energies, since the energy for one or more segments is lost. It was possible to evaluate the frequency with which these two types of events occurred for each individual segment by evaluating a data sample containing pulseshape information in addition to time and energy.

Type 1

Figure 8.7 shows an example of a typical type 1 event. The segment energies after calibration and crosstalk correction are all ≈ 0 keV, the core energy 1648.8 keV. The pulses in the left-hand-side of the plot (segments 1-9) are due to crosstalk, while in segment 14 only the "decaying end" of a pulseshape was recorded. These kind of events can be identified by evaluating the parameters indicated in the plot, *Head*, *Tail* and *baseline*:
The parameter *Head* is the average over the first five bins, *TAIL* is the average over

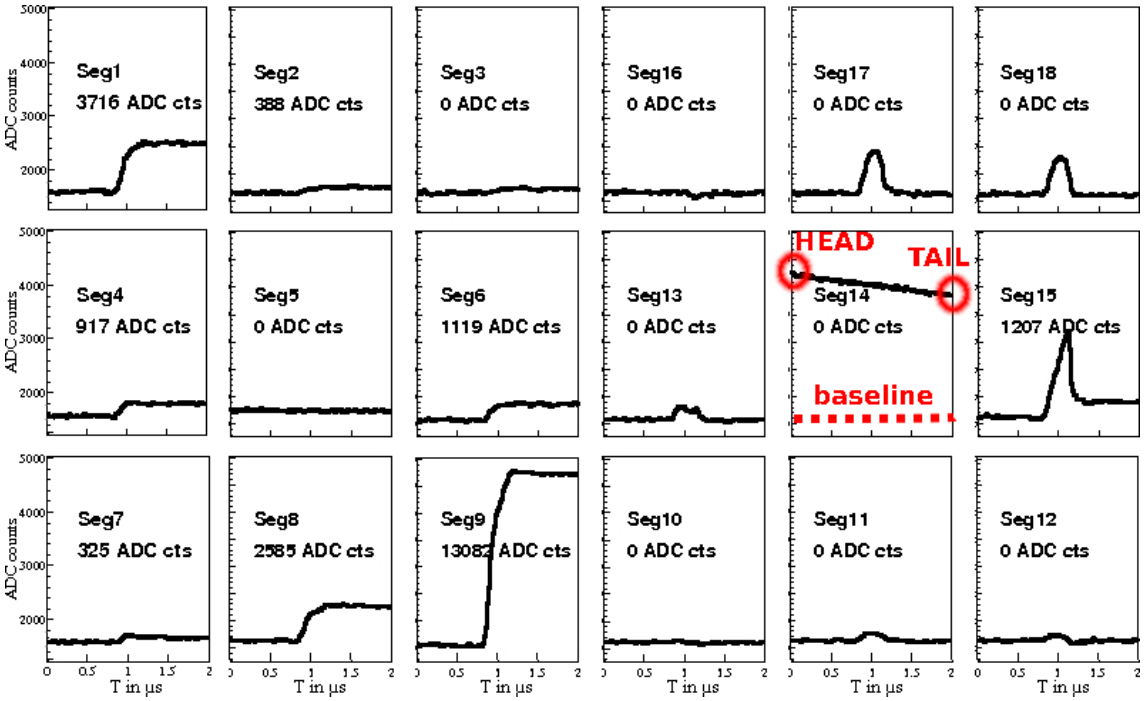

Figure 8.7: Pulseshapes of all 18 segments for a typical type 1 event. For each of the segments, the uncalibrated energy saved by the DAQ is given. The pulses in the left hemisphere are crosstalk pulses (see section 8.3.2) and have ≈ 0 keV energy after calibration and crosstalk correction. In the channel of segment 14 the decreasing tail of a pulse was recorded and the energy set to zero by the DAQ.

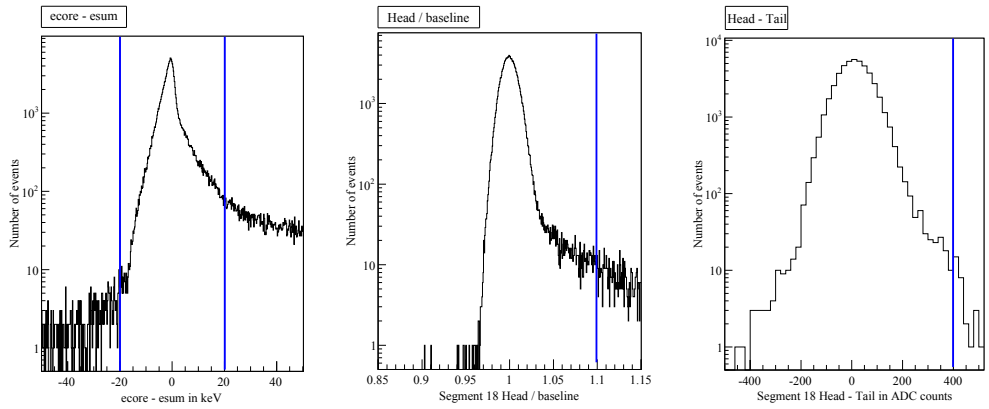

(a) (b) (c)

Figure 8.8: Selection criteria for type 1 events: parameter values (see text). (a) *ecore - esum* , (b) *Head / baseline* and (c) *Head - Tail* for segment 18.

the last three bins. The *baseline* for each segment was determined by averaging the first five bins of all events in which the segment energy of the respective segment calculated by the DAQ was zero and the core energy was roughly equal to the sum of all segment energies ($|ecore - esum| < 20keV$).

The following selection criteria for type 1 events were chosen:

- $|ecore - esum| > 20keV$
- $Head[seg] > 1.1 \cdot baseline[seg]$
- $Head[seg] - Tail[seg] > 400$

$|ecore - esum| > 20keV$ is a cut to find events with missing energy. Figure 8.8(a) shows the distribution of $ecore - esum$ around zero for all events.

The criterion $Head[seg] > 1.1 \cdot baseline[seg]$ is chosen to select those events with segment pulseform above the baseline. As an example, figure 8.8(b) shows the distribution of *Head[seg]/baseline[seg]* for segment 18 for events with $|ecore - esum| < 20keV$, i.e. events that are not presumed to be type 1 and should not be selected.

$Head[seg] - Tail[seg] > 400$ finds a decreasing pulse in that segment. As an example, figure 8.8(c) shows the $Head[seg] - Tail[seg]$ distribution for segment 18, for events with $|ecore - esum| < 20keV$, i.e. events that are not presumed to be type 1 and should not be selected.

For each segment, the number of events selected like this was compared to the total number of events in which an energy deposit in this segment was seen. The

results are given in table 8.4.

Segment	events in %	Segment	events in %	Segment	events in %
1	0.19 ± 0.09	7	0.24 ± 0.11	13	1.46 ± 0.17
2	0.11 ± 0.08	8	0.00 ± 0.01	14	0.26 ± 0.06
3	0.29 ± 0.11	9	8.70 ± 0.65	15	0.21 ± 0.06
4	0.05 ± 0.05	10	0.12 ± 0.05	16	0.03 ± 0.02
5	0.40 ± 0.16	11	0.27 ± 0.06	17	0.14 ± 0.04
6	0.67 ± 0.18	12	0.04 ± 0.03	18	0.31 ± 0.07

Table 8.4: Type 1 events in percent of total events with energy > 20k eV for all segments.

Segment 9 seems to be affected more strongly than the other segments. This can be explained by taking crosstalk into account. The high crosstalk coefficient for segment 9 (see 8.3.2) leads to an increased number of false positives in the selection of type 1 events. For each event occurring in segments other than segment 9, there will be also a significant crosstalk pulse in segment 9, which can also be affected by the DAQ problem. As an illustration for this, let us assume a data sample consists of 20000 events, with energy deposits in segment 9 for 5% of the events, i.e. there are 1000 events with energy deposit in segment 9. If 0.5% of those events are type 1 events, around 5 events are expected to be type 1 events. However, for events with energy deposit in other segments there will be crosstalk pulses in segment 9 that can be affected and are large enough to be caught by the selection criteria. If 0.5% of all those events show type 1 behavior too, this leads to ≈ 100 events being selected for segment 9, which would falsely lead to a fraction of 5%.

This effect can account for the large fraction of type 1 events in segment 9. For estimation of the systematic uncertainty we assume the fraction of the real type 1 events to be the average over the values from the other bottom layer segments.

Type 2

The pulseshapes for type 2 events all were correctly recorded. However, the DAQ failed to reconstruct the energy from the segment, which was then set to zero energy. These events can be identified with the following selection criteria:

- $|ecore - esum| > 20keV$
- *Tail[seg] - Head[seg] > 300*

- *PEnergy[seg]* $> 30\ keV$

$|ecore - esum| > 20keV$ is a cut to find events with missing energy, as for the type 1 events.

Tail[seg] - *Head[seg]* < 300 is chosen to ensure that a pulseshape was recorded for the event, not just noise. As an example, the distribution of *Head[seg]* - *Tail[seg]* is shown for segment 18 in figure 8.9(a).

For events that met the first two criteria, the energy *PEnergy* was calculated directly from the shape of the pulse using a procedure similar to that normally employed for the energy calculation by the DAQ. *PEnergy[seg]* $> 30\ keV$ was chosen to select events above the noise level. Figure 8.9(b) shows the distribution of *PEnergy[seg]* versus *Head[seg]* - *Tail[seg]* for segment 18. The area from which the events were selected due to the *PEnergy[seg]* and *Head[seg]* - *Tail[seg]* conditions is highlighted in red in the figure.

The fraction of type 2 events for the 18 segments are listed in table 8.5.

There are slight differences in the number of type 1 and type 2 events found for the individual segments. If the DAQ problem does not affect all segments in the same way, the differences are of <1.5% level for type 1 and <0.8% for type 2. The systematic uncertainties due to this on the volume calculation are included in the analysis in the next section.

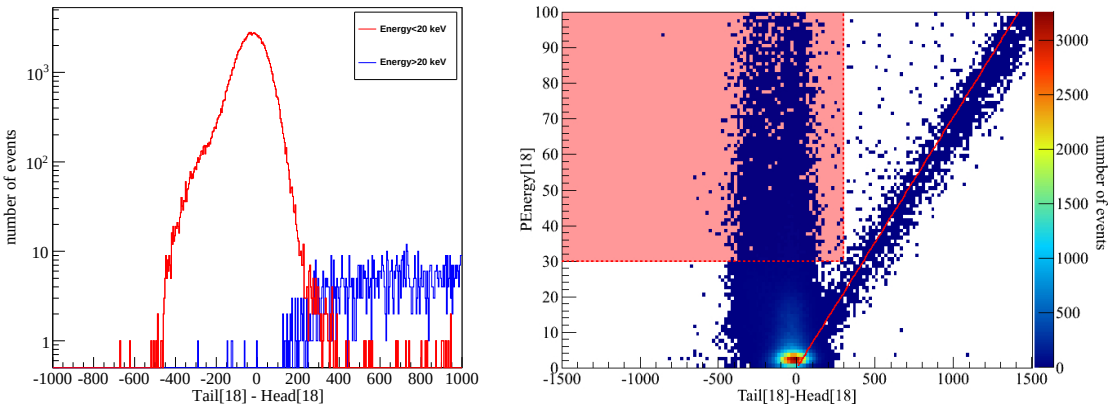

(a) (b)

Figure 8.9: Selection criteria for type 2 events, illustrated on the example of the parameter distributions for segment 18.

Segment	events in %
1	0.06 ± 0.02
2	0.45 ± 0.12
3	0.26 ± 0.09
4	0.63 ± 0.09
5	0.46 ± 0.09
6	0.28 ± 0.06

Segment	events in %
7	0.39 ± 0.13
8	0.22 ± 0.04
9	0.12 ± 0.02
10	0.53 ± 0.10
11	0.61 ± 0.09
12	0.61 ± 0.11

Segment	events in %
13	0.48 ± 0.10
14	0.56 ± 0.09
15	0.58 ± 0.10
16	0.79 ± 0.12
17	0.31 ± 0.06
18	0.54 ± 0.10

Table 8.5: Type 2 events in percent of total events with energy>20keV for all segments.

8.6 Fit of the Double Ratio, Calculation of Active Volume

The double ratio between the number of events in outer layer and central layer in experimental and simulated data (equation 8.1) was calculated and fitted with a constant both for top and bottom layer (figure 8.10). The errors consist of statistical plus systematic errors.

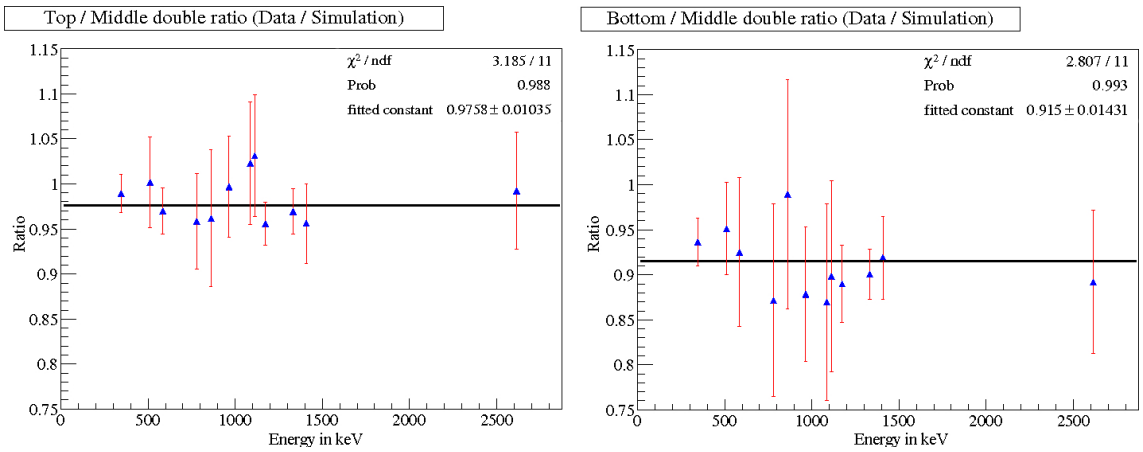

Figure 8.10: Calculated double ratios and fit with a constant.

The fit resulted in the following double ratios:

$$DR_{top/middle} = 0.98 \pm 0.01 \ , \tag{8.5}$$

$$DR_{bottom/middle} = 0.92 \pm 0.01 \ . \tag{8.6}$$

These double rations can now be used to determine the active volume of the

detector:
Calculating the volume from the geometrical parameters of the detector, taking into account a dead layer on the inner surface of 0.5 mm, yields

$$V_{geom} = 301\ cm^3\ . \tag{8.7}$$

A priori, it was assumed that the middle layer consists of 100 percent active volume (which is not entirely true, but close enough for this purpose since the volume of the middle layer that can be affected by surface effects is significantly smaller than for the top and bottom layer). Assigning the top and bottom layer a percentage of active volume corresponding to the double ratios between them and the middle layer given above in 8.5 and 8.6 , the active volume can be calculated as

$$V_{active} = V_{geom} \cdot \frac{1}{3}\left(DR_{top/middle} + 1 + DR_{bottom/middle}\right) = (289\ \pm\ 2)\ cm^2. \tag{8.8}$$

8.7 Conclusions

As anticipated, the active volume is smaller than what would be expected if only the geometry alone was taken into account.

The outer layers differ from the middle layer in terms of the active volume. For this detector the effect is especially pronounced for the bottom layer.

A possible explanation is the inhomogeneity of the impurity density. According to the specification given by the manufacturer (table 5.1), the net impurity concentration changes from 0.70 - 1.35 10^{10} cm^{-3} from top to bottom. The electric field inside the detector is sensitive to the impurity distribution, since it depends on the space charge density, which is caused by the effective number of impurities. This could result in the charge carrier drift trajectories being bent in the z-direction. Then it is possible that the data contains events in which the energy is deposited in the geometrical bottom layer, but the holes drift upwards to one of the electrodes in the middle layer and are registered there. This could explain why the effective volume of the bottom layer is reduced.

A part of this effect might be caused by the cut on events with energy deposit in single segments. This cut will neglect events that occurred at the segment boundaries and show up in two segments. Assuming this happens for events within a 1 mm wide region around the boundaries, from geometrical considerations, this can be

estimated concern $\approx 2.8\%$ of the volume for the top and bottom layer and $\approx 4.1\%$ of the detector volume for the middle layer.

Other possible explanations for the observed effect are the passivation layers on the detector surfaces and the distribution of the impurity concentration.

9 Summary and Outlook

Segmented HPGe detectors can help recognize background in low background experiments such as GERDA. 18-fold segmented n-type HPGe detectors had been developed for this purpose earlier. Different systematic effects of 18-fold segmented high-purity germanium detectors were studied in this thesis.

The effects caused by a floating detector segment were studied. An approach to reconstruct its energy spectrum was presented. The reconstruction procedure performed well in finding events in which energy was deposited in the disconnected segment, while the number of misidentified events is negligible.

The energy spectrum of reconstructed events was found to have an energy resolution comparable to the normal resolution of other segments. In the future, the development of a more complex reconstruction procedure could further improve the energy resolution of the reconstructed energy spectrum, as well as the efficiency of identifying events in a floating segment. Such a procedure would have to make use of the energy information of all segments instead of only the four segments with the highest capacitive coupling. The analysis shows that segmented detectors with one lost contact can still yield nearly all information.

The question whether a partial metallization of the segment contacts has an effect on the energy resolution of the detector was addressed. For this purpose, data was taken with a prototype detector with a mixed metallization scheme was used. Data was taken inside the liquid nitrogen teststand Gerdalinchen II. Different fitting methods were used to investigate the systematics of the fit procedure used to determine the resolution.

Within the uncertainties, no effect of the partial metallization on the resolution were found. An upper limit was set for such an effect.

Future investigations on the effect of the partial metallization could be done in an environment that is less effected by electronic noise. This could be done in the new teststand GALATEA, which is currently under construction at the MPI für Physik

in Munich. The detector and source will be inside a vacuum teststand, i.e. with no material in between them. It will be possible to scan the detector in fine steps with a tunable laser. Thus it should be possible to obtain data with a smaller beam spot size and investigate the effects of the partial metallization in more detail.

The homogeneity of the active volume of another 18-fold segmented prototype detector was studied. Double ratios between the number of events in the outer layers and central layer from experimental data and Monte Carlo simulation were compared.

As anticipated, the active volume was found to be smaller than what would be expected if only the geometry alone was taken into account. Especially the bottom layer showed a smaller active volume, compared to the top and middle layers. This could be due to the inhomogeneity of the impurity density, but also due to surface effect.

Future studies should investigate the influence of the impurity distribution on the z-component of the charge carrier drift. In order to do this, the implementation of the charge carrier drift in the simulation will have to be carefully evaluated and adapted. A comparison to measurements done with GALATEA could improve the understanding of the effects of the impurity density on the drift trajectories of the charge carriers.

Appendix A: Fit Results

z (mm)	$n \cdot \sigma$	FWHM$_{core}$ (keV)	$p(\chi^2/_{\mathrm{NDF}})_{core}$	FWHM$_{11}$ (keV)	$p(\chi^2/_{\mathrm{NDF}})_{11}$
171	3.5	4.96 ± 0.33	0.94	3.50 ± 0.18	0.16
	4	4.68 ± 0.28	1.00	3.41 ± 0.16	0.48
	4.5	4.66 ± 0.27	1.00	3.50 ± 0.16	0.62
	5	4.71 ± 0.26	0.99	3.53 ± 0.16	0.61
	6	4.68 ± 0.25	0.97	3.64 ± 0.16	0.94
	7	4.75 ± 0.25	0.97	3.57 ± 0.16	0.92
175	3.5	3.86 ± 0.22	0.99	3.64 ± 0.13	0.94
	4	3.94 ± 0.22	0.99	3.69 ± 0.12	0.91
	4.5	3.91 ± 0.20	0.98	3.67 ± 0.12	0.90
	5	3.90 ± 0.20	0.98	3.69 ± 0.11	0.91
	6	4.00 ± 0.19	1.00	3.70 ± 0.11	0.79
	7	3.87 ± 0.19	1.00	3.63 ± 0.11	0.79
179	3.5	4.39 ± 0.22	1.00	3.85 ± 0.13	0.97
	4	4.45 ± 0.22	1.00	3.92 ± 0.13	1.00
	4.5	4.45 ± 0.21	1.00	3.95 ± 0.12	1.00
	5	4.42 ± 0.20	1.00	3.99 ± 0.12	1.00
	6	4.55 ± 0.20	1.00	3.93 ± 0.12	1.00
	7	4.61 ± 0.21	1.00	3.88 ± 0.12	1.00
183	3.5	4.02 ± 0.21	0.94	3.83 ± 0.12	0.98
	4	4.11 ± 0.20	0.93	3.74 ± 0.11	1.00
	4.5	3.92 ± 0.17	0.99	3.73 ± 0.10	0.99
	5	3.86 ± 0.17	1.00	3.70 ± 0.10	0.98
	6	3.89 ± 0.16	0.99	3.71 ± 0.10	0.95
	7	3.77 ± 0.16	1.00	3.62 ± 0.10	0.98
187	3.5	4.05 ± 0.25	0.91	3.56 ± 0.13	0.81
	4	4.12 ± 0.24	0.87	3.63 ± 0.12	0.81
	4.5	4.19 ± 0.24	0.88	3.67 ± 0.12	0.85
	5	4.25 ± 0.23	0.84	3.66 ± 0.12	0.76
	6	4.35 ± 0.23	0.90	3.70 ± 0.12	0.87
	7	4.30 ± 0.22	0.81	3.68 ± 0.12	0.90
191	3.5	4.24 ± 0.37	0.87	3.51 ± 0.21	0.88
	4	4.53 ± 0.39	0.91	3.52 ± 0.19	0.76
	4.5	4.52 ± 0.37	0.90	3.54 ± 0.18	0.63
	5	4.36 ± 0.33	1.00	3.48 ± 0.18	0.77
	6	4.55 ± 0.34	1.00	3.50 ± 0.17	0.62
	7	4.44 ± 0.33	1.00	3.47 ± 0.18	0.60

Table A.1: FWHM and $p(\chi^2/_{\mathrm{NDF}})$ for core and segment 11 at 344.3 keV, fitted using a Gaussian plus first order polynomial background.

z (mm)	$n \cdot \sigma$	FWHM$_{core}$ (keV)	$p(\chi^2/_{\mathrm{NDF}})_{core}$	FWHM$_{11}$ (keV)	$p(\chi^2/_{\mathrm{NDF}})_{11}$
171	3.5	5.13 ± 0.04	1.00	4.13 ± 0.07	0.67
	4	5.12 ± 0.03	1.00	4.13 ± 0.06	0.51
	4.5	5.13 ± 0.03	1.00	4.13 ± 0.06	0.51
	5	5.13 ± 0.03	1.00	4.14 ± 0.06	0.38
	6	5.12 ± 0.03	1.00	4.14 ± 0.06	0.24
	7	5.07 ± 0.03	1.00	4.09 ± 0.06	0.19
175	3.5	5.13 ± 0.04	1.00	4.01 ± 0.07	0.85
	4	5.10 ± 0.03	1.00	3.96 ± 0.05	0.97
	4.5	5.09 ± 0.03	1.00	3.98 ± 0.05	0.99
	5	5.09 ± 0.03	1.00	3.99 ± 0.05	0.99
	6	5.09 ± 0.03	1.00	3.99 ± 0.05	1.00
	7	5.05 ± 0.03	1.00	3.93 ± 0.05	1.00
179	3.5	5.22 ± 0.04	0.96	4.10 ± 0.06	0.91
	4	5.20 ± 0.03	0.99	4.11 ± 0.05	0.94
	4.5	5.18 ± 0.03	1.00	4.11 ± 0.05	0.94
	5	5.19 ± 0.03	1.00	4.12 ± 0.05	0.94
	6	5.18 ± 0.03	1.00	4.13 ± 0.05	0.90
	7	5.13 ± 0.03	1.00	4.07 ± 0.05	0.80
183	3.5	5.15 ± 0.04	0.78	4.08 ± 0.06	0.93
	4	5.14 ± 0.03	0.73	4.09 ± 0.06	0.94
	4.5	5.15 ± 0.03	0.95	4.09 ± 0.06	0.94
	5	5.16 ± 0.03	0.98	4.09 ± 0.06	0.91
	6	5.16 ± 0.03	1.00	4.11 ± 0.05	0.93
	7	5.12 ± 0.03	1.00	4.07 ± 0.05	0.99
187	3.5	4.92 ± 0.03	1.00	4.10 ± 0.06	0.87
	4	4.92 ± 0.03	1.00	4.10 ± 0.06	0.83
	4.5	4.92 ± 0.03	1.00	4.10 ± 0.06	0.83
	5	4.92 ± 0.03	1.00	4.13 ± 0.06	0.89
	6	4.93 ± 0.03	1.00	4.14 ± 0.05	0.89
	7	4.88 ± 0.03	1.00	4.10 ± 0.06	0.78
191	3.5	5.02 ± 0.03	0.96	4.24 ± 0.07	0.67
	4	5.00 ± 0.03	0.99	4.28 ± 0.07	0.73
	4.5	5.00 ± 0.03	0.99	4.32 ± 0.07	0.95
	5	5.01 ± 0.03	1.00	4.32 ± 0.07	0.97
	6	5.01 ± 0.03	1.00	4.31 ± 0.06	0.96
	7	4.97 ± 0.03	1.00	4.26 ± 0.06	0.92

Table A.2: FWHM and $p(\chi^2/_{\mathrm{NDF}})$ for core and segment 11 at 1408.0 keV, fitted using a Gaussian plus first order polynomial background.

z (mm)	$n \cdot \sigma$	FWHM$_{core}$ (keV)	$p(\chi^2/_{\mathrm{NDF}})_{core}$	FWHM$_{14}$ (keV)	$p(\chi^2/_{\mathrm{NDF}})_{14}$
195	3.5	4.32 ± 0.31	0.98	3.53 ± 0.16	0.98
	4	4.29 ± 0.27	0.96	3.55 ± 0.14	0.95
	4.5	4.24 ± 0.26	0.96	3.52 ± 0.14	0.94
	5	4.20 ± 0.25	0.93	3.51 ± 0.13	0.87
	6	4.12 ± 0.24	0.90	3.50 ± 0.13	0.94
	7	10.64 ± 0.66	1.00	3.44 ± 0.13	0.87
199	3.5	3.98 ± 0.24	1.00	3.31 ± 0.11	0.99
	4	4.06 ± 0.23	0.99	3.38 ± 0.10	0.99
	4.5	4.08 ± 0.22	0.99	3.37 ± 0.10	0.99
	5	4.10 ± 0.21	1.00	3.39 ± 0.10	0.98
	6	4.04 ± 0.20	1.00	3.39 ± 0.09	0.98
	7	3.95 ± 0.20	0.99	3.33 ± 0.09	0.95
203	3.5	4.02 ± 0.24	0.99	3.74 ± 0.12	1.00
	4	4.07 ± 0.23	0.98	3.68 ± 0.11	1.00
	4.5	4.07 ± 0.21	0.97	3.70 ± 0.11	1.00
	5	4.12 ± 0.21	0.96	3.78 ± 0.11	1.00
	6	4.16 ± 0.21	0.90	3.78 ± 0.10	1.00
	7	4.20 ± 0.21	0.94	3.71 ± 0.10	1.00
207	3.5	3.24 ± 0.19	0.95	3.27 ± 0.11	0.98
	4	3.38 ± 0.19	0.96	3.31 ± 0.11	0.98
	4.5	3.40 ± 0.19	0.94	3.27 ± 0.10	0.97
	5	3.42 ± 0.18	0.92	3.28 ± 0.10	0.95
	6	3.35 ± 0.17	0.96	3.32 ± 0.10	0.96
	7	3.24 ± 0.17	0.99	3.24 ± 0.10	0.94
211	3.5	4.25 ± 0.27	1.00	3.96 ± 0.12	0.41
	4	4.19 ± 0.24	1.00	3.94 ± 0.12	0.32
	4.5	4.29 ± 0.25	1.00	3.88 ± 0.11	0.47
	5	4.28 ± 0.24	1.00	3.88 ± 0.11	0.40
	6	4.19 ± 0.22	1.00	3.90 ± 0.10	0.31
	7	4.19 ± 0.22	1.00	3.87 ± 0.10	0.44
215	3.5	4.31 ± 0.29	1.00	3.76 ± 0.17	0.51
	4	4.40 ± 0.28	1.00	3.79 ± 0.17	0.43
	4.5	4.45 ± 0.28	1.00	3.73 ± 0.15	0.38
	5	4.31 ± 0.26	1.00	3.71 ± 0.15	0.48
	6	4.36 ± 0.25	1.00	3.67 ± 0.14	0.42
	7	4.32 ± 0.25	1.00	3.62 ± 0.14	0.36

Table A.3: FWHM and $p(\chi^2/_{\mathrm{NDF}})$ for core and segment 14 at 344.3 keV, fitted using a Gaussian plus first order polynomial background.

z (mm)	$n \cdot \sigma$	FWHM$_{core}$ (keV)	$p(\chi^2/_{\mathrm{NDF}})_{core}$	FWHM$_{14}$ (keV)	$p(\chi^2/_{\mathrm{NDF}})_{14}$
195	3.5	4.97 ± 0.03	0.99	3.96 ± 0.06	0.72
	4	4.97 ± 0.03	0.98	3.97 ± 0.06	0.68
	4.5	4.97 ± 0.03	1.00	3.98 ± 0.05	0.60
	5	4.97 ± 0.03	1.00	3.98 ± 0.05	0.51
	6	4.97 ± 0.03	1.00	4.01 ± 0.05	0.62
	7	4.92 ± 0.03	1.00	3.94 ± 0.05	0.61
199	3.5	4.89 ± 0.03	0.93	3.88 ± 0.06	0.53
	4	4.88 ± 0.03	0.92	3.88 ± 0.05	0.45
	4.5	4.87 ± 0.03	1.00	3.91 ± 0.05	0.72
	5	4.86 ± 0.03	1.00	3.90 ± 0.05	0.68
	6	4.86 ± 0.03	1.00	3.92 ± 0.05	0.84
	7	4.82 ± 0.03	1.00	3.86 ± 0.05	0.77
203	3.5	5.01 ± 0.03	0.91	4.05 ± 0.06	0.99
	4	5.00 ± 0.03	0.92	4.05 ± 0.06	0.99
	4.5	5.00 ± 0.03	0.89	4.05 ± 0.05	0.98
	5	5.00 ± 0.03	0.89	4.06 ± 0.05	0.98
	6	5.00 ± 0.03	0.98	4.06 ± 0.05	0.97
	7	4.95 ± 0.03	1.00	4.00 ± 0.05	0.95
207	3.5	4.39 ± 0.03	0.99	3.97 ± 0.06	0.73
	4	4.37 ± 0.03	1.00	3.97 ± 0.06	0.73
	4.5	4.37 ± 0.02	1.00	4.02 ± 0.05	0.94
	5	4.37 ± 0.02	1.00	4.04 ± 0.05	0.92
	6	4.37 ± 0.02	1.00	4.04 ± 0.05	0.82
	7	4.32 ± 0.02	1.00	3.98 ± 0.05	0.72
211	3.5	4.80 ± 0.03	1.00	4.23 ± 0.06	0.03
	4	4.81 ± 0.03	1.00	4.26 ± 0.05	0.08
	4.5	4.81 ± 0.03	1.00	4.28 ± 0.05	0.11
	5	4.80 ± 0.03	1.00	4.29 ± 0.05	0.11
	6	4.81 ± 0.03	1.00	4.29 ± 0.05	0.08
	7	4.76 ± 0.03	1.00	4.23 ± 0.05	0.03
215	3.5	5.12 ± 0.03	1.00	4.28 ± 0.06	0.22
	4	5.12 ± 0.03	1.00	4.31 ± 0.06	0.22
	4.5	5.10 ± 0.03	1.00	4.31 ± 0.06	0.18
	5	5.09 ± 0.03	1.00	4.31 ± 0.06	0.13
	6	5.08 ± 0.03	1.00	4.34 ± 0.06	0.89
	7	5.04 ± 0.03	1.00	4.28 ± 0.06	0.82

Table A.4: FWHM and $p(\chi^2/_{\mathrm{NDF}})$ for core and segment 14 at 1408.0 keV, fitted using a Gaussian plus first order polynomial background.

z (mm)	$n \cdot \sigma$	FWHM$_{core}$ (keV)	$p(\chi^2/_{\mathrm{NDF}})_{core}$	FWHM$_{17}$ (keV)	$p(\chi^2/_{\mathrm{NDF}})_{17}$
219	3.5	4.22 ± 0.21	1.00	3.93 ± 0.20	0.17
	4	4.19 ± 0.19	1.00	4.03 ± 0.19	0.22
	4.5	4.24 ± 0.19	1.00	4.10 ± 0.18	0.31
	5	4.27 ± 0.18	1.00	4.08 ± 0.18	0.25
	6	4.16 ± 0.17	1.00	4.11 ± 0.17	0.46
	7	4.21 ± 0.18	1.00	4.07 ± 0.17	0.84
223	3.5	3.98 ± 0.17	1.00	3.84 ± 0.14	0.98
	4	3.99 ± 0.16	1.00	3.74 ± 0.13	0.99
	4.5	3.97 ± 0.15	1.00	3.72 ± 0.12	0.98
	5	4.01 ± 0.15	1.00	3.73 ± 0.12	0.98
	6	3.97 ± 0.14	1.00	3.72 ± 0.12	0.95
	7	3.90 ± 0.14	1.00	3.68 ± 0.12	0.94
227	3.5	3.89 ± 0.16	0.90	3.95 ± 0.13	0.12
	4	3.87 ± 0.15	0.86	3.96 ± 0.13	0.08
	4.5	3.89 ± 0.14	0.78	3.95 ± 0.12	0.10
	5	3.86 ± 0.14	0.68	3.96 ± 0.12	0.12
	6	3.88 ± 0.13	0.60	3.93 ± 0.11	0.11
	7	3.86 ± 0.13	0.77	3.87 ± 0.11	0.07
231	3.5	4.22 ± 0.16	0.87	3.92 ± 0.14	0.87
	4	4.24 ± 0.15	0.75	3.80 ± 0.12	0.94
	4.5	4.20 ± 0.14	0.73	3.73 ± 0.11	0.97
	5	4.18 ± 0.14	0.63	3.71 ± 0.11	0.97
	6	4.20 ± 0.13	0.62	3.73 ± 0.11	0.95
	7	4.12 ± 0.13	0.47	3.70 ± 0.11	0.91
235	3.5	4.30 ± 0.16	0.88	3.75 ± 0.14	0.47
	4	4.30 ± 0.15	0.83	3.74 ± 0.13	0.37
	4.5	4.32 ± 0.14	0.73	3.74 ± 0.13	0.28
	5	4.26 ± 0.14	0.75	3.76 ± 0.12	0.46
	6	4.29 ± 0.13	0.77	3.79 ± 0.12	0.50
	7	4.16 ± 0.13	1.00	3.75 ± 0.12	0.74
239	3.5	3.55 ± 0.16	0.82	3.73 ± 0.22	0.88
	4	3.62 ± 0.16	0.87	3.74 ± 0.20	0.83
	4.5	3.66 ± 0.16	0.91	3.72 ± 0.20	0.77
	5	3.63 ± 0.15	0.90	3.78 ± 0.20	0.77
	6	3.63 ± 0.14	0.88	3.77 ± 0.19	0.91
	7	3.61 ± 0.15	1.00	3.70 ± 0.19	0.94

Table A.5: FWHM and $p(\chi^2/_{\mathrm{NDF}})$ for core and segment 17 at 344.3 keV, fitted using a Gaussian plus first order polynomial background.

z (mm)	$n \cdot \sigma$	FWHM$_{core}$ (keV)	$p(\chi^2/_{\mathrm{NDF}})_{core}$	FWHM$_{17}$ (keV)	$p(\chi^2/_{\mathrm{NDF}})_{17}$
219	3.5	4.69 ± 0.03	1.00	4.30 ± 0.07	0.90
	4	4.67 ± 0.03	1.00	4.33 ± 0.07	0.88
	4.5	4.66 ± 0.03	1.00	4.36 ± 0.06	0.88
	5	4.65 ± 0.02	1.00	4.38 ± 0.06	0.94
	6	4.66 ± 0.02	1.00	4.39 ± 0.06	0.94
	7	4.61 ± 0.02	1.00	4.34 ± 0.06	0.89
223	3.5	4.66 ± 0.03	1.00	3.88 ± 0.07	0.98
	4	4.65 ± 0.03	1.00	3.88 ± 0.06	0.95
	4.5	4.64 ± 0.03	1.00	3.88 ± 0.05	0.93
	5	4.64 ± 0.02	1.00	3.89 ± 0.05	0.94
	6	4.64 ± 0.02	1.00	3.89 ± 0.05	0.95
	7	4.59 ± 0.02	1.00	3.82 ± 0.05	0.98
227	3.5	4.65 ± 0.03	0.94	4.23 ± 0.06	0.74
	4	4.62 ± 0.03	1.00	4.24 ± 0.06	0.65
	4.5	4.62 ± 0.03	1.00	4.25 ± 0.06	0.49
	5	4.63 ± 0.03	1.00	4.26 ± 0.05	0.46
	6	4.63 ± 0.02	1.00	4.25 ± 0.05	0.45
	7	4.58 ± 0.02	1.00	4.23 ± 0.05	0.94
231	3.5	4.73 ± 0.03	1.00	4.07 ± 0.06	0.33
	4	4.72 ± 0.03	1.00	4.07 ± 0.06	0.33
	4.5	4.71 ± 0.02	1.00	4.08 ± 0.05	0.19
	5	4.71 ± 0.02	1.00	4.09 ± 0.05	0.49
	6	4.71 ± 0.02	1.00	4.09 ± 0.05	0.42
	7	4.66 ± 0.02	1.00	4.04 ± 0.05	0.47
235	3.5	4.66 ± 0.03	1.00	4.02 ± 0.06	0.99
	4	4.68 ± 0.03	1.00	4.02 ± 0.06	0.99
	4.5	4.67 ± 0.03	1.00	4.02 ± 0.05	0.98
	5	4.66 ± 0.03	1.00	4.01 ± 0.05	0.96
	6	4.65 ± 0.03	1.00	4.03 ± 0.05	0.94
	7	4.62 ± 0.03	1.00	3.98 ± 0.05	0.95
239	3.5	4.70 ± 0.03	1.00	4.04 ± 0.06	0.94
	4	4.69 ± 0.03	1.00	4.04 ± 0.06	0.94
	4.5	4.69 ± 0.03	1.00	4.04 ± 0.06	0.88
	5	4.69 ± 0.03	1.00	4.04 ± 0.06	0.85
	6	4.70 ± 0.02	1.00	4.06 ± 0.06	0.88
	7	4.65 ± 0.03	1.00	4.00 ± 0.06	0.80

Table A.6: FWHM and $p(\chi^2/_{\mathrm{NDF}})$ for core and segment 17 at 1408.0 keV, fitted using a Gaussian plus first order polynomial background.

z (mm)	$n \cdot \sigma$	FWHM$_{core}$ (keV)	$p(\chi^2/_{\mathrm{NDF}})_{core}$	FWHM$_{11}$ (keV)	$p(\chi^2/_{\mathrm{NDF}})_{11}$
171	3.5	4.75 ± 0.32	0.98	3.50 ± 0.18	0.36
	4	5.42 ± 0.63	1.00	3.59 ± 0.16	0.61
	4.5	5.04 ± 0.27	1.00	3.50 ± 0.16	0.78
	5	4.79 ± 0.26	1.00	3.34 ± 0.15	0.62
	6	4.80 ± 0.25	0.98	3.37 ± 0.15	0.86
	7	4.56 ± 0.25	0.97	3.44 ± 0.15	0.93
175	3.5	3.85 ± 0.22	1.00	3.91 ± 0.13	0.96
	4	3.94 ± 0.22	1.00	3.69 ± 0.12	0.97
	4.5	3.90 ± 0.20	0.99	3.67 ± 0.12	0.96
	5	3.89 ± 0.20	0.99	3.69 ± 0.11	0.96
	6	3.65 ± 0.19	1.00	3.70 ± 0.11	0.88
	7	3.85 ± 0.19	1.00	3.63 ± 0.11	0.87
179	3.5	4.56 ± 0.23	1.00	3.85 ± 0.13	0.99
	4	4.45 ± 0.22	1.00	3.75 ± 0.12	1.00
	4.5	4.44 ± 0.21	1.00	3.75 ± 0.12	1.00
	5	4.41 ± 0.20	1.00	3.79 ± 0.12	1.00
	6	4.26 ± 0.19	1.00	4.00 ± 0.12	1.00
	7	4.26 ± 0.22	1.00	3.88 ± 0.12	1.00
183	3.5	4.02 ± 0.21	0.98	3.83 ± 0.12	0.99
	4	3.89 ± 0.19	0.96	4.04 ± 0.11	1.00
	4.5	4.27 ± 0.18	0.99	3.73 ± 0.10	1.00
	5	4.31 ± 0.17	0.99	3.83 ± 0.10	0.98
	6	3.95 ± 0.16	1.00	3.71 ± 0.10	0.98
	7	3.92 ± 0.16	1.00	3.68 ± 0.10	0.99
187	3.5	4.05 ± 0.24	0.97	3.56 ± 0.13	0.93
	4	3.66 ± 0.31	0.85	3.46 ± 0.12	0.85
	4.5	3.67 ± 0.21	0.79	3.45 ± 0.12	0.78
	5	3.81 ± 0.21	0.75	3.66 ± 0.12	0.87
	6	3.96 ± 0.21	0.83	3.55 ± 0.11	0.82
	7	4.12 ± 0.21	0.84	3.57 ± 0.11	0.75
191	3.5	4.23 ± 0.36	0.94	3.79 ± 0.21	0.95
	4	3.90 ± 0.34	0.91	3.52 ± 0.19	0.89
	4.5	4.23 ± 0.34	0.94	3.54 ± 0.18	0.79
	5	4.97 ± 0.37	1.00	3.48 ± 0.18	0.88
	6	4.41 ± 0.33	1.00	3.50 ± 0.17	0.75
	7	16.69 ± 22.30	1.00	3.38 ± 0.17	0.69

Table A.7: FWHM and $p(\chi^2/_{\mathrm{NDF}})$ for core and segment 11 at 344.3 keV, fitted using a Gaussian plus cubic background.

z (mm)	$n \cdot \sigma$	FWHM$_{core}$ (keV)	$p(\chi^2/_{\mathrm{NDF}})_{core}$	FWHM$_{11}$ (keV)	$p(\chi^2/_{\mathrm{NDF}})_{11}$
171	3.5	5.13 ± 0.04	1.00	4.13 ± 0.06	0.83
	4	5.12 ± 0.03	1.00	4.13 ± 0.06	0.68
	4.5	5.13 ± 0.03	1.00	4.13 ± 0.06	0.68
	5	5.13 ± 0.03	1.00	4.14 ± 0.06	0.55
	6	5.12 ± 0.03	1.00	4.14 ± 0.06	0.38
	7	5.11 ± 0.03	1.00	4.09 ± 0.06	0.31
175	3.5	5.13 ± 0.04	1.00	4.01 ± 0.07	0.94
	4	5.10 ± 0.03	1.00	3.96 ± 0.05	0.99
	4.5	5.09 ± 0.03	1.00	3.98 ± 0.05	1.00
	5	5.09 ± 0.03	1.00	3.99 ± 0.05	1.00
	6	5.09 ± 0.03	1.00	3.99 ± 0.05	1.00
	7	5.05 ± 0.03	1.00	3.93 ± 0.05	1.00
179	3.5	5.22 ± 0.04	0.99	4.09 ± 0.06	0.97
	4	5.20 ± 0.03	1.00	4.11 ± 0.06	0.98
	4.5	5.18 ± 0.03	1.00	4.11 ± 0.06	0.98
	5	5.18 ± 0.03	1.00	4.12 ± 0.05	0.97
	6	5.18 ± 0.03	1.00	4.13 ± 0.05	0.95
	7	5.13 ± 0.03	1.00	4.07 ± 0.05	0.88
183	3.5	5.15 ± 0.04	0.89	4.08 ± 0.06	0.97
	4	5.14 ± 0.03	0.85	4.09 ± 0.06	0.98
	4.5	5.15 ± 0.03	0.98	4.09 ± 0.06	0.98
	5	5.16 ± 0.03	0.99	4.09 ± 0.06	0.96
	6	5.16 ± 0.03	1.00	4.11 ± 0.05	0.97
	7	5.12 ± 0.03	1.00	4.07 ± 0.05	1.00
187	3.5	4.92 ± 0.03	1.00	4.10 ± 0.06	0.94
	4	4.92 ± 0.03	1.00	4.10 ± 0.06	0.92
	4.5	4.92 ± 0.03	1.00	4.10 ± 0.06	0.92
	5	4.92 ± 0.03	1.00	4.13 ± 0.06	0.95
	6	4.93 ± 0.03	1.00	4.08 ± 0.05	0.77
	7	4.88 ± 0.03	1.00	4.09 ± 0.06	0.86
191	3.5	5.02 ± 0.03	0.99	4.24 ± 0.07	0.82
	4	5.00 ± 0.03	1.00	4.28 ± 0.07	0.85
	4.5	5.00 ± 0.03	1.00	4.15 ± 0.07	0.49
	5	5.01 ± 0.03	1.00	4.32 ± 0.07	0.99
	6	5.01 ± 0.03	1.00	4.31 ± 0.06	0.98
	7	4.97 ± 0.03	1.00	4.26 ± 0.06	0.96

Table A.8: FWHM and $p(\chi^2/_{\mathrm{NDF}})$ for core and segment 11 at 1408.0 keV, fitted using a Gaussian plus cubic background.

z (mm)	$n \cdot \sigma$	FWHM$_{core}$ (keV)	$p(\chi^2/_{\mathrm{NDF}})_{core}$	FWHM$_{14}$ (keV)	$p(\chi^2/_{\mathrm{NDF}})_{14}$
195	3.5	4.31 ± 0.31	0.99	3.53 ± 0.16	0.99
	4	4.28 ± 0.28	0.99	3.44 ± 0.14	0.98
	4.5	4.24 ± 0.26	0.98	3.52 ± 0.14	0.98
	5	4.42 ± 0.25	0.96	3.55 ± 0.13	0.94
	6	4.43 ± 0.25	0.89	3.55 ± 0.13	0.97
	7	4.17 ± 0.28	0.82	3.44 ± 0.12	0.93
199	3.5	3.98 ± 0.24	1.00	3.31 ± 0.11	1.00
	4	4.05 ± 0.22	1.00	3.38 ± 0.10	1.00
	4.5	3.73 ± 0.21	0.99	3.37 ± 0.10	1.00
	5	3.83 ± 0.20	1.00	3.27 ± 0.09	0.99
	6	4.03 ± 0.20	1.00	3.38 ± 0.09	0.99
	7	4.00 ± 0.20	0.99	3.28 ± 0.09	0.97
203	3.5	3.55 ± 0.23	0.99	3.37 ± 0.12	1.00
	4	4.06 ± 0.22	0.99	3.67 ± 0.11	1.00
	4.5	4.06 ± 0.21	0.99	3.70 ± 0.11	1.00
	5	4.11 ± 0.21	0.98	3.59 ± 0.10	1.00
	6	4.00 ± 0.20	0.93	3.67 ± 0.10	1.00
	7	3.89 ± 0.20	0.88	3.66 ± 0.10	1.00
207	3.5	3.24 ± 0.19	0.99	3.03 ± 0.11	0.99
	4	3.37 ± 0.19	0.99	3.08 ± 0.11	0.98
	4.5	3.40 ± 0.19	0.98	3.24 ± 0.10	0.99
	5	3.42 ± 0.21	0.97	3.28 ± 0.10	0.98
	6	3.44 ± 0.17	0.98	3.21 ± 0.10	0.96
	7	3.38 ± 0.17	0.99	3.22 ± 0.10	0.97
211	3.5	4.24 ± 0.27	1.00	4.14 ± 0.12	0.50
	4	4.18 ± 0.25	1.00	3.94 ± 0.12	0.53
	4.5	3.82 ± 0.23	1.00	4.12 ± 0.11	0.23
	5	3.92 ± 0.22	1.00	3.99 ± 0.11	0.43
	6	4.34 ± 0.22	1.00	3.92 ± 0.10	0.45
	7	4.11 ± 0.22	1.00	3.80 ± 0.10	0.47
215	3.5	4.31 ± 0.29	1.00	3.76 ± 0.17	0.73
	4	4.39 ± 0.28	1.00	3.78 ± 0.17	0.65
	4.5	4.22 ± 0.27	1.00	3.87 ± 0.16	0.51
	5	4.72 ± 0.27	1.00	3.70 ± 0.15	0.65
	6	4.19 ± 0.24	1.00	3.81 ± 0.14	0.42
	7	4.30 ± 0.25	1.00	3.64 ± 0.14	0.50

Table A.9: FWHM and $p(\chi^2/_{\mathrm{NDF}})$ for core and segment 14 at 344.3 keV, fitted using a Gaussian plus cubic background.

z (mm)	$n \cdot \sigma$	FWHM$_{core}$ (keV)	$p(\chi^2/_{\mathrm{NDF}})_{core}$	FWHM$_{14}$ (keV)	$p(\chi^2/_{\mathrm{NDF}})_{14}$
195	3.5	4.97 ± 0.03	1.00	3.96 ± 0.06	0.87
	4	4.97 ± 0.03	0.99	3.97 ± 0.06	0.83
	4.5	4.97 ± 0.03	1.00	3.98 ± 0.05	0.76
	5	4.97 ± 0.03	1.00	3.98 ± 0.05	0.69
	6	4.97 ± 0.03	1.00	4.01 ± 0.05	0.76
	7	4.92 ± 0.03	1.00	3.94 ± 0.05	0.74
199	3.5	4.89 ± 0.03	0.97	3.88 ± 0.06	0.75
	4	4.88 ± 0.03	0.96	3.88 ± 0.05	0.65
	4.5	4.87 ± 0.03	1.00	3.91 ± 0.05	0.85
	5	4.86 ± 0.03	1.00	3.90 ± 0.05	0.82
	6	4.86 ± 0.03	1.00	3.92 ± 0.05	0.91
	7	4.82 ± 0.03	1.00	3.86 ± 0.05	0.86
203	3.5	5.01 ± 0.03	0.96	4.05 ± 0.06	1.00
	4	5.00 ± 0.03	0.96	4.05 ± 0.06	1.00
	4.5	5.00 ± 0.03	0.94	4.05 ± 0.05	0.99
	5	5.00 ± 0.03	0.94	4.06 ± 0.05	0.99
	6	5.00 ± 0.03	0.99	4.06 ± 0.05	0.99
	7	4.95 ± 0.03	1.00	4.00 ± 0.05	0.98
207	3.5	4.39 ± 0.03	1.00	3.97 ± 0.05	0.86
	4	4.37 ± 0.03	1.00	3.97 ± 0.05	0.86
	4.5	4.37 ± 0.02	1.00	4.02 ± 0.05	0.98
	5	4.37 ± 0.02	1.00	4.04 ± 0.05	0.96
	6	4.37 ± 0.02	1.00	4.04 ± 0.05	0.90
	7	4.32 ± 0.02	1.00	3.98 ± 0.05	0.82
211	3.5	4.80 ± 0.03	1.00	4.23 ± 0.06	0.10
	4	4.81 ± 0.03	1.00	4.26 ± 0.05	0.19
	4.5	4.80 ± 0.03	1.00	4.28 ± 0.05	0.22
	5	4.80 ± 0.03	1.00	4.29 ± 0.05	0.22
	6	4.80 ± 0.03	1.00	4.29 ± 0.05	0.15
	7	4.76 ± 0.03	1.00	4.23 ± 0.05	0.07
215	3.5	5.12 ± 0.03	1.00	4.28 ± 0.06	0.41
	4	5.12 ± 0.03	1.00	4.31 ± 0.06	0.38
	4.5	5.10 ± 0.03	1.00	4.31 ± 0.06	0.32
	5	5.09 ± 0.03	1.00	4.31 ± 0.06	0.25
	6	5.08 ± 0.03	1.00	4.34 ± 0.06	0.94
	7	5.04 ± 0.03	1.00	4.28 ± 0.06	0.89

Table A.10: FWHM and $p(\chi^2/_{\mathrm{NDF}})$ for core and segment 14 at 1408.0 keV, fitted using a Gaussian plus cubic background.

z (mm)	$n \cdot \sigma$	FWHM$_{core}$ (keV)	$p(\chi^2/_{\mathrm{NDF}})_{core}$	FWHM$_{17}$ (keV)	$p(\chi^2/_{\mathrm{NDF}})_{17}$
219	3.5	7.05 ± 0.22	0.97	3.93 ± 0.20	0.36
	4	4.71 ± 0.34	1.00	4.03 ± 0.19	0.39
	4.5	4.35 ± 0.19	1.00	4.10 ± 0.18	0.48
	5	4.26 ± 0.18	1.00	4.08 ± 0.18	0.40
	6	4.44 ± 0.18	1.00	4.00 ± 0.17	0.54
	7	4.10 ± 0.17	1.00	3.93 ± 0.20	0.86
223	3.5	4.67 ± 0.17	1.00	3.84 ± 0.14	0.99
	4	3.99 ± 0.16	1.00	3.91 ± 0.13	1.00
	4.5	4.15 ± 0.15	1.00	3.72 ± 0.12	0.99
	5	4.00 ± 0.15	1.00	3.74 ± 0.12	0.99
	6	4.06 ± 0.14	1.00	3.74 ± 0.11	0.98
	7	3.98 ± 0.14	1.00	3.54 ± 0.11	0.98
227	3.5	3.89 ± 0.16	0.96	3.95 ± 0.13	0.29
	4	3.87 ± 0.15	0.94	3.96 ± 0.13	0.20
	4.5	3.85 ± 0.14	0.88	3.95 ± 0.12	0.22
	5	3.86 ± 0.14	0.81	3.96 ± 0.12	0.24
	6	3.88 ± 0.13	0.72	3.99 ± 0.11	0.16
	7	3.73 ± 0.13	0.73	3.91 ± 0.11	0.12
231	3.5	4.22 ± 0.16	0.95	3.74 ± 0.14	0.94
	4	4.24 ± 0.15	0.87	4.11 ± 0.12	0.94
	4.5	4.40 ± 0.14	0.76	4.05 ± 0.11	0.89
	5	4.35 ± 0.14	0.64	3.97 ± 0.11	0.89
	6	4.25 ± 0.13	0.73	3.73 ± 0.11	0.98
	7	4.18 ± 0.13	0.56	3.66 ± 0.11	0.94
235	3.5	4.30 ± 0.15	0.95	3.75 ± 0.14	0.70
	4	4.29 ± 0.15	0.92	3.74 ± 0.13	0.58
	4.5	4.32 ± 0.14	0.84	3.74 ± 0.13	0.47
	5	4.37 ± 0.14	0.83	3.76 ± 0.12	0.63
	6	4.22 ± 0.13	0.84	3.69 ± 0.12	0.55
	7	4.33 ± 0.13	1.00	3.64 ± 0.12	0.73
239	3.5	3.55 ± 0.16	0.93	3.73 ± 0.22	0.96
	4	3.61 ± 0.16	0.95	3.74 ± 0.20	0.92
	4.5	3.46 ± 0.15	0.93	3.72 ± 0.20	0.89
	5	3.63 ± 0.15	0.95	3.78 ± 0.20	0.87
	6	3.62 ± 0.15	0.93	3.73 ± 0.19	0.95
	7	3.50 ± 0.14	1.00	3.70 ± 0.19	0.97

Table A.11: FWHM and $p(\chi^2/_{\mathrm{NDF}})$ for core and segment 17 at 344.3 keV, fitted using a Gaussian plus cubic background.

z (mm)	$n \cdot \sigma$	FWHM$_{core}$ (keV)	$p(\chi^2/_{\mathrm{NDF}})_{core}$	FWHM$_{17}$ (keV)	$p(\chi^2/_{\mathrm{NDF}})_{17}$
219	3.5	4.69 ± 0.03	1.00	4.30 ± 0.07	0.96
	4	4.67 ± 0.03	1.00	4.33 ± 0.07	0.94
	4.5	4.66 ± 0.03	1.00	4.36 ± 0.06	0.94
	5	4.65 ± 0.02	1.00	4.38 ± 0.06	0.97
	6	4.66 ± 0.02	1.00	4.31 ± 0.06	0.85
	7	4.61 ± 0.02	1.00	4.34 ± 0.06	0.94
223	3.5	4.66 ± 0.03	1.00	3.88 ± 0.07	0.99
	4	4.65 ± 0.03	1.00	3.88 ± 0.05	0.98
	4.5	4.64 ± 0.03	1.00	3.88 ± 0.05	0.97
	5	4.64 ± 0.02	1.00	3.89 ± 0.05	0.97
	6	4.64 ± 0.02	1.00	3.89 ± 0.05	0.98
	7	4.59 ± 0.02	1.00	3.82 ± 0.05	0.99
227	3.5	4.65 ± 0.03	0.98	4.23 ± 0.06	0.87
	4	4.62 ± 0.03	1.00	4.24 ± 0.06	0.80
	4.5	4.62 ± 0.03	1.00	4.25 ± 0.06	0.65
	5	4.63 ± 0.03	1.00	4.26 ± 0.05	0.61
	6	4.63 ± 0.02	1.00	4.25 ± 0.05	0.60
	7	4.58 ± 0.02	1.00	4.23 ± 0.05	0.97
231	3.5	4.73 ± 0.03	1.00	4.07 ± 0.06	0.54
	4	4.72 ± 0.03	1.00	4.07 ± 0.06	0.54
	4.5	4.71 ± 0.03	1.00	4.08 ± 0.05	0.35
	5	4.71 ± 0.02	1.00	4.09 ± 0.05	0.66
	6	4.71 ± 0.02	1.00	4.09 ± 0.05	0.57
	7	4.66 ± 0.02	1.00	4.04 ± 0.05	0.61
235	3.5	4.66 ± 0.03	1.00	4.02 ± 0.06	1.00
	4	4.68 ± 0.03	1.00	4.02 ± 0.06	1.00
	4.5	4.67 ± 0.03	1.00	4.02 ± 0.05	0.99
	5	4.66 ± 0.03	1.00	4.01 ± 0.05	0.98
	6	4.65 ± 0.03	1.00	4.03 ± 0.05	0.97
	7	4.62 ± 0.03	1.00	3.98 ± 0.05	0.97
239	3.5	4.70 ± 0.03	1.00	4.04 ± 0.07	0.98
	4	4.69 ± 0.03	1.00	4.04 ± 0.06	0.98
	4.5	4.69 ± 0.03	1.00	4.04 ± 0.06	0.95
	5	4.69 ± 0.03	1.00	4.04 ± 0.06	0.93
	6	4.70 ± 0.03	1.00	4.06 ± 0.06	0.94
	7	4.65 ± 0.03	1.00	4.00 ± 0.06	0.88

Table A.12: FWHM and $p(\chi^2/_{\mathrm{NDF}})$ for core and segment 17 at 1408.0 keV, fitted using a Gaussian plus cubic background.

energy (keV)	$n_{BG}\cdot\sigma$	$n_{peak}\cdot\sigma$	FWHM_{core}	FWHM_{11}	FWHM_{14}	FWHM_{17}
344.3	6.0	2.5	3.67 ± 0.31	3.24 ± 0.19	3.03 ± 0.29	3.41 ± 0.15
		3.0	3.67 ± 0.38	3.19 ± 0.17	3.25 ± 0.32	3.49 ± 0.09
		3.5	3.75 ± 0.37	3.35 ± 0.16	3.37 ± 0.30	3.56 ± 0.06
		4.0	3.89 ± 0.34	3.41 ± 0.16	3.28 ± 0.29	3.52 ± 0.13
	7.0	2.5	3.64 ± 0.29	3.24 ± 0.20	3.04 ± 0.29	3.42 ± 0.14
		3.0	3.65 ± 0.34	3.19 ± 0.18	3.25 ± 0.32	3.45 ± 0.09
		3.5	3.72 ± 0.33	3.36 ± 0.16	3.36 ± 0.30	3.57 ± 0.06
		4.0	3.87 ± 0.33	3.41 ± 0.17	3.27 ± 0.29	3.61 ± 0.22
	8.0	2.5	3.64 ± 0.25	3.25 ± 0.20	3.04 ± 0.30	3.40 ± 0.12
		3.0	3.64 ± 0.33	3.20 ± 0.18	3.25 ± 0.32	3.44 ± 0.09
		3.5	3.74 ± 0.31	3.36 ± 0.16	3.36 ± 0.30	3.56 ± 0.07
		4.0	3.84 ± 0.31	3.41 ± 0.16	3.27 ± 0.29	3.60 ± 0.22
1408.0	6.0	2.5	4.48 ± 0.25	3.70 ± 0.12	3.51 ± 0.24	3.65 ± 0.15
		3.0	4.57 ± 0.28	3.74 ± 0.10	3.69 ± 0.19	3.80 ± 0.15
		3.5	4.62 ± 0.26	3.85 ± 0.09	3.78 ± 0.10	3.77 ± 0.18
		4.0	4.63 ± 0.25	3.87 ± 0.18	3.85 ± 0.10	3.81 ± 0.24
	7.0	2.5	4.48 ± 0.25	3.70 ± 0.12	3.51 ± 0.24	3.66 ± 0.15
		3.0	4.57 ± 0.28	3.74 ± 0.11	3.69 ± 0.19	3.80 ± 0.15
		3.5	4.63 ± 0.26	3.85 ± 0.09	3.79 ± 0.10	3.77 ± 0.18
		4.0	4.63 ± 0.25	3.87 ± 0.18	3.82 ± 0.11	3.81 ± 0.24
	8.0	2.5	4.48 ± 0.25	3.70 ± 0.12	3.51 ± 0.24	3.66 ± 0.15
		3.0	4.57 ± 0.28	3.74 ± 0.11	3.69 ± 0.19	3.80 ± 0.15
		3.5	4.59 ± 0.27	3.85 ± 0.09	3.79 ± 0.10	3.77 ± 0.18
		4.0	4.64 ± 0.25	3.87 ± 0.18	3.82 ± 0.11	3.81 ± 0.24

Table A.13: Average FWHM for core and segments of interest, fitted using a Gaussian plus first order polynomial background, with different fit windows for peak and background.

energy (keV)	$n_{BG}\cdot\sigma$	$n_{peak}\cdot\sigma$	$p(\chi^2/\mathrm{NDF})_{core}$	$p(\chi^2/\mathrm{NDF})_{11}$	$p(\chi^2/\mathrm{NDF})_{14}$	$p(\chi^2/\mathrm{NDF})_{17}$
344.3	6.0	2.5	0.90 ± 0.20	0.90 ± 0.13	0.79 ± 0.29	0.71 ± 0.24
		3.0	0.91 ± 0.20	0.84 ± 0.22	0.83 ± 0.25	0.67 ± 0.31
		3.5	0.97 ± 0.04	0.83 ± 0.24	0.85 ± 0.20	0.62 ± 0.32
		4.0	0.96 ± 0.06	0.85 ± 0.18	0.78 ± 0.29	0.61 ± 0.34
	7.0	2.5	0.93 ± 0.17	0.91 ± 0.12	0.79 ± 0.29	0.72 ± 0.24
		3.0	0.91 ± 0.20	0.87 ± 0.17	0.83 ± 0.25	0.67 ± 0.30
		3.5	0.97 ± 0.04	0.84 ± 0.23	0.84 ± 0.21	0.62 ± 0.32
		4.0	0.96 ± 0.07	0.85 ± 0.18	0.77 ± 0.29	0.61 ± 0.34
	8.0	2.5	0.93 ± 0.17	0.91 ± 0.12	0.79 ± 0.29	0.71 ± 0.24
		3.0	0.91 ± 0.20	0.85 ± 0.20	0.83 ± 0.25	0.66 ± 0.31
		3.5	0.97 ± 0.04	0.83 ± 0.21	0.84 ± 0.21	0.62 ± 0.32
		4.0	0.96 ± 0.06	0.84 ± 0.18	0.77 ± 0.30	0.60 ± 0.35
1408.0	6.0	2.5	0.97 ± 0.08	0.86 ± 0.08	0.67 ± 0.30	0.62 ± 0.28
		3.0	1.00 ± 0.01	0.86 ± 0.11	0.69 ± 0.28	0.79 ± 0.23
		3.5	1.00 ± 0.01	0.90 ± 0.12	0.64 ± 0.31	0.80 ± 0.24
		4.0	1.00 ± 0.01	0.88 ± 0.14	0.65 ± 0.28	0.83 ± 0.22
	7.0	2.5	0.98 ± 0.07	0.86 ± 0.08	0.67 ± 0.30	0.62 ± 0.28
		3.0	1.00 ± 0.01	0.86 ± 0.11	0.70 ± 0.27	0.80 ± 0.23
		3.5	1.00 ± 0.01	0.90 ± 0.12	0.66 ± 0.30	0.80 ± 0.24
		4.0	1.00 ± 0.01	0.89 ± 0.14	0.67 ± 0.26	0.85 ± 0.20
	8.0	2.5	0.98 ± 0.07	0.86 ± 0.08	0.67 ± 0.30	0.62 ± 0.28
		3.0	1.00 ± 0.01	0.86 ± 0.11	0.70 ± 0.27	0.80 ± 0.23
		3.5	1.00 ± 0.01	0.91 ± 0.12	0.67 ± 0.30	0.80 ± 0.24
		4.0	1.00 ± 0.01	0.89 ± 0.13	0.68 ± 0.26	0.85 ± 0.19

Table A.14: Average $p(\chi^2/\mathrm{NDF})$ for the fit with a Gaussian plus first order polynomial background, with different fit windows for peak and background.

Bibliography

[Aal02] C. E. Aalseth et al., *IGEX ^{76}Ge neutrinoless double-beta decay experiment: Prospects for next generation experiments*, Phys. Rev. D **65** (2002), no. 9, 092007.

[Aal05] C. E. Aalseth et al., *The proposed Majorana ^{76}Ge double-beta decay experiment*, Nuclear Physics B - Proceedings Supplements **138** (2005), 217 – 220, Proceedings of the Eighth International Workshop on Topics in Astroparticle and Undeground Physics.

[Abd99] J. N. Abdurashitov et al., *Measurement of the solar neutrino capture rate with gallium metal*, Phys. Rev. C **60** (1999), no. 5, 055801.

[Abt04] I. Abt et al., *A New ^{76}Ge Double Beta Decay Experiment at LNGS*, [arXiv:hep-ex/0404039] (2004).

[Abt07] I. Abt et al., *Characterization of the first true coaxial 18-fold segmented n-type prototype HPGe detector for the GERDA project*, Nuclear Instruments and Methods in Physics Research Section A: Accelerators, Spectrometers, Detectors and Associated Equipment **577** (2007), 574 – 584.

[Abt09] I. Abt et al., *Operation of an 18-fold segmented n-type HPGe detector in liquid nitrogen*, Journal of Instrumentation **4** (2009), P11008.

[Ago03] S. Agostinelli et al., *GEANT4: A simulation toolkit*, Nucl. Instrum. Meth. **A506** (2003), 250–303.

[Alb04] W. M. Alberico and S. M. Bilenky, *Neutrino oscillations, masses and mixing*, Phys. Part. Nucl. **35** (2004), 297–323.

[Alt05] M. Altmann et al., *Complete results for five years of GNO solar neutrino observations*, Physics Letters B **616** (2005), no. 3-4, 174 – 190.

[Ams08] C. Amsler et al., *Review of particle physics*, Phys. Lett. **B667** (2008), 1.

[Arn08] C. Arnaboldi et al., *Results from a search for the* $0\,\nu\beta\beta$*-decay of* ^{130}Te, Phys. Rev. C **78** (2008), no. 3, 035502.

[Arp92] C. Arpesella, *Background measurements at Gran Sasso Laboratory*, Nuclear Physics B - Proceedings Supplements **28** (1992), no. 1, 420 – 424.

[Bar89] R. J. Barlow, *Statistics: A Guide to the Use of Statistical Methods in the Physical Sciences*, reprint ed., Wiley-Blackwell, 7 1989.

[Bar10] A. S. Barabash, V. B. Brudanin, and the NEMO Collaboration, *Investigation of double beta decay with the NEMO-3 detector*, [arXiv:1002.2862v1] (2010).

[Bel95] A. I. Belesev et al., *Results of the Troitsk experiment on the search for the electron antineutrino rest mass in tritium beta-decay*, Physics Letters B **350** (1995), no. 2, 263 – 272.

[Ber] M. J. Berger et al., *XCOM: Photon Cross Sections Database*, http://www.nist.gov/xcom (2010, August 05), National Institute of Standards and Technology (NIST), Gaithersburg, Maryland.

[Blo07] T. Bloxham et al., *First results on double beta-decay modes of Cd, Te, and Zn Isotopes*, Phys. Rev. C **76** (2007), no. 2, 025501.

[Bon05] L. Bonolis, *Bruno Pontecorvo: From slow neutrons to oscillating neutrinos*, American Journal of Physics **73** (2005), no. 6, 487–499.

[Bra03] C. H. Brase and C. P. Brase, *Understanding basic statistics*, 3 ed., Brooks Cole, 2 2003.

[Cha08] Y.-D. Chan et al., *MaGe - a Geant4-based Monte Carlo framework for low-background experiments*, [arXiv:0802.0860v] (2008).

[Cow56] C. L. Cowan et al., *Detection of the free neutrino: A Confirmation*, Science **124** (1956), 103–104.

[Dav55] R. Davis, Jr., *Attempt to Detect the Antineutrinos from a Nuclear Reactor by the* $Cl37(\overline{\nu}, e^-)A37$ *Reaction*, Phys. Rev. **97** (1955), no. 3, 766–769.

[Dav68] R. Davis, Jr., D. S. Harmer, and K. C. Hoffman, *Search for neutrinos from the sun*, Phys. Rev. Lett. **20** (1968), 1205–1209.

[Dav03] R. Davis, Jr., *Nobel Lecture: A half-century with solar neutrinos*, Rev. Mod. Phys. **75** (2003), no. 3, 985–994.

[Dol09] M. J. Dolinski and the EXO Collaboration, *The Enriched Xenon Observatory*, AIP Conference Proceedings **1182** (2009), no. 1, 92–95.

[Dor08] U. Dore and D. Orestano, *Experimental results on neutrino oscillations*, Reports on Progress in Physics **71** (2008), no. 10, 106201.

[Ebe08] J. Eberth and J. Simpson, *From Ge(Li) detectors to gamma-ray tracking arrays - 50 years of gamma spectroscopy with germanium detectors*, Progress in Particle and Nuclear Physics **60** (2008), 283 – 337.

[Egu03] K. Eguchi et al., *First Results from KamLAND: Evidence for Reactor Antineutrino Disappearance*, Phys. Rev. Lett. **90** (2003), no. 2, 021802.

[Ell02] S. R. Elliott and R. Vogel, *Double Beta Decay*, Annual Review of Nuclear and Particle Science **52** (2002), no. 1, 115–151.

[Giu07] C. Giunti, *Neutrino flavour states and the quantum theory of neutrino oscillations*, Journal of Physics G: Nuclear and Particle Physics **34** (2007), no. 2, R93.

[Gol58] M. Goldhaber, L. Grodzins, and A. W. Sunyar, *Helicity of Neutrinos*, Phys. Rev. **109** (1958), no. 3, 1015–1017.

[Gri69] V. Gribov and B. Pontecorvo, *Neutrino astronomy and lepton charge*, Physics Letters B **28** (1969), no. 7, 493 – 496.

[Gru08] C. Grupen and B. Shwartz, *Particle Detectors*, 2nd edition ed., Cambridge University Press, 2008.

[Gut90] D. Gutknecht, *Photomask technique for fabricating high purity germanium strip detectors*, Nuclear Instruments and Methods in Physics Research Section A: Accelerators, Spectrometers, Detectors and Associated Equipment **288** (1990), 13 – 18.

[Ham99] W. Hampel et al., *GALLEX solar neutrino observations: results for GALLEX IV*, Physics Letters B **447** (1999), no. 1-2, 127 – 133.

[Han95] S. Hannestad and J. Madsen, *Neutrino decoupling in the early Universe*, Phys. Rev. D **52** (1995), no. 4, 1764–1769.

[Jun01] C. K. Jung et al., *Oscillations of Atmospheric Neutrinos*, Annual Review of Nuclear and Particle Science **51** (2001), 451–488.

[Kin07] G. S. King, *Neutrino mass*, Contemporary Physics **48** (2007), no. 4, 195–211.

[Kir10] I. V. Kirpichnikov, *Klapdor's claim for the observation of the neutrinoless double beta-decay of Ge-76. Analysis and corrections*, [arXiv:1006.2025v1] (2010).

[KK01a] H. V. Klapdor-Kleingrothaus et al., *Latest results from the Heidelberg-Moscow double beta decay experiment*, The European Physical Journal A - Hadrons and Nuclei **12** (2001), 147–154, 10.1007/s100500170022.

[KK01b] H. V. Klapdor-Kleingrothaus et al., *Evidence for Neutrinoless Double Beta Decay*, Mod. Phys. Lett. **A16** (2001), 2409–2420.

[KK06] H. V. Klapdor-Kleingrothaus and I. V. Krivosheina, *The evidence for the observation of $0\nu\beta\beta$ decay: The identification of $0\nu\beta\beta$ events from the full spectra*, Mod. Phys. Lett. **A21** (2006), 1547–1566.

[Kno00] G. F. Knoll, *Radiation Detection and Measurement*, 3 ed., John Wiley & Sons, 1 2000.

[Kra05] C. Kraus et al., *Final results from phase II of the Mainz neutrino mass searchin tritium β decay*, European Physical Journal C **C40** (2005), 447–468.

[Lee56] T. D. Lee and C. N. Yang, *Question of Parity Conservation in Weak Interactions*, Phys. Rev. **104** (1956), no. 1, 254–258.

[Leo92] W. R. Leo, *Techniques for Nuclear and Particle Physics Experiments*, 2nd ed., Springer, 1992.

[Mik86] S. Mikheyev and A. Smirnov, *Resonant amplification of ν oscillations in matter and solar-neutrino spectroscopy*, Il Nuovo Cimento C **9** (1986), 17–26, 10.1007/BF02508049.

[Ott10] E. Otten, *Searching the absolute neutrino mass in tritium β-decay—interplay between nuclear, atomic and molecular physics*, Hyperfine Interactions **196** (2010), 3–23, 10.1007/s10751-009-0150-2.

[Pau85] W. Pauli, *Wissenschaftlicher Briefwechsel mit Bohr, Einstein, Heisenberg u.a. / Scientific Correspondence with Bohr, Einstein, Heisenberg a.o.: Band/Volume 2: 1930-1939 (German and English Edition)*, 1 ed., Springer, 1 1985.

[Pov94] B. Povh et al., *Teilchen und Kerne (German Edition)*, 2nd ed., Springer-Verlag, 9 1994.

[Raf97] G. G. Raffelt, *Neutrino Masses in Astrophysics and Cosmology*, [arXiv:hep-ph/9704315] (1997).

[Rei56] F. Reines and C. L. Cowan, *The neutrino*, Nature **178** (1956), 446–449.

[Sch05] S. Schönert et al., *The GERmanium Detector Array (GERDA) for the search of neutrinoless $\beta\beta$ decays of ^{76}Ge at LNGS*, Nuclear Physics B - Proceedings Supplements **145** (2005), 242 – 245, NOW 2004.

[Shi10] Yu. A. Shitov and the SuperNEMO Collaboration, *A Search for Neutrinoless Double Beta Decay: from NEMO-3 to SuperNEMO*.

[Sis10] M. Sisti and the CUORE collaboration, *From Cuoricino to CUORE: Investigating neutrino properties with double beta decay*, Journal of Physics: Conference Series **203** (2010), no. 1, 012069.

[Ste09] M. Steidl, *Experiments for the absolute neutrino mass measurement*, [arXiv:0906.0454v1] (2009).

[Str95] B. G. Streetman, *Solid State Electronic Devices*, 2nd revised ed. ed., Prentice-Hall, 1995.

[Str10] A. Strumia and F. Vissani, *Neutrino masses and mixings and...*, [arXiv:hep-ph/0606054v3] (2010).

[Vet07] K. Vetter, *Recent developments in the fabrication and operation of germanium detectors*, Annual Review of Nuclear and Particle Science **57** (2007), 363–404.

[Wol78] L. Wolfenstein, *Neutrino oscillations in matter*, Phys. Rev. **D17** (1978), 2369–2374.

[Wu57] C. S. Wu et al., *Experimental Test of Parity Conservation in Beta Decay*, Phys. Rev. **105** (1957), no. 4, 1413–1415.

[Zub10] K. Zuber, *The status of the COBRA double-beta-decay experiment*, Progress in Particle and Nuclear Physics **64** (2010), no. 2, 267 – 269, Neutrinos in Cosmology, in Astro, Particle and Nuclear Physics, International Workshop on Nuclear Physics, 31st course.

Acknowledgements

I would like to take this opportunity to extend my warmest thanks to everyone who helped and supported me during my work on this thesis.

First of all, I would like to thank Prof. Allen Caldwell for supervising this work and offering me the chance to write my thesis in his group.

I would especially like to thank Dr. Béla Majorovits for his excellent support and encouragement throughout my entire time at the MPI.

I would like to thank the fantastic members of the GERDA- and GeDet-group in Munich for the great atmosphere at work and the fun we had afterwards - at the beer garden, the Christmas market, the squash court and at many other occasions. My sincerest thanks to Dr. Iris Abt for all our inspiring and instructive conversations on physics and beyond. Particular thanks and gratitude go to Sabine Hemmer for her endless support and motivation, to Xiang Liu and Daniel Lenz, who were always ready to help me, and to Daniel Greenwald, who was ever happy to provide me with linguistic guidance and strange music to listen to.

I would also like to express my gratitude to Jens Schubert for all I learned from him about C++ and Linux, to Oleksandr Volynets for our nice lunchtime conversations and his help with Geant4, to Franz Stelzer for his never-ending patience with the questions I asked him, and to Sabine Dinter for her precious help with every weird LaTeX problem I could come up with.

Last but definitely not least, I would like to thank my family who unremittingly supported and encouraged me throughout my entire life.

Erklärung

Mit der Abgabe der Diplomarbeit versichere ich, dass ich die Arbeit selbständig verfasst und keine anderen als die angegebenen Quellen und Hilfsmittel benutzt habe.

München, den 22. Oktober 2010

.....

Annika Vauth